Development of Encoding and Entanglement for Free Space Quantum Key Distribution

by

Yaseera Ismail

A thesis submitted in fulfilment of the academic
requirements for the degree of
Doctor of Philosophy
in the School of Chemistry and Physics,
College of Science, Engineering and Agriculture,
University of KwaZulu-Natal
Durban

Supervisor: Prof. Francesco Petruccione

November 2014

ABSTRACT

It is established that the manipulation of quantum information is bound only by the laws of physics and thus information can be characterised, quantified and processed as a physical entity using the basic properties of quantum mechanics. The most advanced quantum information related technology at present is Quantum Key Distribution (QKD). QKD encodes information into a quantum data carrier, in particular, a single photon that is transported through a quantum channel to produce secure key. To date QKD has been demonstrated across two types of channels which is generally fibre or free space. Free space QKD is beneficial since it provides various mediums for the encoding. When considering the atmosphere as a medium for free space QKD, one of the challenges is the effects of turbulence. Apart from the turbulence effects, one of the other challenges faced with implementing a QKD system, is the use of an appropriate source of single photons for the encoding. A good implementation of a source of single photons would be to make use of entanglement. This thesis addresses the above two aspects of QKD

Entanglement is essentially at the core of quantum mechanics and deals with the ability to couple two or more particles in time and space. It is relevant to all sub-atomic particles which include photons, electrons and ions. One of the techniques to obtaining an entangled photon pair lies in the successful implementation of a second-order nonlinear process which is referred to as Spontaneous Parametric Down Conversion (SPDC). The objective of this study was to build a polarisation encoded entangled single photon source using high powered lasers. The reason for this is that, for the successful implementation of free space QKD using entangled single photons, a bright source with high quality entanglement is required. We reach a power output of 400 mW and a violation of the Clauser, Horne, Shimony and Holt (CHSH) inequality, 0.8 % less than the theoretical limit.

Free space QKD is challenged by the effects of atmospheric turbulence due to additional noise introduced to the system. Hence it is of relevance hence to study the effects that turbulence poses on photons. Within this study we simulate atmospheric turbulence which was applied to two well known methods of encoding namely, polarisation and states carrying Orbital Angular Momentum (OAM). Polarisation encoding, when subjected to simulated turbulence, suffered phase dependence on the coincidence. This was due to the inefficient coupling of single mode fibre within the detection scheme. These results suggest that the design of an entangled source is crucial when utilised within non-ideal conditions. An alternative method of encoding is to make use of photons carrying OAM. Here we investigated an alternative approach to encoding of OAM states in the form of higher

order Bessel beams. Although OAM suffers much loss due to the break down of the phase in the presence of atmospheric turbulence, it is promising method of encoding to reach hyper entanglement states. Furthermore this will provide a means to attain dense coding.

Encoding and an appropriate single photon source is significant for the implemantation of free space QKD. The aforementioned investgations carried out within this thesis is promising for the further development of free space QKD.

PREFACE

The experimental work described in this thesis was carried out at the University of KwaZulu-Natal, School of Chemistry and Physics, Westville, Durban, from June 2012 to December 2014, under the supervision of Professor Francesco Petruccione and co-supervision of Professor Andrew Forbes. These studies represent original work by the author and have not otherwise been submitted in any form for any degree or diploma to any tertiary institution. Where use has been made of the work of others it is duly acknowledged in the text.

Signed:_____Yaseera Ismail

On this_____day of_____2014

As the candidate's supervisor I have approved this dissertation for submission.

Signed:_____ Prof Francesco Petruccione

On this_____day of_____2014

DECLARATION 1 - PLAGIARISM

I, Yaseera Ismail, declare that

1. The research reported in this thesis, except where otherwise indicated, is my original research.
2. This thesis has not been submitted for any degree or examination at any other university.
3. This thesis does not contain other persons' data, pictures, graphs or other information, unless specifically acknowledged as being sourced from other persons.
4. This thesis does not contain other persons writing, unless specifically acknowledged as being sourced from other researchers. Where other written sources have been quoted, then:(a) Their words have been re-written but the general information attributed to them has been referenced (b) Where their exact words have been used, then their writing has been placed in italics and inside quotation marks, and referenced.
5. This thesis does not contain text, graphics or tables copied and pasted from the Internet, unless specifically acknowledged, and the source being detailed in the thesis and in the References sections.

Signed:.....

DECLARATION 2 - DETAILS OF CONTRIBUTION TO PUBLICATION

Publication 1 - Published

Yaseera Ismail, Abdul Rahim Mirza and Francesco Petruccione. Characterisation of single photon entanglement source. The African Journal of Physics 9:0029, pp. 217-226 (2014).

Yaseera Ismail was the principal researcher, conducted the findings and authored the paper. Abdul Rahim Mirza, Andrew Forbes and Francesco Petruccione supervised the research and editted the publication.

Publication 2 - Published

Yaseera Ismail, Abdul Rahim Mirza, Andrew Forbes and Francesco Petruccione. Advancemnt of quantum communication through entanglement. Proceeding of the SAIP 2013, the 58th Annual Conference of the South African Institute of Physics, editted by Roelf Botha and Thulani Jili (2014), pp. 464-465. ISBN 978-0-620-62819-8. Available online at http://events.saip.org.za

Yaseera Ismail was the principal researcher, conducted the experimental work and authored the paper. Abdul Rahim Mirza, Andrew Forbes and Francesco Petruccione supervised the research and editted the publication.

Publication 3- Published

Abderrahmen Trichili, Thandeka Mhlanga, Yaseera Ismail, Filippus Roux, Melanie McLaren, Mourad Zghal, Andrew Forbes. Detection of Bessel beams with digital axicons. Optics Express Vol. 22, Issue 14, pp. 17553-17560 (2014).

Yaseera Ismail was a co-researcher and editted the publication.

Publication 4- Published

Abderrahmen Trichili, Thandeka Mhlanga, Yaseera Ismail, Filippus Roux, Melanie McLaren, Mourad Zghal, Andrew Forbes. Detecting Bessel Beams. Proc. SPIE 9194, Laser Beam Shaping XV, 91940B (September 2014) doi:10.1117/12.2061372

Yaseera Ismail was a co-researcher and editted the publication.

Publication 5- In Preparation

Yaseera Ismail, Abdul Rahim Mirza, Andrew Forbes and Francesco Petruccione. Instrumentation limitation on a polarisation based entangled single photon source. Journal of Optics.

Yaseera Ismail was the principal researcher, conducted the experimental work and authored the paper. Abdul Rahim Mirza, Andrew Forbes and Francesco Petruccione supervised the research and editted the publication.

Publication 6- In Preparation

Marco Mariola, Yaseera Ismail, Abdul Rahim Mirza and Francesco Petruccione. GPS Tracking. Physics Review.

Marco Mariola was the principal researcher, conducted the fieldwork and authored the paper. Yaseera Ismail was a co-researcher and co-author. Abdul Rahim Mirza and Francesco Petruccione supervised the research and editted the publication.

Presentations

The following is a list of conference/workshop presentations given during the period of my research:

Orals

1. Detection of Bessel Gauss modes by the use of holography. 57th South African Institute of Physics (SAIP) Conference, 9-13 July 2012, Pretoria, South Africa.
2. Recent findings in QKD at UKZN. Quantum Africa II, 3-7 September 2012, Mont aux Sources Hotel, South Africa .
3. Quantum Key Distribution (QKD) through entanglement. College of Agriculture, Engineering and Science Research day, 29 October 2012, PMB, South Africa.
4. Advancement of quantum communication through entanglement. 58th South African Institute of Physics (SAIP) Conference, 9-13 July 2013, Zululand, South Africa.
5. Free space quantum key distribution through entanglement.. Quantum Information Processing and Computing and control Conference 2, 25-29 November 2013, Pumula Beach Resort, South Africa.

6. Free space quantum key distribution through multiple entanglement sources. College of Agriculture, Engineering and Science Research day 2013, 1 November 2013, Howard college, South Africa.

7. The effects a simulated turbulent medium imposes on the quantumness of a polarisation based entangled photon source. IONS Montreal, 25-27 May 2014 , Ecole Polytechnique, Montreal, Canada.

8. The effects a simulated turbulent medium imposes on the non-classical properties of a polarisation encoded entangled photon source. Quantum Information Processing and Computing and control Conference 3, 3-7 November 2014, Drakensberg, South Africa.

Posters presented

1. Generation and analysis of polarisation entangled photons for Quantum Key Distribution (QKD). IONS Africa, 31 August- 2 September 2012, Cathedral Peak Hotel, Drakensberg, South Africa.

2. Characterisation of an polarisation based-entangled source. Quantum Information Processing and Computing Conference, June 30-5 July 2013, Florence, Italy.

3. Quantum communication in free space. South African Society for Atmospheric Sciences 2013, 26-27 September 2013, Salt Rocks Hotel, South Africa .

4. A study of the influences a diffractive plate has on the non-classical behaviour of a polarisation based entangled photon source. Quantum Cryptography 2014. 1-5 September 2014, Telecom Paris, Paris.

Other Conferences Attended

1. Quantum Diamond Conference, 2-8 December 2012, Bonamanzi, Zululand, South Africa.

2. 9th International Workshop on Adaptive Optics for Medicine and Industry, 2-6 September 2013, Stellenbosch, South Africa.

Schools Attended

1. 5th winter school on Practical Quantum Cryptography, 21-24 January 2013, LesDiablerets, Switzerland.

Awards obtained for this work

1. 1st prize for best oral presentation within the M-Stream Category at the UKZN College of Agriculture, Engineering and Science Research day, 29 October 2012, PMB, South Africa (Talk: "Quantum Key Distribution (QKD) through entanglement.")

2. 2nd prize for best PHD oral presentation within the Applied Physics forum at 58th South African Institute of Physics (SAIP) Conference, 8-12 July 2013, Zululand, South Africa (Talk: "Advancement of quantum communication through entanglement.")

3. 1st prize for best oral presentation within the M-Stream Category at the UKZN College of Agriculture, Engineering and Science Research day, 1 November 2013, Howard College, South Africa (Talk: "Free space Quantum Key Distribution (QKD) through multiple entanglement source.")

4. 3rd prize for best oral presentation at the 8th North American Optical Society of America Networking of Students Conference Conference, 25-27 May 2014, Montreal, Canada (Talk: "The Effects a Simulated Turbulent Medium Imposes on the Quantumness of a Polarisation-based Entangled Photon Source.")

Name: .....

Signed: .....

ACKNOWLEDGEMENT

This work is based upon the research supported by the South African Research Chair Initiative of the Department of Science and Technology and the National Research Foundation as well as the Council for Scientific and Industrial Research, National Laser Centre.

Achieving success is only possible if you are driven by the right individuals and a student is only as good as his/her supervisors. For this I would like to thank my supervisors, Prof. Francesco Petruccione and Prof. Andrew Forbes.

My deepest gratitude goes out to Prof. Francesco Petruccione for allowing me the opportunity to join the Quantum Research Group and the immense support during my research. Being a part of the Group has allowed me numerous opportunites to grow as a researcher and as an indivudual. I found a group where I fit in and for this I am eternally grateful. To Prof. Andrew Forbes, for moulding me as researcher and giving me the skills to conduct my research in an appropriate manner, thank you.

To the QKD Group, Dr. Abdul Rahim Mirza, Sharmini Pillay, Marco Mariola, Makhamisa Senekane and Dr. Mhlambululi Mafu, thank you for all great moments, work or otherwise. Each one of you have contributed positively to my PHD. Thank you for the brain storming sessions, long discussions, good advice and most importantly for the stress relief. A profound thank you goes out to Dr. Abdul Rahim Mirza for being an exceptionally great QKD group manager, for always proof reading my work, encouraging my ideas and constantly assisting with supportive guidance throughout my PhD.

To my office partners, coffee buddies, and good friends, Marco Mariola and Iulia Semina, thank you for always being around, the extra long conversations, the constant encouragement and for making the days gone by ever so special.

A special thank you goes out to Diane Sivil, who has assisted me throughout my PhD, in acquiring equipment and sorting out logistics for conferences. It has not always been an easy task however I thank you for all that you have done to support me through my research. I would like to extend a thank you to each individual in the Physics Department especially the members belonging to the Quantum Research Group for all the critical remarks and thoughts throughout my PhD.

An extra special thank you goes out to my parents, Ebrahim and Razia Ismail, my sibling Fernaaz Ismail and nephew Muhammed Areef Iqbal, the most important people in my life, for motivating me every step of the way. Without the constant encouragement and support I would not have reached this point. I am eternally grateful to you for constantly believing in me.

Contents

List of Figures

List of Tables

Nomenclature

BBO Beta Barium Borate

BG Bessel Gaussian

BLB Bessel Like Beam

CCD Charged Coupled Device

CHSH Clauser, Horne, Shimony and Holt

EPR Einstein, Podolsky and Rosen

HWP Half Wave Plate

ICT Information and Communication Technology

LC Liquid Crystal

LG Laguerre Gaussian

MDI Measurement Device Independent

OAM Orbital Angular Momentum

QIPC Quantum Information Processing and Commuication

QKD Quantum Key Distribution

QWP Quarter Wave Plate

SLM Spatial Light Modulator

SPAD Single Photon Avalanche Detectors

SPDC Spontaneous Parametric Down Conversion

SR Strehl Ratio

1 Introduction

1.1 Quantum Entanglement: A Breakthrough in Physics

"Everything we call real is made of things that cannot be regarded as real. If quantum mechanics hasn't profoundly shocked you, you haven't understood it yet. " - Niels Bohr

The understanding of realism and the physical world has been a matter of dispute amongst the most renowned scientist. The most essential understanding of the physical world can be categorised by two realms, namely the macroscopic and the microscopic. Within the macroscopic world the evolution of any system is governed by the laws of classical mechanics. This means, that the evolution of the system is deterministic and therefore influenced by casuality [1]. This differs when considering the microscopic world where a probabilistic approach is taken to fully understand the evolution of a system whereby the interactions within the system is governed by the laws of quantum mechanics [2, 3].

Quantum mechanics originated in the early 1900's with the work by Max Planck who discovered that energy is quantised indicating that it is always a multiple of a basic quantum denoted by $\hbar v$, where $\hbar$ is dependent on the fundamental constant, h, known as the Planck's constant and v is a characteristic frequency of the system being considered [4]. This discovery lead to decades of significant contributions confirming that quantization is indeed a legitimate theory, which governs the microscopic world of atoms, molecules, electrons and neutrons, and that nature essentially functions in this manner described by quantum mechanics. These significant contributions include Bohr's description of the quantum nature of an atom [5], De Broglie's formulation of the wave-particle duality [6], Heisenberg's Uncertainty principle [7] and Schrödinger's Superposition principle [8]. Quantum mechanics accounts for the above four occurrences which classical mechanics is unable to explain. The superposition principle, which includes entanglement, is the most bizarre of the aforementioned.

Entanglement occurs when two or more particles interact physically but indistinguishably and thereafter separate, such that knowledge about a distant particle can be obtained by observing its local entangled partner. Particles which are entangled are said to be in a state of superposition until an observation or measurement is carried out as explained by Schrödinger's with his famous "cat in a box" analogy [8]. According to this thought experiment, a cat is placed in a box with a radioactive alpha particle. It is unbeknown to the observer as to when the radioactive alpha particle will decay which will trigger a poison and the cat will die. It is intepreted that the cat is alive and dead at the same time. It is only when the box is opened can it be confirmed as to the state of the cat (dead or alive) [8]. Similarly, the properties of quantum particles in particular entangled particles remains in an indefinite state until a measurement is carried out and an outcome is obtained. Entanglement is not constrained to a finite distance. This basically means that the properties of entanglement holds irrespective of the distance between entangled particles.

Concurrent to the investigations by Schrödinger, the subject of entanglement, was contested by Einstein, Podolsky and Rosen (EPR) who argued that entangled systems contradict the classical notions of both reality and locality [9]. Local realism is an amalgamation of the principle of locality which states that an object may only be influenced directly by its immediate surroundings and realism which infers that an object must have a preceding value before a measurement is undertaken. EPR proposed that the existence of quantum entanglement renders quantum mechanics incomplete since it does not satisfy the completeness condition *[9]* which states that

"Every element of the physical reality must have a counterpart in the physical theory[9]."

For a better understanding of this notion, EPR, considered two physical systems which were to interact with respect to a certain observable. Due to this interaction, the two systems would display a strong mutual relation with respect to that observable. It was deduced that, the outcomes of the observables measured for each of the two systems cannot be predicted with certainty however the outcomes of the observables for any arbitrary measurement of the complete system is always strictly correlated. EPR based their finding on the well-known Gedanken experiment [9]. From this, it was generalised that quantum entanglement violates the physical reality in the sense that, unlike the classical notion, the individual results are essentially undetermined before the measurement is undertaken.

According to quantum mechanics, the measurement of a certain observable in one EPR system instantaneously determines the state of the other system, regardless of the distance between the systems. This condition implies that quantum entanglement also contradicts the concept of locality. EPR hence hypothesised that there should exist a local hidden

variable scheme which accounts for the outcomes of an entangled system [9].

The dilemma of the existence of a local hidden variable was addressed years after the EPR paper by physicist John S. Bell in his seminal paper entitled "On the Einstein, Podolsky and Rosen paradox." In this paper, Bell showed mathematically that EPR's ideas about causality and locality are incompatible with the predictions of quantum mechanics. According to Bell's paper both quantum mechanics and local hidden variables can not be correct, either local hidden variables or quantum mechanics is right. It was further stated that if quantum mechanics is the correct description of the microscopic world, then non-locality is a significant element of this world [10].

Bell validated entanglement and quantum mechanics based on the Bohm interpretation [11]. He assumed that hidden variables could exist [10] and considered a case in which two entangled spin-$\frac{1}{2}$ particles in the singlet state are emitted from a common source, and analysed what transpired in such an experiment. The assumption is, that the existence of hidden variables are the carriers of the missing information. Hence the particles are programmed with a set of instructions that informs them, in advance how to react for each measurement outcome. By means of this assumption, Bell obtained a contradiction, which proved that quantum mechanics could not be supplemented with any hidden-variables scheme hence Bell's theorem states that hidden variables and a locality assumption have no place within the quantum theory. This theorem is expressed in terms of the Bell's inequality which if violated signifies evidence of non-locality. Furthermore this theorem inspired experiments that established that entanglement is a real phenomenon.

The expansion of Bell's seminal work was established years later by Clauser, Horne, Shimony and Holt (CHSH). CHSH proposed an experiment to test Bell's theorem [12] in which they demonstarted that by measuring the polarisation states of photons, it is possible to calculate the quantum mechanical predictions for the correlations of these polarisations states. They hence showed that the calculated correlations violated Bell's inequality. This formed a definitive test for the verification entanglement known as the violation of the CHSH inequality [12].

Ultimately, the theoretical prediction made by Bell and the proposed experiment by CHSH provided an end to the dispute of entanglement and the verification of quantum mechanics and opened a window for the progression of entanglement based experiments. The simplest scheme for demonstrating entanglement is observed in a bi-partite system in which electron spins are entangled. The first experimental source of polarisation-entangled photon pairs were implemented with atomic-cascade decays [13, 14, 15]. Aspect and colleagues used this process of atomic cascades to produce entangled photons at a rate of 3.8 photons per second per mW [16].

Since the demonstration of entanglement by Aspect *et al*, quantum correlations were also observed between photon pairs emitted from non-linear crystals, pumped with strong coherent light [17, 18].

Over the last two decades the design of Spontaneous Parametric Down Conversion (SPDC) sources has become more distinguished resulting in less complex setups. Originally SPDC based sources required polarisation independent 50:50 beam splitters in order to convert correlated photon pairs into entangled states [17, 18, 19, 20, 21]. The requisite for such beam splitters was removed with a new source designed by Kwiat *et al* in 1995 [22] and 1999 [23]. These designs, demonstrated in 1995, utilised the concept of non-collinear type-II phase matching, where photon pairs were emitted from a single downconversion crystal in an entangled polarisation state.

SPDC can also be achieved through a technique known as Quasi-Phase Matching (QPM). QPM was first described by Armstrong *et al.* [24] as well as by Franken and Ward [25]. In QPM, frequency conversion is enhanced through some kind of periodicity in the non-linear material. This periodicity can be introduced by alternating the orientation of the crystal optical axis between two directions. These crystals are known as periodically poled crystals. The primary application of QPM is in second harmonic generation [26] however, periodically poled materials are being increasingly used for SPDC as well. The first sources exploiting QMP to obtain entangled photon pairs were implemented in 2001 [27, 28] .

Bulk periodically poled crystals have since become available, leading to a simpler alignment criteria and also higher quality of entangled photon pairs [29, 30, 31, 32]. Such sources display better spectral brightness compared to sources based on angle phase matching. It was only in 2007, that a periodically poled crystal source had been able to achieve a competitive quality of entanglement when fabricated by Fedrizzi *et al.* [33].

Four-Wave Mixing (FWM) has also been demonstrated to produce entangled photon pairs [34]. Although FWM experiments had been carried out before to demonstrate quantum correlations, recent experiments are geared towards producing telecom wavelength photon pairs taking place inside a micro-structure fibre. In a recent experiment, Fan *et al.* [35] reported a measured pair generation rate of 7000 pairs per second using only 300μW of pump power in a 1.8m patch of fibre that was at room temperature. FWM appears to be a promising method for correlated photon pair generation. A complete review of single photon sources is provided by Fan *et al* [36].

1.2 Entanglement: A Resource in Quantum Information, Processing and Communication

Entanglement sources have become a useful resource for various disciplines of science specifically in the field of Quantum Information, Processing and Communication (QIPC). QIPC is a field concerned with technological implementations established on quantum mechanical phenonomena. It is based on the notion that the manipulation of information is governed by the quantum effects of physics. Hence, quantum information can be characterised, quantified and processed as a physical entity using the basic properties of quantum mechanics. This is achieved by exploiting some of the fundamental features of the quantum world, namely, the Superposition principle and the Heisenberg Uncertainty relation. QIPC encapsulates two major disciplines, quantum computing and quantum communication, both provide an enabling technology towards future ICT solutions.

Quantum computing involves performing operations based on quantum mechanical phenomena. This is implemented by encoding information in either a bit 0 or 1 or in a superposition of bits of 0's and 1's known as qubits which is possible due to the process of entanglement. Quantum computing makes use of the properties of quantum systems to achieve exponential speed-up of certain computational tasks. Quantum computational algorithms have the possibility to implement fast searches, and factor prime numbers in polynomial time scales. Quantum computing is an extremely challenging and an inherently difficult task to experimentally implement. Thus far, fairly simple quantum computational tasks have been performed [37, 38, 39]. This is a revolutionary new paradigm that will allow us to build machines capable of solving problems that cannot be solved today. Currently, the progress of quantum computers suffers from the ability of invoking entanglement on demand. Quantum computing is directly related to quantum communicaton, in the sense that, in theory the development of a fully functional quantum computer will render current encrpytion methods, which are based on mathematical complexities, obsolete.

Currrent conventional encryption techniques are based on the complexity of mathematical algorithm which relies on the factorisation of large numbers. The principle variation between conventional and quantum encryption is the key distribution process. Conventional key distribution encapsulates the key data within a mathematical construct that may not be efficiently reversed without sufficient information using current knowledge and computing power [40]. Quantum encryption or Quantum Key Distribution (QKD) encodes the key information into a quantum data carrier, in particular, a single photon that is then transported from one point to another via a quantum channel which is generally free space

or fibre. This shifts the security basis away from mathematical complexities and towards fundamental physical boundaries set by the laws of quantum mechanics. This therefore means that the retrieval of the key information by unauthorized parties requires one to defy the laws of quantum mechanics. QKD provides a future-proof technology for secure communications. It is therefore applicable to situations that require confidential information to remain secure for extended periods of time. Entanglement offers an extra layer of security to the key distribution process since the state of an entangled photon remains indefinite, that is, until an observation is performed. Furthermore, entanglement provides a means of increasing the length of the quantum channel resulting in the ability to achieve QKD at longer distances or alternatively building a quantum network [41].

1.3 Motivation for the Development of Entanglement Sources

Free space QKD systems can provide a means of secure communication between remote sites that have a line of sight between them. One of the major advantage of free space QKD is the possibility of a low cost solution to transfer information within terrestrial areas and the access to mobile links. This will also lead to satellite based communication as well as information transfer between un-trusted nodes in the form of Measurement Device Independent (MDI) QKD [42]. For the successful implementation of a QKD link the following criteria needs to be adhered to:

1. An appropriate encoding should be chosen dependent upon the quantum channel.

2. A single photon source which can survive the turbulence or noise of the quantum channel.

3. A means to coarse and fine align the transmitter and the reciever which becomes vital especially if the line of sight is of the order of hundreds of kilometers.

4. A synchronisation system for the transmitter and receiver.

5. Efficient detectors to limit the quantum bit error rate.

The development of free space QKD is also dependent upon the advancement of other quantum based technologies, namely, quantum repeaters and quantum memory. Quantum repeaters is an enabling device for extending an optical communication link. In the same manner as amplifiers are used for classical communication, it is possible to increase the quantum channel in which entanglement, and hence quantum information, is distributed by chaining several quantum repeaters. One implementation of a quantum repeater is based on light-matter interactions at the quantum level in a specific crystal that

stores quantum information by coherent control of the quantum degrees of freedom [43]. Quantum repeaters requires the use of quantum memories which is the storage of quantum states [44]. The combination of entangled photons and quantum memories is at the heart of the development of quantum repeaters. Furthermore, the realisation of quantum repeaters will enable the development of building a quantum network. The development of free space QKD is also favorable since it is not restricted to ground to ground communication and will eventually lead to the progression of ground to satellite communication. Secure transmission of QKD has been performed over 144 km of free space [45]. To an extent the distance of free space QKD is limited by the quality of entanglement which is partly dependent on the brightness of the source [23].

This thesis will address the first two of the aforementioned points listed for the successful implementation of a QKD link focusing on the use of entangled single photons as a source for the encoding. The last three points mentioned falls beyond the scope of this thesis.

1.4 Research Contributions

This thesis is based on the research conducted at the Centre for Quantum Technology (CQT). The thesis subject is based on various publications and a conference proceeding authored and co-authored during the course of this study. The work carried out during this study has received various awards at national and international conferences. These papers, conferences and awards are outlined on pages iv-vii . The main results are collated together in the following subsections. Although this thesis is based explicitly on entanglement, throughout this study reference is made to free space quantum communication with the aim of placing the work investigated into context.

1.4.1 Verification of Entanglement

The focus of this study is based on understanding the progression of the field of entanglement, specifically concentrating on the development of entanglement sources and its usefulness within the field of QIPC. This involves considering the role entanglement plays in a QKD scheme. Preliminary studies of this study deals with an overview of the theoretical aspects of entanglement and methods of obtaining entanglement. Specifically concentrating on SPDC which is a non-linear process of generating entangled single photons. Emphasis is placed on reviewing a detailed study of the theory of entanglement and the testing the quantum correlations of an entangled system. This involves experimentally demontrating the verification of entanglement of a polarisation encoded single photon source by means of the violation of the CHSH inequality as well as determining

the quality of entanglement both in the rectilinear and the diagonal basis. The presevation of the generated states are also verified by carrying out a state tomography of the system and reconstructing the density matrix from which the fidelity of the system is determined. This work has been accepted for publication in the African Review of Physics Journal and is outlined in Chapters 2 and 3.

1.4.2 Influences of Turbulence on a Single Photon Source

The behaviour of entangled single photon sources under non-ideal conditions is of relevance when considering a free space optical communication link. One of the major setbacks of free space QKD is dealing with turbulence effects in the atmosphere. These effects are much more severe in a phase encoding system as opposed to a polarisation encoding system however both these systems are worth studying. For the purpose of this study atmospheric turbulence is simulated using a diffractive plate encoded with turbulence based on Kolmogorov theory [46, 47]. The strength of the simulated turbulence is quantified classically by considering the deformation of the intensity profile of a Gaussian beam at various positions on the plate.

Incorporating the aforementioned turbulent plate into a polarisation encoding entangled single photon source provides a means of investigating the limitation that turbulence imposes on the source during the implementation of a QKD link. This is achieved by carrying out a complete analysis of the behaviour of the source. Of importance, is the realisation that the standard detection method of single mode fibre coupling to single photon counters results in a spatial mode dependence on the coincidences, even if the entanglement is not measured with spatial modes. This work is being prepared for submission for publication in the Journal of Optics and is outlined in Chapter 4.

An alternative approach to encode an entangled single photon source is through the use of states carrying Orbital Angular Momentum (OAM). This shifts the attention away from a polarisation encoded entanglement source to a method of generating entangled photons that spans an infinite state space. Emphasis is placed on the generation of these modes carrying OAM in the form of Laguerre-Gaussian (LG) and Bessel-Gaussian (BG) beams. The adavantage OAM poses to an entanglement system and the propagation of these beams (Bessel-Gaussian) through turbulence is of interest. Furthermore this study involves demonstrating the changing radial and azimuthal spectrums of the these beams implemented for the first time. The aforementioned is outlined in Chapter 5. This work was published in Optics Express [48].

1.4.3 Bright Polarisation Encoded Single Photon Source

Free space QKD is limited by the survival of single photons through the atmosphere. As far as single photon sources are concerned, the brighter the source the greater the photon generation for SPDC. The brightness of the source is directly related to the power input. To reach a longer distance, a bright source is required. This forms part of the aim of this study, engineering a bright polarisation encoded single photon source. The quantum correlation of this new source is determined by carrying out a complete characterisation of the source in terms of measuring the quality of entanglement, determining the violation of the CHSH inequality and measuring the fidelity of the system. Of relevance, is the method of combining economical lasers to enhance the power of the source. This work is currently in the process of being prepared for publication and is outlined in Chapter 6.

2 Theory of Entanglement

2.1 A Description of Entanglement

Entanglement is a characteristic of quantum mechanics in which the correlations collectively between separate systems cannot be acquired from the states of the individual systems. It occurs when two or more sub-atomic particles such as photons or electrons interact and thereafter separate resulting in an instantaneous correlation shared between them. As an example, this correlation between quantum entangled particles can be further explained by considering a spin zero sub-atomic particle which decays into two spin half particles which are said to be maximally entangled as represented in Figure 2.1.

These two particles decay to two individuals, A and B, whereby one of the decayed particles is measured at position A and the other at position B. Since both the decayed particles are required to add-up to a spin zero state, if at position A the particle is measured to be in a spin up state then consequently at position B a spin down state will be measured. This instantaneous correlation is independent of the distance between A and B and this is where the phenomena of entanglement comes into role.

When considering the behaviour of a particle, in particular a photon, it is represented by a probabilistic wave function whereby the position of the photon is unknown however it can be represented as a probabilistic distribution denoted as [49]:

$$\big|\psi\big\rangle = \alpha_1\big|\psi_1\big\rangle + \alpha_2\big|\psi_2\big\rangle + ... + \alpha_n\big|\psi_n\big\rangle, \tag{2.1}$$

where $\alpha_1, \alpha_2, ..., \alpha_n$ are the complex coefficients defined by the condition $\alpha_1^2 + \alpha_2^2 + ... + \alpha_n^2 = 1$. The properties of the photon are defined in terms of the position and momentum as described by the Heisenberg's Uncertainty principle. These properties remain indefinite until an observation has been made which collapses the wave function. Photons

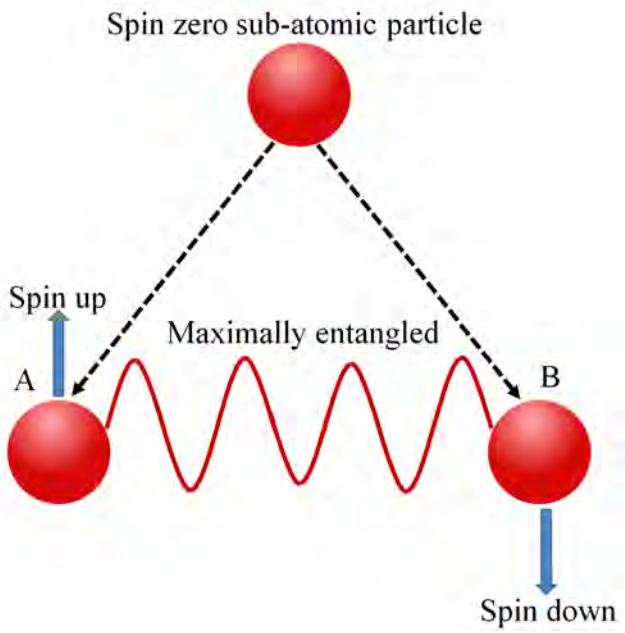

Figure 2.1: Illustration of the decomposition of a spin zero sub-atomic particle into two spin half particles, A and B, which are maximally entangled.

which are entangled are considered inseparable and are therefore represented as a single state. This means that for a complete description of any qubit within an entangled system, the description of its entangled partner is also included. This also implies that there exists a strong mutual correlation between maximally entangled photon pairs [50].

Photons can be entangled via time-bin, phase or polarisation. Time-bin entanglement is established by making use of a Franson interferometer which consists of two spatially separate unbalanced Mach-Zehnder interferometers through which the generated photon pairs created from SPDC are transmit individually [51]. Phase based entanglement is established by either encoding a photon to carry OAM by introducing an azimuthal phase variation [52] or by establishing a phase delay achieved using a Mach Zehnder interformeter [53]. For the remainder of this study the main focus will be on a polarisation based single photon source although other types of entanglement will be discussed in Section 2.2.2 and Chapter 5.

2.2 Methods of Entanglement

Various methods of obtaining entanglement do exist, such as the use of quantum dots [54], exploiting atomic cascades [55] or through the use of FWM in chip-scale micro-resonators [56, 57, 58]. One of the most well known methods of generating entangled

pairs occurs through a process known as SPDC achieved by pumping a non-linear crystal resulting in the downconversion of a parent photon into a pair of daughter photons of lower energy known as a signal and an idler [59].

2.2.1 Spontaneous Parametric Down Conversion

The spontaneous creation of photons through non-linear interactions was first investigated theoretically by David Klyshko [60] and experimentally by David Burham and Donald Weinberg [59]. Burnham and Weinberg showed that by pumping a 25 mm long ammonium dehydrates phosphate crystal with a He-Cd laser lasing at 325 nm, it is possible to downconvert a photon into a single photon pair (signal and idler) [59]. The essential feature of SPDC is that a single pump photon passing through a uniaxial non-linear optical material, undergoes excitation and decay back to the ground energy level resulting in the generation of two daughter photons obeying energy and momentum conservation. These daughter photons will be correlated in momentum, energy and time. The standard technique for detecting photon pairs is the timing coincidence method that was first demonstrated in 1970 by Burnham and Weinberg [59]. Due to the non-linear interaction of the pump photons, the daughter photons (signal and idler) will satisfy the following frequency and phase matching condition as represented by Equation (2.2) and (2.3) respectively

$$\omega_s + \omega_i = \omega_p, \tag{2.2}$$

$$\vec{k}_s + \vec{k}_i = \vec{k}_p, \tag{2.3}$$

where ω_s, ω_i and ω_p are the frequency of the signal, idler and pump respectively and $\vec{k}_s$, $\vec{k}_i$ and $\vec{k}_p$ denote the wave number of the signal, idler and pump respectively. From the above relationships it is clear that during this process of SPDC there is a conservation of momentum and energy. As shown the additive energy of the signal and idler is equal to the energy of the pump photon and similarly for the momentum which is further illustrated in Figure 2.2. Essentially, phase matching relates to maintaining an appropriate phase relationship between the interacting waves along the direction of propagation satisfying the condition represented in Equation (2.2) and (2.3). This process of SPDC can occur in non-linear crystals which satisfies type-0, type-I or type-II phase matching [61].

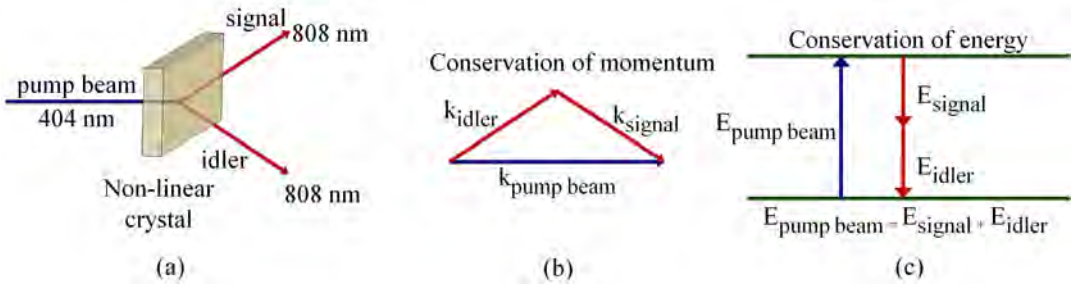

Figure 2.2: Down conversion occurs when a pump photon is downconverted into a signal and idler (a). During this process there is a conservation of momentum where k_{idler}, k_{signal} and $k_{pump\ beam}$denote the wave number of the idler, signal and pump beam respectively (b) and the conservation of energy where E_{idler}, E_{signal} and $E_{pump\ beam}$ denote the energy of the idler, signal and pump beam respectively (c) such that the energy of the signal and idler is equal to that of the pump photon and similarly for the momentum.

Type-I Downconversion

During SPDC the downconverted photons form emission rings which are wavelength dependent. This emission pattern is formed by cones, which are perpendicular to the direction of the pump beam. For type-I phase matching the cones are concentric around the pump direction as illustrated in Figure 2.3. Each cone corresponds to a distinct wavelength emitted. The opening angles of the emission cones depend on the wavelengths of the emitted photons and on the opening angle between the pump direction and the optical axis, θ_p.

The generation of polarisation based entanglement through SPDC using a type-I crystal, requires the use of two crystals mounted orthogonal to each other. For this type of configuration the optical axis of the first crystal is aligned in the vertical plane while the optical axis of the second crystal is aligned in the horizontal plane. Due to the type-I coupling, the downconversion process occurs only in the crystal where the pump photon is extraordinary polarised emitting two ordinary polarised downconversion photons into the characteristic cone.

Extraordinary polarised photons propagate parallel to the optical axis while ordinary polarised photons travel perpendicular to the optical axis. In terms of the vertically polarised pump the downconversion process occurs only in the first crystal emitting pairs of horizontally polarised photons where as with the horizontally polarised pump the downconversion process occurs only in the second crystal producing two vertically polarised photons.

By pumping the crystals with linearly polarised light at 45 degrees with respect to the orthogonal axes, there is an equal probability that a pump photon will be downconverted in either crystal as illustrated in Figure 2.4. It is only recently that concatenated type-I

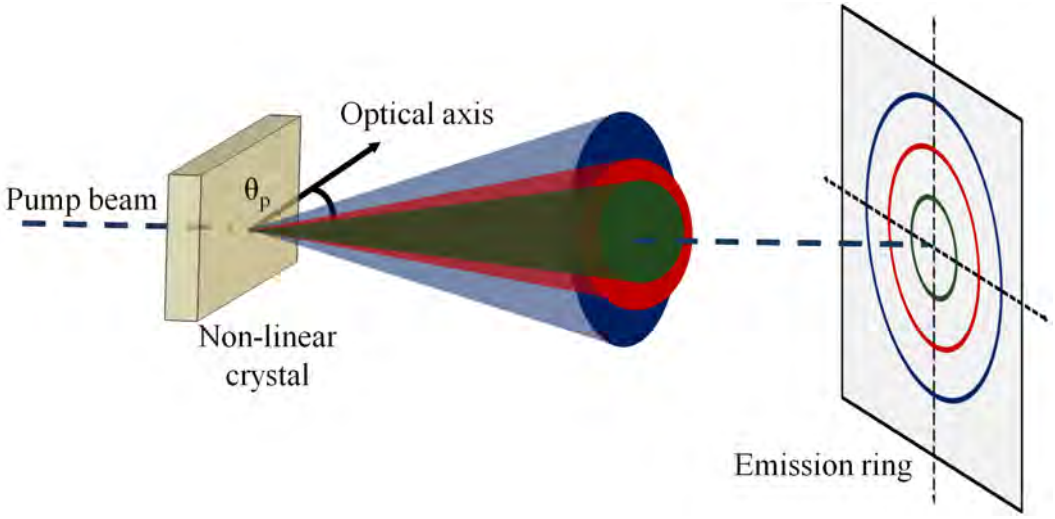

Figure 2.3: Spatial Distribution of the downconversion emission for type-I phase matching. Each cone corresponds to a distinct wavelength. Furthermore, each of the emission cones depends on the wavelengths of the emitted photons and on the opening angle between the pump direction and the optical axis, θ_p.

crystals have been used for entanglement [62]. Previously most entangled sources relied on type-II downconversion. It is worth noting that type-I downconversion produces a higher photon generation as well as the alignment of such a system is reasonably simpler.

Type-II Downconversion

Most downconversion sources rely on non-collinear type-II phase matching. During this process downconversion occurs at certain phase matching angles, θ_p , between the pump beam and the optical axis of the non-linear crystal. The phase-matching conditions are satisfied such that the photons are emitted within cones as illustrated in Figure 2.5. Here, the photon originating from one of the cones is ordinarily polarised while the other is extraordinarily polarised. During type-II downconversion the generated photon pairs are always polarised orthogonally. The photons that are emitted are indistinguishable in terms of which cone they originated from. This procedure results in the generation of a pure polarisation entangled state.

2.2.2 Other Types of Entanglement Through Spontaneous Parametric Down Conversion

Apart from polarisation based entanglement there exist other types of entanglement generated through SPDC which includes time bin [63], momentum based [64] and higher-

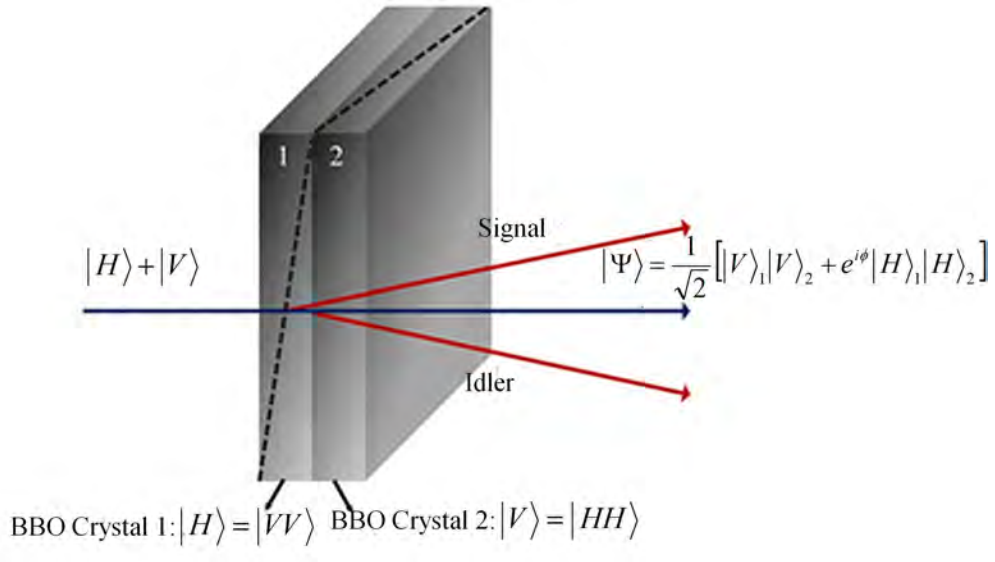

Figure 2.4: Polarisation based entangled photon pairs generated using two type-I crystal orientated orthogonal to each other. By pumping the crystal with linearly polarised light at 45 degrees with respect to the orthogonal axes containing a horizontal state, $|H\rangle$, and a vertical state, $|V\rangle$, there is an equal probability of a pump photon downconverted in either crystals. This means that the horizontal state, $|H\rangle$, can be downconverted into two vertical states $|VV\rangle$ or the vertical state, $|V\rangle$ can be downconverted in two $|HH\rangle$ states. This will result in the generation state, $|\psi\rangle$ where ϕ is the relative phase between the ordinary and extraordinary polarised light, $|V\rangle_1$ and $|H\rangle_1$is the vertical and horizontal state respectively generated by crystal 1 and $|V\rangle_2$ and $|H\rangle_2$is the vertical and horizontal state respectively generated by crystal 2.

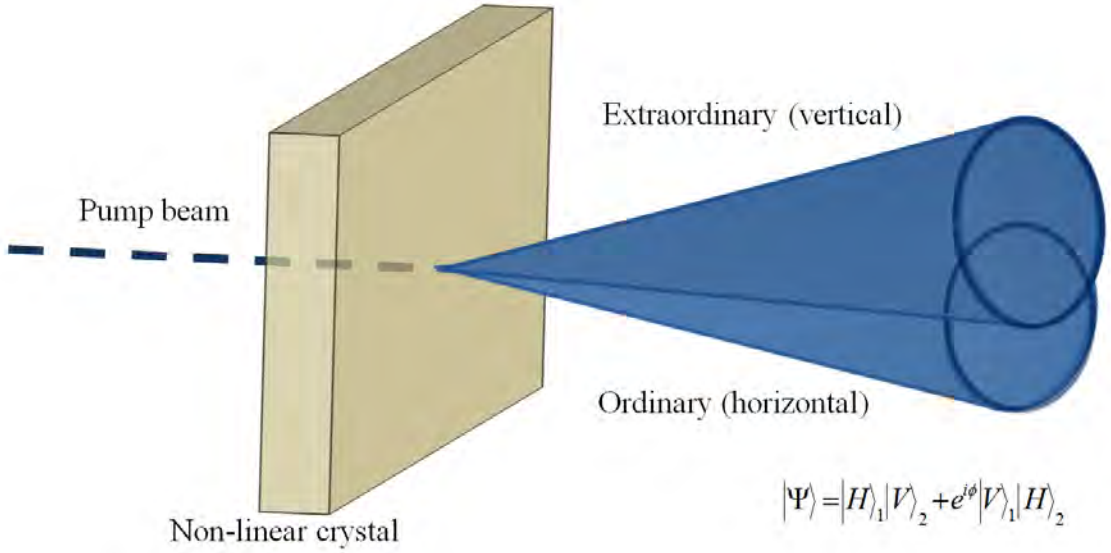

Figure 2.5: Spatial distribution of the downconversion emission for type-II phase matching whereby a pump photon emits ortogonally polarised states. The states that are generated is indistinguishable in terms of which cone they originated from which leads to the creation of a pure polarisation entangled state. The polarisation state, $|\psi\rangle$, emitted from the crystal consist of a horizontal state, $|H\rangle$, and a vertical state, $|V\rangle$, and ϕ is the relative phase between the ordinary and extraordinary polarised light

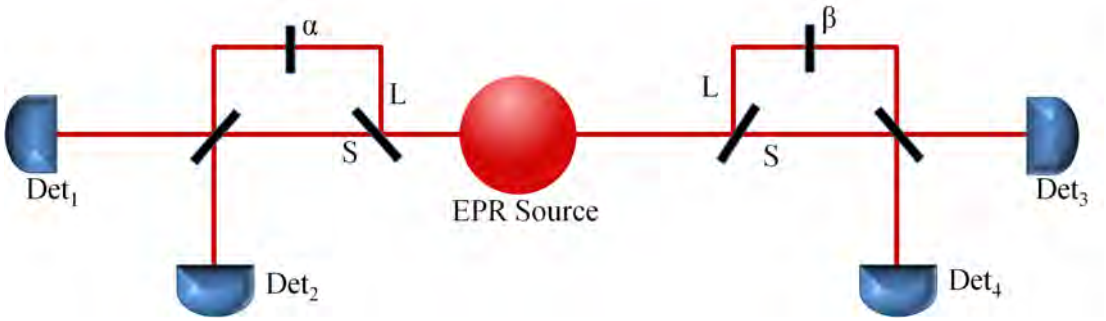

Figure 2.6: Schematic illustrating the generation of time bin entangled photon pairs using a franson interferometer consisting of an unbalanced Mach-Zehnnder interferometer. Due to the unbalanced path length, the entangled photons can either follow the long path, L, or the short path, S, creating an entangled state that is a superposition of $|L\rangle$ and $|S\rangle$. The photons are detected by detectors; Det_1, Det_2, Det_3 and $Det_4$and α and β are two fused phase plates.

dimensional entanglement using OAM states [65]. The aforementioned types of entanglement will be briefly explained below.

Time bin entanglement

Time bin entanglement may be generated using type-I or type-II downconversion crystals and depends solely on the fact that the two photons in a pair are created simultaneously and that they satisfy the laws of energy conservation. This means that the emission time of any pair is uncertain within the coherence time of the pump laser. This kind of entanglement has been used for so-called two-photon Franson-interferometry, where both photons pass separate unbalanced Mach-Zehnder interferometers as illustrated in Figure 2.6 [63] . The two interferometers are constructed in the same way such that the coherence length of an individual photon is shorter than the path length difference.

Consequently no interference can be seen in the direct count rates of the detectors at the outputs of the interferometers however the variation of phases between the arms of the interferometers results in oscillations of the coincidence counts. The generated state, $|\psi\rangle$, within the interferometers can be represented by

$$|\psi\rangle = \frac{1}{2}\left[|S\rangle_1|S\rangle_2 + e^{i(\phi_1+\phi_2)}|L\rangle_1|L\rangle_2 + e^{i\phi_2}|S\rangle_1|L\rangle_2 + e^{i\phi_2}|L\rangle_1|S\rangle_2\right], \tag{2.4}$$

where $|S\rangle$ is the state if the photon follows the short path and $|L\rangle$ is the state if the photon follows the long path, subscripts 1 and 2 refer to the photon moving to the left and to the right respectively (see Figure 2.6) and ϕ_1 and ϕ_2 are independent phase controllers. The state generated is in fact a product state however only long-long (L-L) and short-short (S-S) detections are truly coincident at the detectors and other events can be discarded

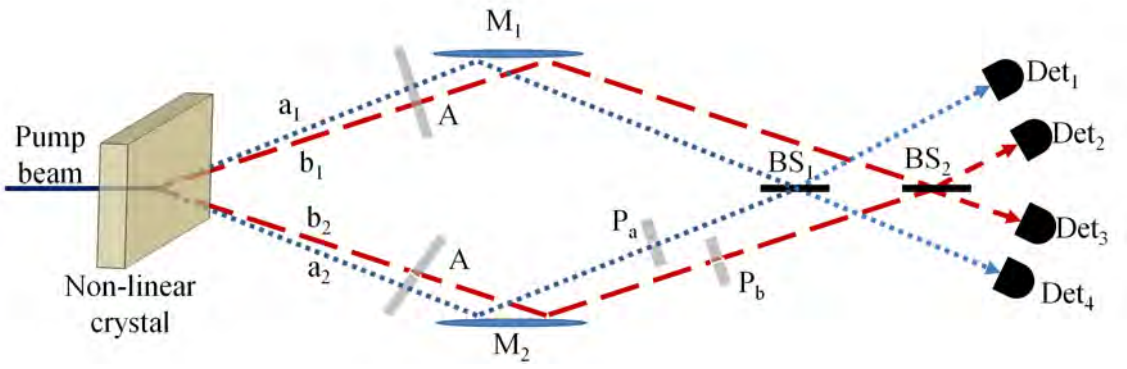

Figure 2.7: Schematic illustrating the generation of momentum based entanglement. During this process the individual mode pairs from the emission of a downconversion source are selected such that each pair consists of one photon with ν_a (slightly above half of the pump frequency) and one photon with ν_b (slightly below half of the pump frequency). The pairs are emitted into either modes a_2, b_1 or modes a_1, b_2 which are transmitted through an aperture, A, and thereafter reflected by mirrors (M_1 and M_2) onto two beamsplitters (BS_1 and BS_2) . The photons are detected by detectors Det_1 , Det_2 , Det_3 and Det_4 . In either arms of the interferometer there are two independent phase adjusters, P_a and P_b.

by suitable coincidence gating. Thus, if a pump photon undergoes excitation and emits a twin-photon inside the crystal after the first interferometer, the time of creation of the latter is undefined. More precisely, the unbalanced interferometer transforms the state of the pump photon in a superposition of $|\psi\rangle = \alpha|S\rangle_{\text{pump}} + \beta|L\rangle_{\text{pump}}$, where α and β represent the phase and the downconversion process in the crystal transforms this state into

$$|\psi\rangle = \alpha|L\rangle_1 \otimes |S\rangle_2 + \beta|L\rangle_1 \otimes |S\rangle_2. \tag{2.5}$$

Momentum Based Entanglement

Another kind of entanglement that is present in non-collinear downconversion is momentum based entanglement. This is induced by the phase matching relation which governs the emission of different wavelengths into different directions. During this process the individual mode pairs from the emission of a downconversion source are selected. The selection is such that each pair consists of one photon with ν_a (slightly above half of the pump frequency) and one photon with ν_b (slightly below half of the pump frequency). The pairs are emitted into either modes a_2, b_1 or modes a_1, b_2 as shown in Figure 2.7 [64].

Thus the state before the beam splitter ($BS_1$and BS_2 in Figure 2.7) is

$$\left|\psi\right\rangle = \frac{1}{\sqrt{2}}\left[e^{i\phi_b}\left|a\right\rangle_1\left|b\right\rangle_2 + e^{i\phi_a}\left|a\right\rangle_2\left|b\right\rangle_1\right], \tag{2.6}$$

which is entangled although the modes at this stage are clearly distinguishable where ϕ_a and ϕ_b are the phase of the a-modes and b-modes respectively. The entanglement manifests itself when the a-modes and b-modes are recombined in a beam splitter. Within this system the interference visibility is low compared to a polarisation based entanglement source which is due to the difficulties of alignment and the overlap of the four beams.

Higher-Dimensional Entanglement using Orbital Angular Momentum States

Entanglement based on OAM states was first demonstrated by Mair *et al* [65], in which it was shown that OAM is conserved during the process of SPDC. The OAM carried by the photon is related to the spatial distribution of the light wave. The first generation of laser beams carrying OAM was demonstrated by Allen *et al* [66]. These beams have a helical phase front and possess an azimuthal phase dependence of $\exp(i\ell\phi)$, where ℓ is the azimuthal phase index of integer value which represents the number of azimuthal phase rotations, ϕ, in one full cycle from 0 to 2π.

A photon pair that is entangled in the OAM basis can be represented by a state $\left|\psi\right\rangle$ as [65]

$$\left|\psi\right\rangle = \sum a_{\ell,-\ell}\left|\ell\right\rangle\left|-\ell\right\rangle, \tag{2.7}$$

where $\left|a_{\ell,-\ell}\right|^2$ is the probablity of finding one of the photons in either the positive azimuthal index state, $\left|\ell\right\rangle$, or the negative azimuthal index state, $\left|-\ell\right\rangle$, where the pump beam has a zero OAM. The interest behind generating OAM states can be attributed to the creation of states which theoretically span an infinite state space [67]. Furthermore these beams are beneficial when incorporated into a QKD system since OAM states exhibit a continuous nature of time and frequency or position and momentum which potentially results in an unlimited information capacity even on a single photon level whereas polarisation encoding is restricted to one bit per photon [68]. One of the drawbacks of incoporating OAM states within a free space QKD system would be the degradation of entanglement due to the break up of the phase as these beams propagate through the atmosphere [69]. This process of OAM state generation and the effects of atmospheric turbulence on the generated states will be addressed further in Chapter 5.

2.3 Verification of Polarisation Encoded Entanglement

A photon pair which is entangled via polarisation can be represented either by the rectilinear (horizontal and vertical) or the diagonal ($\pm$ 45 degrees) bases represented as:

$$\left|\psi\right\rangle = \frac{1}{\sqrt{2}}\left[\left|V\right\rangle_s\left|V\right\rangle_i + e^{i\phi}\left|H\right\rangle_s\left|H\right\rangle_i\right], \tag{2.8}$$

where $\left|V\right\rangle$ and $\left|H\right\rangle$ are the vertical and horizontal states respectively and s and i denote the signal and idler. A measure of entanglement is determined through coincidence C, which is evaluated via the single count rates at each detector and is defined as [70]:

$$C = \frac{(N_A)(N_B)\tau}{t}, \tag{2.9}$$

where N_A and N_B are the single counts measured at detectors A and B respectively, τ is the time resolution which is an indication of how far apart incidents must be for the system to register them and t is the integration time. Furthermore the coincidence counts or pair detection efficiency is measured by considering the quantum efficiencies, the detectors' apertures and the transverse spatial correlation between the two photons. The coincidence efficiency is determined by [71]:

$$\eta_{AB} = \frac{C}{\sqrt{N_A N_B}}. \tag{2.10}$$

It is assumed that C is corrected for accidental coincidence counts whereby the accidental count rate is given by [70]

$$C_{\text{acc}} = N_A N_B \tau, \tag{2.11}$$

and that N_A and N_B are also corrected for background and dark counts. Assuming that the two detectors have quantum efficiencies η_A and η_B, the limit for η_{AB} in a lossless optical system is $\sqrt{\eta_A \eta_B}$ [71]. The practicality of coincidence counts will be further discussed in Chapter 3 when quantifying the degree of entanglement within an optical system.

2.3.1 Testing for Entanglement

Prior to checking for the violation of the CHSH inequality and verifying entanglement, a test of visibility is used to determine the correlation of the entangled photon pairs. The visibility is measured in both bases (rectilinear and diagonal) by considering the maximum and minimum coincidence according to the following condition:

$$V = \frac{C_{\mathbf{max}} - C_{\mathbf{min}}}{C_{\mathbf{max}} + C_{\mathbf{min}}}, \tag{2.12}$$

where V corresponds to the visibility for a given basis and $C_{\max}$ and $C_{\min}$ are the maximum and minimum coincidence rates, respectively. The error, $\triangle V$, on the visibility is determined by applying the Gaussian error propagation rule:

$$\triangle V = \sqrt{\left(\frac{2C_{\min}}{(C_{\max}+C_{\min})^2}\triangle C_{\max}\right)^2 + \left(\frac{2C_{\max}}{(C_{\max}+C_{\min})^2}\triangle C_{\min}\right)^2}. \tag{2.13}$$

The acquired coincidence rates are assumed to be statistically independent Poisson random variables, so that $\triangle C_{\max} = \sqrt{C_{\max}}$ and $\triangle C_{\min} = \sqrt{C_{\min}}$.

The verification of entanglement however, lies in the violation of the CHSH inequality which states that in local realistic theories the absolute value of a particular combination of correlations between two particles is bounded by 2 [12]. The CHSH test is the experimental realisation of the Bell's test which is used to examine the hypothesis of the local hidden variable theory prescribed by EPR [9].

For the basis of this analysis two spacially separated independent individuals, Alice and Bob, are considered. The hidden variable theory aims at understanding the basis of locality and realism. The following two assumptions pertaining to the locality and realism conditions are considered:

Locality condition: The outcome of Alice's measurement is independent of the settings of Bob's measurement and vice versa.

Realism condition: The correlation between Alice and Bob measurements can be accounted for by some hidden variable theory. This basically means that the correlation that exists between the measurements can be explained by some unknown hidden variable that is arranged at the source.

A generalised case is considered which can be applied to a system other than the spin of two particles. For this realisation a two component system is considered and a pair of instruments which can be used to measure the outcomes of the system. The two components are assumed to be particles. Each instrument has a range of settings and the possible result of a measurement is taken to be ± 1. These instrument settings will be denoted as α for the first instrument and β for the second instrument. To keep with known notation for the purpose of this explanation λ is taken to account for all hidden variables.

From the aforementioned locality condition it can be deduced that the measurement outcome of Alice and Bob are independent of each other and hence the combined probability can be decoupled and be expressed as a product of the individual measurement probability

given by the correlation function in the form of

$$E(\alpha,\beta) = \int A(\alpha,\lambda)B(\beta,\lambda)f(\lambda)d\lambda, \tag{2.14}$$

where $A(\alpha,\lambda) = \pm 1$ and $B(\beta,\lambda) = \pm 1$ are the measurement outcome acquired by Alice and Bob respectively, $f(\lambda) \geq 0$ is the probability density function dependent upon the hidden variable λ and $\int f(\lambda)d\lambda = 1$. The properties of $E(\alpha,\beta)$ can be reduced to a mathematical execise where the restriction on $A(\alpha,\lambda) = \pm 1$ and $B(\beta,\lambda) = \pm 1$ can be expressed as:

$$|A(\alpha,\lambda)| \leq 1 \tag{2.15}$$

and

$$|B(\beta,\lambda)| \leq 1. \tag{2.16}$$

By considering two alternative settings α and α' for the first instrument and β and β' for the second instrument, the difference in correlation function can be expressed as

$$E(\alpha,\beta) - E(\alpha,\beta') = \int \left[A(\alpha,\lambda)B(\beta,\lambda) - A(\alpha,\lambda)B\left(\beta',\lambda\right)\right] f(\lambda)d\lambda \tag{2.17}$$

$$= \int \left[A(\alpha,\lambda)B(\beta,\lambda)\left\{1 \pm -A\left(\alpha',\lambda\right)B\left(\beta',\lambda\right)\right\}\right] f(\lambda)d\lambda$$

$$- \int \left[A(\alpha,\lambda)B\left(\beta',\lambda\right)\left\{1 \pm -A\left(\alpha',\lambda\right)B(\beta,\lambda)\right\}\right] f(\lambda)d\lambda.$$

Using Equation (2.15) and (2.16) the correlation function can be re-written as

$$\left|E(\alpha,\beta) - E(\alpha,\beta')\right| \leq \int \left|\left[1 \pm A\left(\alpha',\lambda\right)B\left(\beta',\lambda\right)\right]\right| f(\lambda)d\lambda \tag{2.18}$$

$$+ \int \left|\left[1 \pm A\left(\alpha',\lambda\right)B(\beta,\lambda)\right]\right| f(\lambda)d\lambda$$

$$= 2 \pm \left[E(\alpha',\beta') + E(\alpha,\beta)\right].$$

This implies that with any local hidden-variable theory the Bell inequality, S, experimetally realised to be the CHSH inequality can only be less than or equal to 2 as seen

below

$$S(\alpha,\alpha^{'},\beta,\beta^{'}) = E[\alpha,\beta] - E[\alpha.,\beta] + E[\alpha^{'},\beta] + E[\alpha^{'},\beta^{'}] \leq 2, \tag{2.19}$$

where $E[\alpha,\beta]$ is the normalised expectation value given by:

$$E[\alpha,\beta] = \frac{C(\alpha,\beta) - C(\alpha_{\perp},\beta) - C(\alpha,\beta_{\perp}) + C(\alpha_{\perp},\beta_{\perp})}{C(\alpha,\beta) + C(\alpha_{\perp},\beta) + C(\alpha,\beta_{\perp}) + C(\alpha_{\perp},\beta_{\perp})}, \tag{2.20}$$

and $C(\alpha,\beta)$ denotes the coincidence count rate obtained for the combination of polariser settings. Here$\alpha_{\perp}$and $\beta_{\perp}$ are the perpendicular polarisation orientation. The statistical nature of the inequality requires that sufficiently long integration time for collecting the required coincidence rates.

The standard deviation of the experimental value is obtained by applying the sum rule represented as follows:

$$\triangle S(\alpha,\alpha^{'},\beta,\beta^{'}) = \sqrt{\sum_{\alpha=\alpha,\alpha'} \sum_{\beta=\beta,\beta'} \triangle E(a,b)^2}, \tag{2.21}$$

where the errors $\triangle E(a,b)$ on the individual correlation coefficients are computed via Gaussian error propagation as:

$$\triangle E(a,b) = 2\left[\frac{[C(\alpha,\beta)+C(\alpha_{\perp},\beta_{\perp})]\,[C(\alpha_{\perp},\beta)+C(\alpha,\beta_{\perp})]}{C(\alpha,\beta)+C(\alpha_{\perp},\beta)+C(\alpha,\beta_{\perp})+C(\alpha_{\perp},\beta_{\perp})}\right] \tag{2.22}$$

$$\times\left[\sqrt{\frac{1}{C(\alpha,\beta)+C(\alpha_{\perp},\beta_{\perp})} + \frac{1}{C(\alpha_{\perp},\beta)+C(\alpha,\beta_{\perp})}}\right].$$

The strength of the violation is usually defined in terms of the number of standard deviations which add up into the gap between the experimental value S and the local realistic bound 2 given as:

$$n_{\triangle} = \frac{S-2}{\triangle S}. \tag{2.23}$$

2.3.2 Accounting for the Fidelity of the Generated States

Ideally, a pure entangled state is generated, however, this case is highly unlikely due to implementation limitations. For this reason, the purity of the generated states is determined by performing a state tomography. By constructing the two-photon density matrix

and considering the interference effect of two photons, the fidelity of the system is determined. This is achieved experimentally by assembling an interferometer to verify the interference of two indistinguishable photons at a non-polarising beam splitter. This phenomenon is known as the Hong-Ou-Mandel interference [72].

The experimental indication of the two photon interference is identified by the V-shaped drop in the measure of detected photon pairs towards zero as represented in Figure 2.8. This provides a determination of the time separation between the photon arrivals. In addition, the degree of indistinguishability of two photons is directly associated to the depth in the dip. In the case where two photons impinge on a 50:50 beam splitter, four outcomes are possible as represented in Figure 2.9.

Either both the photons (A and B) are transmitted as in Figure 2.9(a), both photons are reflected shown in Figure 2.9(b), photon A is transmitted while the photon B is reflected seen in Figure 2.9(c) and vice versa in Figure 2.9(d).

In the case of (a) and (b), both detectors at the beam splitter output register photons in coincidence. Hence, the photons are indistinguishable since they have the same wavelength, polarisation and spatial-temporal mode. If the outcome occurs as represented in (c) and (d), where both of the single photons will reach one of the detectors, no coincidence count would result.

By scanning the relative time delay between the two photon arrivals at the beam splitter, the degree of temporal distinguishability is effectively changed and hence the dip in the coincidence counts can be observed. In contrast to the conventional Mach Zehnder and Michelson interferometer, the effect of the Hong-Ou-Mandel interference is independent of the phase stability in both arms. The path difference is only required to be kept constant to a fraction of the photon coherence length. Overall, this interference effect is a method of determining the time interval of photons and is also a reasonably straightforward way of analysing the coherence length of a photon.

Using the Hong-Ou-Mandel interferometer as represented in Figure 2.10, a state tomography can be used to reconstruct the density matrix of an unknown quantum state. In the case of entangled photon pairs the state tomography requires a set of 16 projective measurements indicated by an appropriate setting of the HWP and Quarter Wave Plate (QWP) in Figure 2.10. These are specified by all possible combination of projecting the two photons into either the $|H\rangle$, $|V\rangle$, plus diagonal $|P\rangle$ or right circular $|R\rangle$ states where $|P\rangle$ and $|R\rangle$ are defined as

$$|P\rangle = \frac{1}{\sqrt{2}}\left[|H\rangle + |V\rangle\right] \tag{2.24}$$

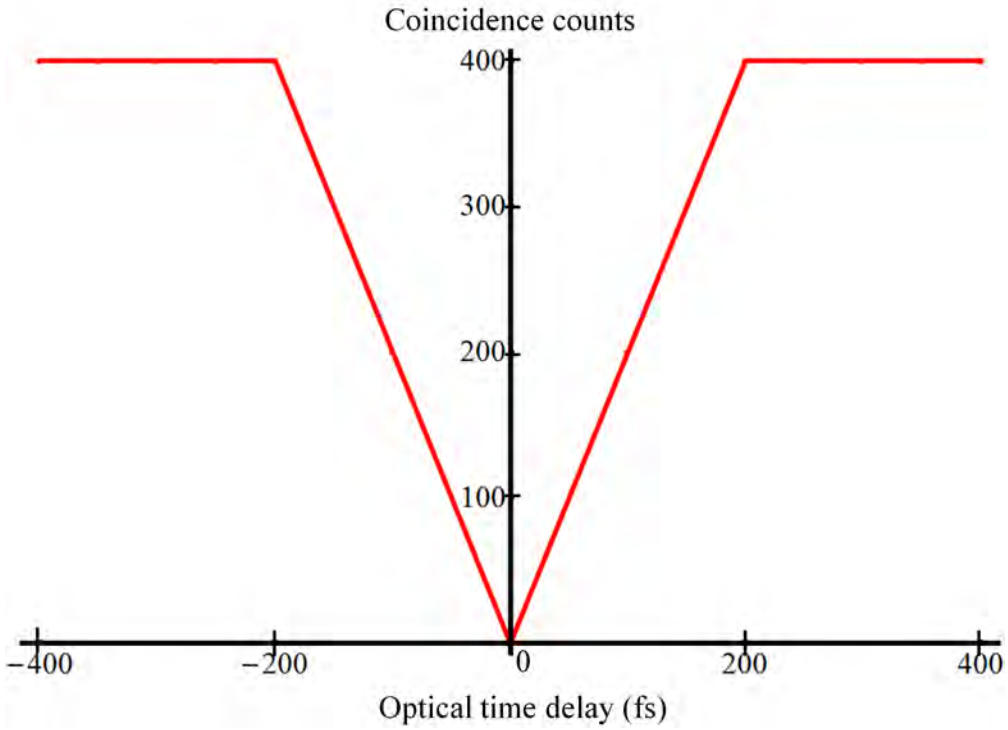

Figure 2.8: The experimental indication of the two photon interference is identified by the V-shaped drop in the measure of detected photon pairs towards zero where the optical time delay is given in femtoseconds (fs).

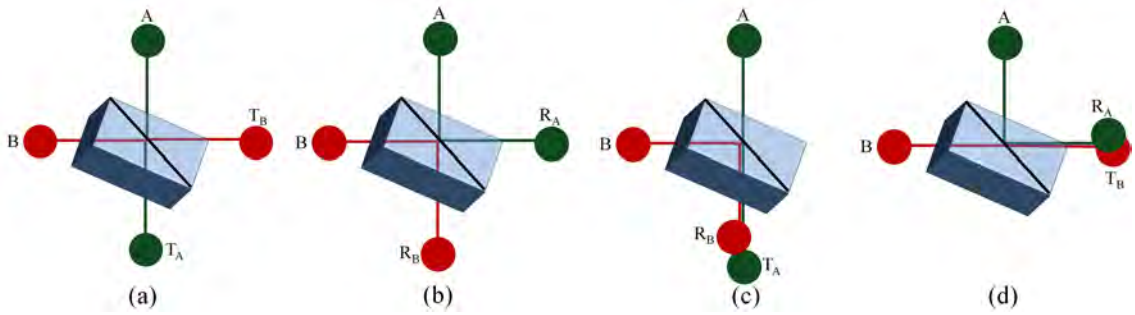

Figure 2.9: Two photons impinge on a 50:50 beam splitter where photon 1 is represented in green (A) and photon 2 is represented by red (B): (a) and (b), both detectors at the beam splitter output register photons in coincidence. In this case both photon A (green) and photon B (red) are transmitted denoted by $T_A$and T_B respectively. The photons are indistinguishable since they have the same wavelength, polarisation and spatial-temporal mode. In the case of (c) and (d), however, where both of the single photons will reach one of the detectors, no coincidence counts would result. In (c) photon A (green) is transmitted (T_A) and photon B (red) is reflected (R_B) at the beamsplitter. For the case of (d) however, photon A (green) is reflected (R_A) and photon B (red) is transmitted (T_B).

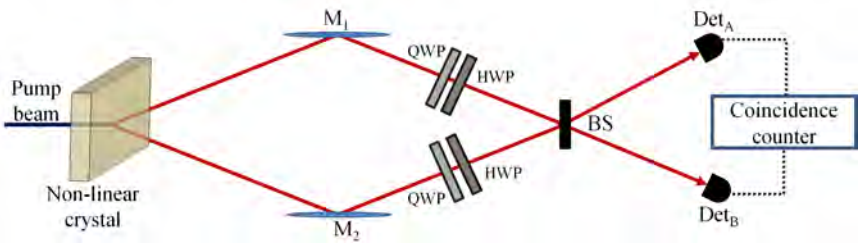

Figure 2.10: Schematic of a Hong-Ou-Mandel interferometer used to carry out the state tomography on the generated states in order to reconstruct the density matrix and determine the fidelity of the system. The photon pairs are generated by pumping a non-linear crystal. The generated photons are transmitted to a Half Wave Plate (HWP) and Quarter Wave Plate (QWP) via mirror (M_1 and M_2). The HWP and QWP are used to set the orientation for the 16 projective polarisation states. The photons propagate through a 50:50 beam splitter (BS) and are detected by detectors, Det_A and Det_B ,which are connected to a coincidence counter.

and

$$|R\rangle = \frac{1}{\sqrt{2}}\left[|H\rangle + i|V\rangle\right] \tag{2.25}$$

respectively. These states are possible pure polarisation states constructed from the superposition of $|H\rangle$ and $|V\rangle$.

To quantitatively characterise the fidelity of the system, the deviation of the experimental density matrix from the ideal case is considered. This is determined by taking into account the overlap of the experimental density matrix with respect to the theoretical density matrix represented as [73]:

$$F = Tr[(\sqrt{\rho_{\text{th}}}\rho_{\text{exp}}\sqrt{\rho_{\text{th}}})^{\frac{1}{2}}], \tag{2.26}$$

where F is the fidelity which takes a value between 0 and 1, ρ_{exp} is the experimentally obtained density matrix and ρ_{th} is the theoretically calculated density matrix which is defined to be the Bell state. The maximum value of 1 is obtained if $\rho_{\text{th}} = \rho_{\text{exp}}$ which infers the two states are completely indistinguishable. The mapping of the tomographic density matrix is given by [73]:

$$\rho = \frac{\sum_{v=1}^{16} M_v C_v}{\sum_{v=1}^{4} C_v}, \tag{2.27}$$

where C_v is the coincidence counts for each of the 16 projections and M_v is defined below where $B_{\mu,v} = \langle \psi_v \mid \Gamma_\mu \mid \psi_v \rangle$ and Γ_μ is a set of 16 linearly independent 4×4 matrices while ψ_v are the16 projective states [73]

$$M_v = \sum_{v=4}^{4n} \left(B^{-1}\right)_{v,\mu} \Gamma_\mu . \tag{2.28}$$

3

Experimental Verification of the Quantum Properties of an Entangled Photon Source

Taking into consideration the theoretical aspects of entanglement described previously, this chapter deals with the experimental verification of entanglement. To demonstrate entanglement, an optical system was constructed whereby the most important component is the non-linear crystal which was responsible for the downconversion into single photon pairs. A schematic of the polarisation based entangled source can be found in Figure 3.1. Within this scheme a UV laser (λ= 404 nm) with an output power of 20 mW was used to pump two type-I beta-Barium Borate (BBO) crystals. For alignment purposes the beam was propagated through a spherical and cylindrical lens respectively onto a Half Wave Plate (HWP) set at 22.5° to allow for an equal probability of photons being generated in either crystals and a quartz crystal which compensated for the phase shift caused by the two spatially separated BBO crystals.

The photons of the pump beam (λ = 404 nm) upon encountering the BBO crystal have a small possibility ($\approx 10^{-11}$ for standard material) of being absorbed and thereafter re-emitted as a pair of single photons at a wavelength of 808 nm. Within the aforementioned optical scheme the two BBO crystals were mounted orthogonal with respect to each other. The first BBO crystal was responsible for the generation of vertically polarised photon pairs while the second one accounted for the generation of the horizontally polarised photon pairs. This allowed for equal probability of both pairs being produced and resulted in the generation of the desired Bell state

$$\left|\psi^{\pm}\right\rangle = \frac{1}{\sqrt{2}}\left[\left|H\right\rangle_1\left|H\right\rangle_2 \pm \left|V\right\rangle_1\left|V\right\rangle_2\right], \tag{3.1}$$

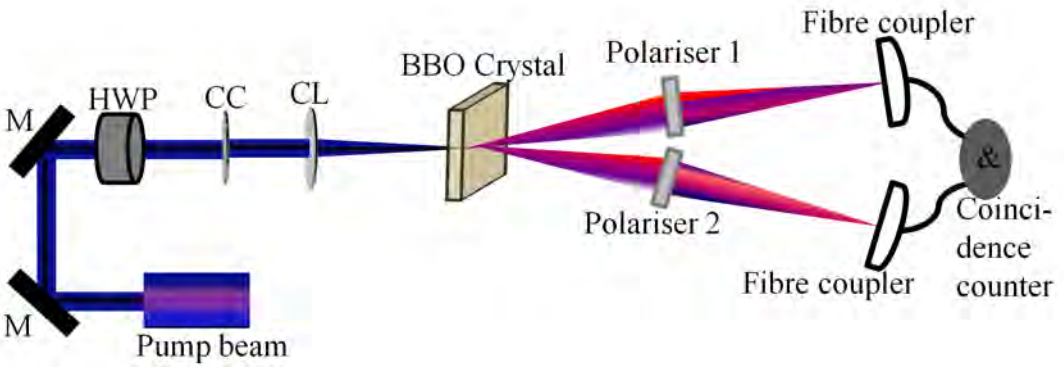

Figure 3.1: Schematic of an entangled source comprising of a pump laser lasing as 404 nm, a few alignment optics (mirrors (M) and cylindrical lens (CL)), a Half Wave Plate (HWP), a crystal compensator (CC), BBO crystal, a polariser in each arm and fibre couplers connected to a coincidence counter via single mode fibres containing a pair of single photon avalanche detectors .

which is required to test for the violation of the CHSH inequality as represented by Equation (2.19).

Since the properties of an entangled photon, namely its state of polarisation, remains unknown until a measurement is carried out, a polariser was placed in each arm of the source, to determine the state of polarisation of the photon pairs. The single photons were detected by avalanche single photon detectors which were embedded in a coincidence counter connected via single mode fibres. This system, as described, can be used to verify the visibility of both the rectilinear and diagonal bases and test for entanglement by violating the CHSH inequality.

To test for the fidelity of the system, further adaption of the system was required. This was achieved by considering the interference of the photon pairs generated. For the purpose of the experimental demonstration of the distinguishability of the photons pairs, instead of constructing a traditional interferometer, a balanced beam splitter was assembled by making use of a fused 50:50 polarisation maintaining fibre coupler. The adaptation of the optical system is represented in Figure 3.2 whereby the photon pairs were directed towards a 50:50 polarisation maintaining fibre coupler, which was used as a beam splitter, via a transmitting collimator. Both arms of the two photon interferometer contained a short free space optical line.

The length of one of the optical lines remained fixed while the other line was varied by means of a manual micrometer translation stage. This made it possible to tune the path difference between the two optical arms. The outputs of the 50:50 polarisation maintaining fibre coupler were connected via a receiving collimator to the coincidence counter by means of single mode fibres in order to measure the coincidence. A HWP and QWP were placed in both arms to vary the polarisation such that the coincidence counts could

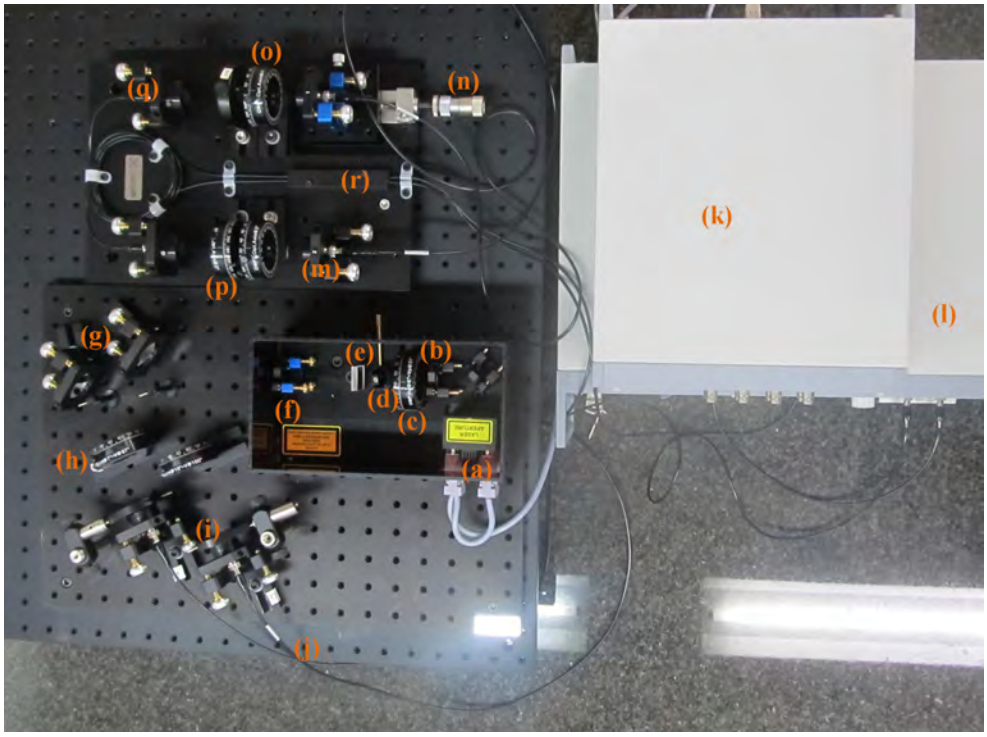

Figure 3.2: Optical system constructed to generate and characterise single photon pairs: (a) UV pump laser lasing at 404 nm, (b) spherical lens, (c) Half Wave Plate (HWP), (d) crystal compensator, (e) cylindrical lens, (f) BBO crystal, (g) mirrors, (h) polarisers, (i) fibre couplers, (j) single mode fibre, (k) Time to digital convertor, (l) coincidence counter embedded with single photon detectors, (m) transmitting collimators, (n) manual micrometer translation stage (o) Quarter Wave Plate (QWP), (p) HWP, (q) receiving collimator and (r) is the 50:50 polarisation maintaining fibre coupler.

be measured for the various projective permutation required to reconstruct the density matrix from which the fidelity of the system was determined.

3.1 Determination of the Visibility of the System

A test for entanglement of photon pairs involves a measurement of correlation curves in two non-orthogonal bases namely the rectilinear and the diagonal bases. This was observed by setting the orientation of polariser 1 in Figure 3.1 to 0° for the rectilinear basis and 45° for the diagonal basis. The orientation of polariser 2 was varied from 0° to 360°, from which the coincidence was measured at each orientation over an integration time of 1s. The dark count of the detectors were measured to be 900 and 1600 cps in detector A and B respectively. The resolution time was set at 26 ns. A plot of the data for the two bases is shown in Figure 3.3.

The resulting visibility was measured to be 91.3 % ± 0.8 % and 90.8 % ± 0.8 % for the rectilinear and diagonal basis respectively which was calculated using Equation 2.12.

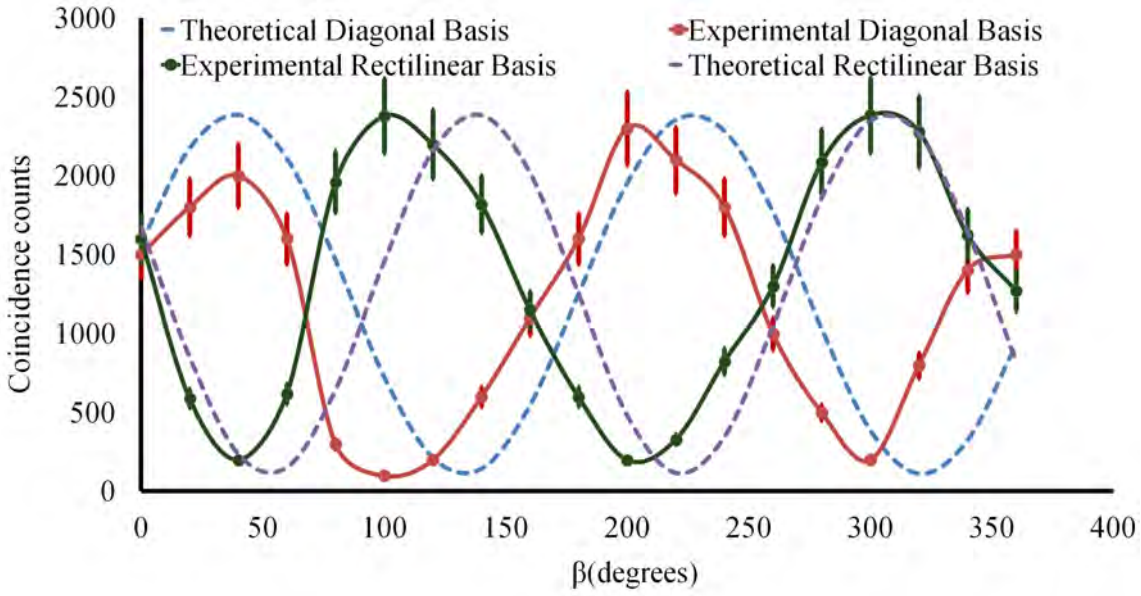

Figure 3.3: Plot representing the correlation of the rectilinear and diagonal bases. The rectilinear basis was measured by setting polariser 1 to 0° while varying the orienation of polariser 2. The orientaion was varied from 0° to 360° and coincidence was measured at each variation. Similarly this was carried out for the diagonal basis except in this case polariser 1 was set at 45°. The green curve is the correlation curve of the experimentally obatained rectilinear basis while the dashed purple is the corresponding theoretical curve, Similarly the red curve is the correlation curve of the experimentally obtained diagonal basis while the dashed blue curve is the corresponding theoretical correlation curve.

The coincidence counts of both bases (rectilinear and diagonal) have a cosine squared dependence and are correlated. There is a phase shift due to slight misalignment. From Figure 3.3 it can also be seen that the mean number of coincidences per second was about 1200 with a noise of about 100 coincidences per second. The coincidences was minimum when the measurement basis were at horizontal and vertical respectively while it was maximum when they were at the same basis.

3.2 Violation of the CHSH Inequality

To test for the violation of the CHSH inequality the following set of orientations were chosen, $\alpha = 0°$, $\alpha' = 45°$, $\beta = 22.5°$ and $\beta' = 67.5°$. Four separate experimental runs were conducted corresponding to the four terms $E[\alpha, \beta]$ in the definition of S, Equation (2.19). Each of the terms $E[\alpha, \beta]$ was calculated from four detections of coincidences making it collectively 16 count rates over an intergration time of 5s.

Using the data obtained during the various experimental runs, as presented in Table 3.1, the violation was measured to be 2.71 ± 0.03. For the theoretical violation of the CHSH

Table 3.1: Data obtained during the 16 permutation used to determine the violation of CHSH inequality. This was achieved by varying the orientation of the polarisers according to the predetermined angles and measuring coincidence. From the coincidence the expectation value, $E(\alpha,\beta)$, for each orientation set was determined. This was used to measure the violation of the CHSH inequality.

Expectation value when α is 0 and β is 22.5 degrees								
α	β	$\alpha_\perp$	$\beta_\perp$	$C(\alpha,\beta)$	$C(\alpha_\perp,\beta)$	$C(\alpha,\beta_\perp)$	$C(\alpha_\perp,\beta_\perp)$	$E(\alpha,\beta)$
0	22.5	90	112.5	8557	1838	1886	8939	0.649
Expectation value when α' is 45 and β is 22.5 degrees								
α'	β	$\alpha'_\perp$	$\beta_\perp$	$C(\alpha',\beta)$	$C(\alpha'_\perp,\beta)$	$C(\alpha',\beta_\perp)$	$C(\alpha'_\perp,\beta_\perp)$	$E(\alpha',\beta)$
45	22.5	135	112.5	11296	2253	1041	10442	0.737
Expectation value when α is 0 and β' is 67.5 degrees								
α	β'	$\alpha_\perp$	$\beta'_\perp$	$C(\alpha,\beta')$	$C(\alpha_\perp,\beta')$	$C(\alpha,\beta'_\perp)$	$C(\alpha_\perp,\beta'_\perp)$	$E(\alpha,\beta')$
0	67.5	90	157.5	2950	10707	7238	1642	-0.592
Expectation value when α' is 45 and β' is 67.5 degrees								
α'	β'	$\alpha'_\perp$	$\beta'_\perp$	$C(\alpha',\beta')$	$C(\alpha'_\perp,\beta')$	$C(\alpha',\beta'_\perp)$	$C(\alpha'_\perp,\beta'_\perp)$	$E(\alpha',\beta')$
45	67.5	135	157.5	13180	1692	2070	11211	0.732

inequality, it is expected that the S-value tends to $2\sqrt{2}$, we obtained a value 3.56 % less than the expected value. This could be due to slight misalignment of our systems. At lower integration time, the coincidence counts tends to fluctuate, which resulted in higher accidental counts. This will also lower the S-value obtained.

3.3 Determination of the Fidelity of the System

Although the violation of the CHSH inequality verified entanglement, as a last step in the characterisation of a polarisation based entangled source the fidelity of the system was measured. This was achieved by setting the HWP and QWP to the appropriate orientation as listed in Table 3.2 and measuring the coincidence at each permutation. From the data presented in Table 3.2 the density matrix shown below was reconstructed by making use of the maximum likelihood method [73] represented in Equation (2.27)

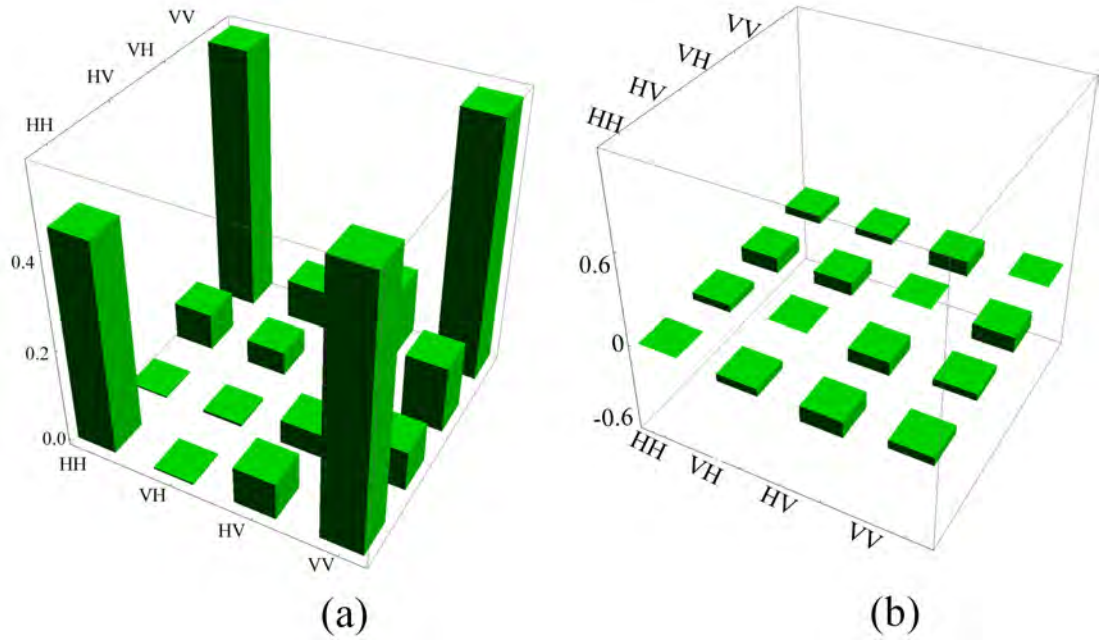

Figure 3.4: Graphical representation of the real (a) and imaginary (b) part of the reconstructed density matrix obtained from carrying out a full tomography of the system where HH is the horizontal-horizontal state, HV is the horizontal-vertical state, VH is the vertical-horizontal state and VV is the vertical-vertical state. It can be noted that the fidelity is almost 1 which means that the states generated are indistinguishable.

$$\rho = \begin{bmatrix} 0.4307 & -0.0035+0.0416i & -0.0788-0.0876i & 0.5511+0.0450i \\ -0.0035-0.0416i & 0.0060 & 0.0515-0.0745i & -0.0850-0.0382i \\ -0.0788+0.0876i & 0.0515+0.0745i & 0.0082 & -0.4129+0.0856i \\ 0.5511-0.0450i & -0.0850+0.0382i & -0.1429-0.0856i & 0.5050 \end{bmatrix}.$$

A graphical representation of the real and imaginary part of the density matrix is illustrated in Figure 3.4. The elements of the imaginary matrix along the diagonal is zero while the off-diagonal elements are measured to be relatively low. The fidelity of the system was determined to be 0.949 ± 0.0001, evaluated using Equation (2.26), by taking the trace of the density matrix. Noticeably the fidelity is almost 1 which means that the states are indistinguishable and that the quantum states are well preserved.

Table 3.2: Experimental data for the 16 polarisation projections used to determine the fidelity of the system represented by the horizontal state, $|H\rangle$, vertical state, $|V\rangle$, plus diagonal state, $|P\rangle$, and the right circular state, $|R\rangle$. This was achieved by setting the Half Wave Plate (HWP 1 and HWP 2) and the Quarter Wave Plate (QWP 1 and QWP 2) in each arm of the inferometer to the appropriate orientations. From the measured coincidence counts, C, the density matrix was reconstructed, where N is the number of different projections.

N	State 1	State 2	HWP 1 (°)	QWP 1 (°)	HWP 2 (°)	QWP 2 (°)	C
1	$\|H\rangle$	$\|H\rangle$	45	0	45	0	23464
2	$\|H\rangle$	$\|V\rangle$	45	0	0	0	320
3	$\|V\rangle$	$\|V\rangle$	0	0	0	0	29018
4	$\|V\rangle$	$\|H\rangle$	0	0	45	0	439
5	$\|R\rangle$	$\|H\rangle$	22.5	0	45	0	16618
6	$\|R\rangle$	$\|V\rangle$	22.5	0	0	0	12636
7	$\|P\rangle$	$\|V\rangle$	22.5	45	0	0	10141
8	$\|P\rangle$	$\|H\rangle$	22.5	45	45	0	16145
9	$\|P\rangle$	$\|R\rangle$	22.5	45	22.5	0	16216
10	$\|P\rangle$	$\|P\rangle$	22.5	45	22.5	45	35426
11	$\|R\rangle$	$\|P\rangle$	22.5	0	22.5	45	14225
12	$\|H\rangle$	$\|P\rangle$	45	0	22.5	45	12079
13	$\|V\rangle$	$\|P\rangle$	0	0	22.5	45	10256
14	$\|V\rangle$	$\|L\rangle$	0	0	22.5	90	10170
15	$\|H\rangle$	$\|L\rangle$	45	0	22.5	90	14109
16	$\|R\rangle$	$\|L\rangle$	22.5	0	22.5	90	24412

4

Behaviour of Polarisation Encoded Entangled Single Photons in Turbulence

Free space quantum communication is a mooted technology of the future, and as such the propagation of entangled photons through the atmosphere has become topical of late. Studies show that polarisation entangled photons are immune to atmospheric turbulence perturbations as the medium is isotropic [74]. While atmospheric turbulence is a stochastic process, there is structure to the randomness. From an optical perspective, the theory of turbulence in air is based on taking into account the variation in refractive index amid points in the atmosphere.

Over the years extensive studies have been carried out in simulating turbulence which includes making use of liquid crystal technology [75, 76, 77, 78, 79]. Thus far, the focus of studies involving simulated turbulence has been on the propagation of states carrying OAM. For instance, it has been shown that for an OAM based entangled system the concurrence [80], which is a measure of entanglement, decays in the presence of simulated turbulence mimicked using a Spatial Light Modulator (SLM) [69, 81]. This has also been expanded to studying the decay of different qutrit states [82]. Recently a method was proposed to investigate the modal distortions of Bessel beams propagating through atmospheric turbulence [48]. In addition, simulated atmospheric turbulence has played a useful role in the study of holographic ghost imaging [83].

This chapter deals with a method of mimicking, in the laboratory, the near and far field turbulence effects on entangled photons in the polarisation basis. This is achieved by making use of a diffractive optical element to simulate turbulence distortions. The aim is to measure the entanglement as a function of the turbulence strength. The non-classical behavior of an entangled single photon source is observed by testing the visibility of the system and verifying the CHSH inequality. The focus here, is on the detection method of single mode fibre coupling of single photon sources, stressing the role that turbulence

effects plays on the overall detection efficiency of the system. It is shown that the standard detection method of single mode fibre coupling to single photon counters results in a spatial mode dependence on the coincidences, even if the entanglement is not measured with spatial modes. The work presented in this chapter is in the process of being prepared for publication.

4.1 Theoretical Background on Turbulence

Turbulence is related with the random velocity fluctuations of particles within a viscous fluid such as the atmosphere [47]. The atmosphere has two discrete states of motion namely that of laminar and turbulent flow. In the case of laminar flow mixing does not occur however this differs with turbulent flow which is characterised by dynamic mixing. A turbulent flow also acquires random secondary flows called turbulent eddies [46]. According to the energy cascade theory, unsteady air masses under the influence of inertial forces disintegrate into smaller eddies to form a range of eddy size for the transfer of energy from a macro-scale, L_0, which is the outer scale of turbulence to a micro-scale, l_0, which is the inner scale of turbulence [46] as shown in Figure 4.1 [84].

Kolmogorov considered the simplified problem of a non-viscous and isotropic atmosphere [46]. In this approach the inner scale is considered to be zero while the outer scale is infinite. Taking these assumptions into consideration lead to a well-defined distribution for the randomness in the refractive index of the atmosphere. This can be applied in the laboratory, giving a good approximation for a real atmosphere [85, 86].

One of the significant outcomes predepicted by Kolmogorov [46, 47] has been that the turbulence strength can be described by a distinct parameter known as the atmospheric structure constant, C_n^2. The structure constant can be defined in terms of the turbulence coherence length, r_0 also known as the Fried's scale parameter [87]. For a plane wave the Fried's parameter is defined by:

$$r_0 = 1.68 \left(C_n^2 D k^2\right)^{\frac{5}{3}}, \tag{4.1}$$

where D is the path length through the turbulent atmosphere, and $k = \frac{2\pi}{\lambda}$ with λ being the wavelength of the light (in vacuum) passing through the atmosphere.

4.1.1 Turbulent Plate

The simulated turbulence medium is achieved by utilising a diffractive plate encoded with turbulence based on Kolmogorov theory. The plate consisted of a 5×5 grid ranging in turbulence whereby the closeness of the pixels depicts the strength of the turbulence as seen in Figure 4.2. The encoding varied across the plate from weak to strong as shown

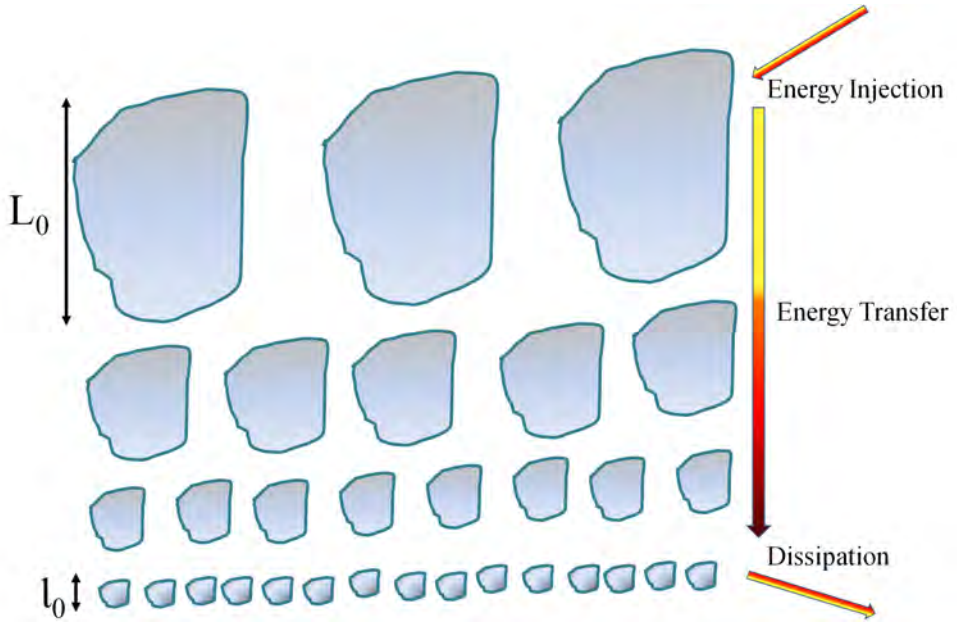

Figure 4.1: Turbulent flow consist of random secondary flows known as turbulent eddies. Disintegration of unsteady air masses into smaller eddies ranging in eddy size for the transfer of energy from a macro-scale, L_0, which is the outer scale of turbulence to a micro-scale, l_0, which is the inner scale of turbulence.

by the grey-scale image in Figure 4.2(a) [88]. The plate was the size of a 2 inch (50 mm) lens shown in Figure 4.2(b). The strength of the plate is visualised by the closeness of the encoded pixels as observed by the magnified image of the plate in Figure 4.2(c).

The strength of the plate is determined based on the Strehl ratio which is the measure of the quality of optical deformation. A good measure of image quality, is to consider the image of a point source in the object plane. This quantity has been defined by Strehl in 1896 and is commonly called the Strehl ratio [89], determined by the variation in optical intensity given by:

$$SR = \frac{I}{I_0} = e^{-\sigma^2}, \tag{4.2}$$

where I is the optical intensity of the abberated field, I_0 is the optical intensity of the unabberated field and σ^2 is the phase error given by:

$$\sigma^2 = 1.03 \left(\frac{d}{r_0}\right)^{\frac{5}{3}}, \tag{4.3}$$

where d is the diameter of the aperture and r_0 is the Fried parameter.

Recall, from Equation (4.1), the Fried parameter r_0, is directly proportional to the atmospheric structure constant, C_n^2. From this it can be deduced that the Strehl ratio exponen-

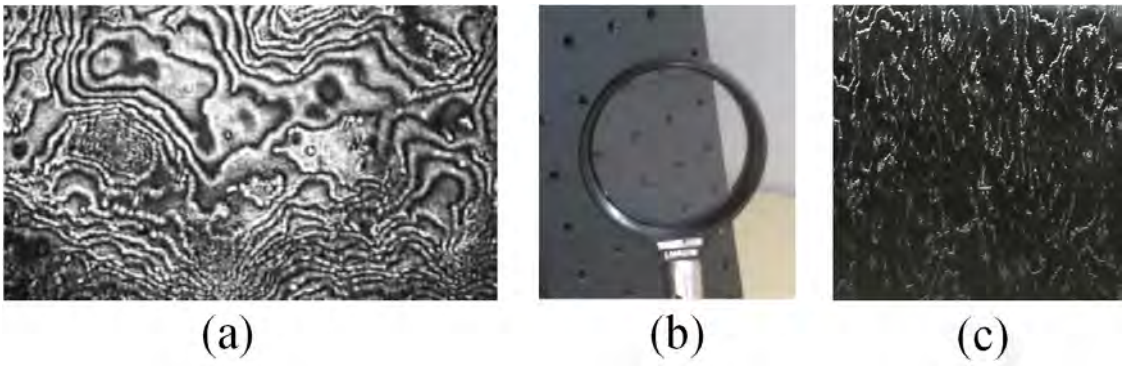

Figure 4.2: Turbulent plate encoded with Kolmogorov theory of turbulence: (a) The encoding of the variation in turbulence strength, (b) turbulent plate and (c) magnified image of the plate showing the variation in the pixels (encoding).

tially decreases as the turbulence strength, C_n^2, increases. In the absence of turbulence, the Strehl ratio (Equation (4.2) is normalised to unity. The change in optical intensity due to turbulence or aberration is graphically represented in Figure 4.3. A Gaussian beam detected in the absence of turbulence maintains its optical intensity (Gaussian profile in red) however in the presence of turbulence there is a loss in detected optical intensity (aberated beam profile in blue). The Strehl ratio is hence determined by the optical peak intensity after aberrations to the optical peak intensity before aberrations.

4.2 Experimental Analysis

The strength of the plate was determined by measuring the intensity of the beam before and after the plate from which the Strehl ratio was obtained. A simple system was constructed to carry out this analysis consisting of a 633 nm He-Ne laser, a Fourier lens and an imaging system. The HeNe laser emitted a Gaussian TEM_{00} mode that was passed through two mirrors for the purpose of aligning the near and the far-field. The turbulent plate was placed on a XYZ translation stage to allow for accurate movement of the plate with a resolution of 149.4 μm translation per revolution. A Fourier lens was placed a focal distance away from the turbulent plate which was imaged by a Spiricon Beamgage CCD Camera placed a focal length (100 mm) away from the Fourier lens, L_1, as represented in Figure 4.4. Note that the imaging of the beam was carried out at the far-field.

For the duration of the measurement a 22 micron aperture was placed at the central region of the initial Gaussian beam (in the absence of the plate). The measurements were obtained by varying the position of the plate until each row of the plate was traversed. The 22 micron aperture remained fixed and a total of ten readings were taken per row such that a fair sample of data was obtained. Since the encoding varied across all the rows, the

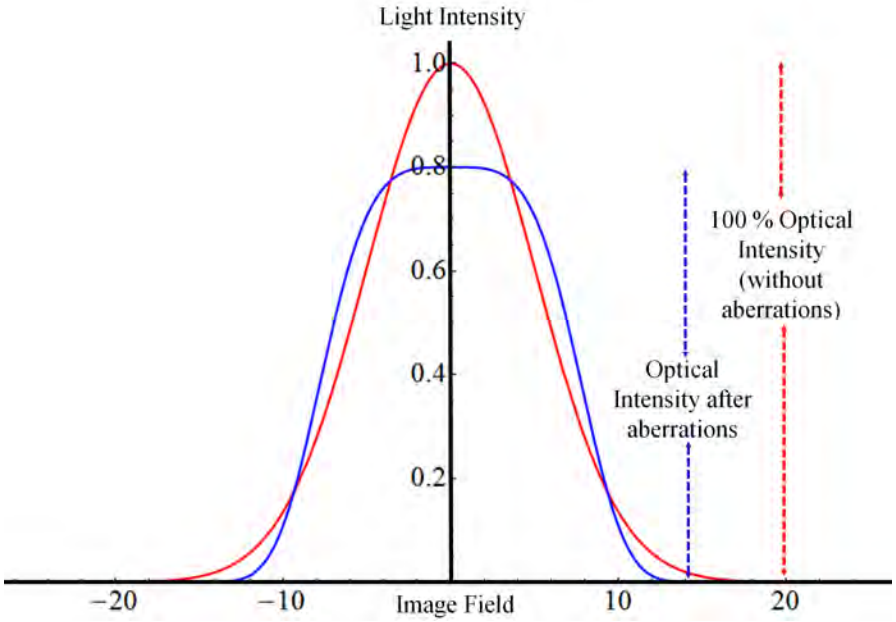

Figure 4.3: The Strehl ratio is the measure of optical deformation determined by considering the intensity profile before and after the turbulent medium. The Guassian beam in the absence of turbulence maintains its optical intensity (Gaussian profile in red) however in the presence of turbulence there is a loss in detected optical intensity (abberated beam profile in blue). The Strehl ratio is hence determined by the optical peak intensity before aberrations to the optical peak intensity after aberrations.

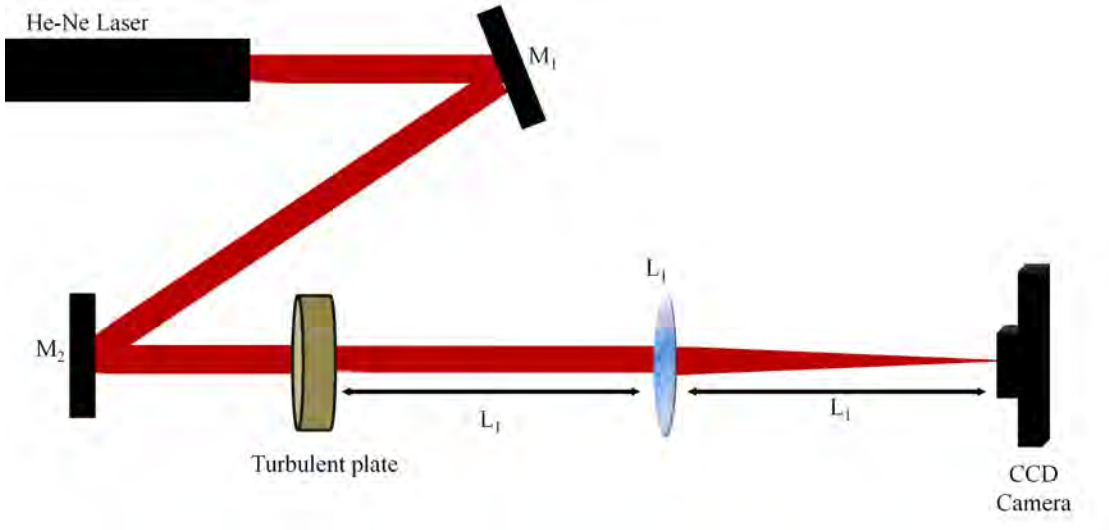

Figure 4.4: Optical system constructed to measure the Strehl ratio comprising of a 633 nm He-Ne laser, mirrors $M_1$and M_2 to align the near and far-field respectively, a Fourier lens and an imaging system. The turbulent plate was placed on a XYZ translation stage and imaged by a Spiricon Beamgage CCD Camera placed a focal length (100 mm) away from the Fourier lens L_1 (far-field) .

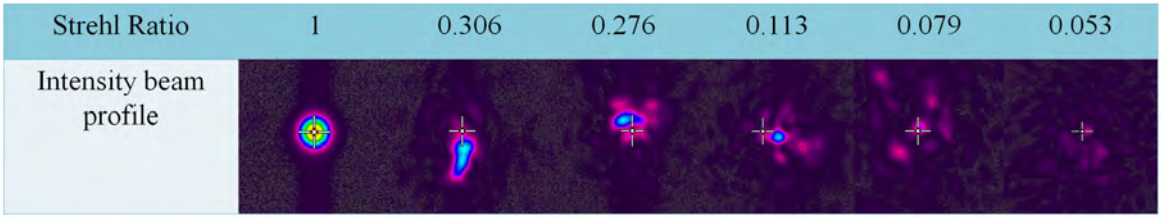

Figure 4.5: Images depicting the break down in intensity of the beams as they pass through the turbulent plate for the various Strehl ratios ranging from 0.306 (weak turbulence) to 0.053 (strong turbulence).

Table 4.1: Measured Strehl ratio for each of the rows of the turbulent plate. As the turbulent strength increases the measured Strehl ratio decreased exponentially.

Rows	Strehl ratio measured
1	0.306 ± 0.234
2	0.276 ± 0.125
3	0.113 ± 0.097
4	0.080 ± 0.060
5	0.050 ± 0.044

intensity of the Gaussian beam was subjected to different conditions causing the beam to wander or scatter accordingly as observed in Figure 4.5.

The initial Guassian beam had a beam diameter of 0.51 mm (SR = 1) however as the turbulent strength increased, the spatial distribution of the beam broke down completely as seen for a SR of 0.053. The Strehl ratio measured for each row is represented in Table 4.1 and a plot of Strehl ratio versus turbulent strength is shown in Figure 4.6.

For each of the rows within the turbulent plate there was a change in the Strehl ratio due to the variation of the enscription. The strongest encoding of turbulence resulted in a Strehl ratio measurement of 0.050 ± 0.044 while the weakest encoding of turbulence resulted in a measurement of 0.306 ± 0.234. The experimental results obtained agreed with the theoretical expectation of the turbulence dependence on the Strehl ratio as depicted in Equations (4.1), (4.2) and (4.3) which shows an increase in the turbulent strength leads to an exponential decrease in the Strehl ratio.

4.2.1 Verification of Non-Classical Properties of the System in the Presence of the Turbulent Plate

For the measurement of the non-classical behavior of the source, both the photons were allowed to propagate through the simulated turbulent medium as seen in Figure 4.7. The non-classical properties of the system was tested for each of the rows of turbulent strength

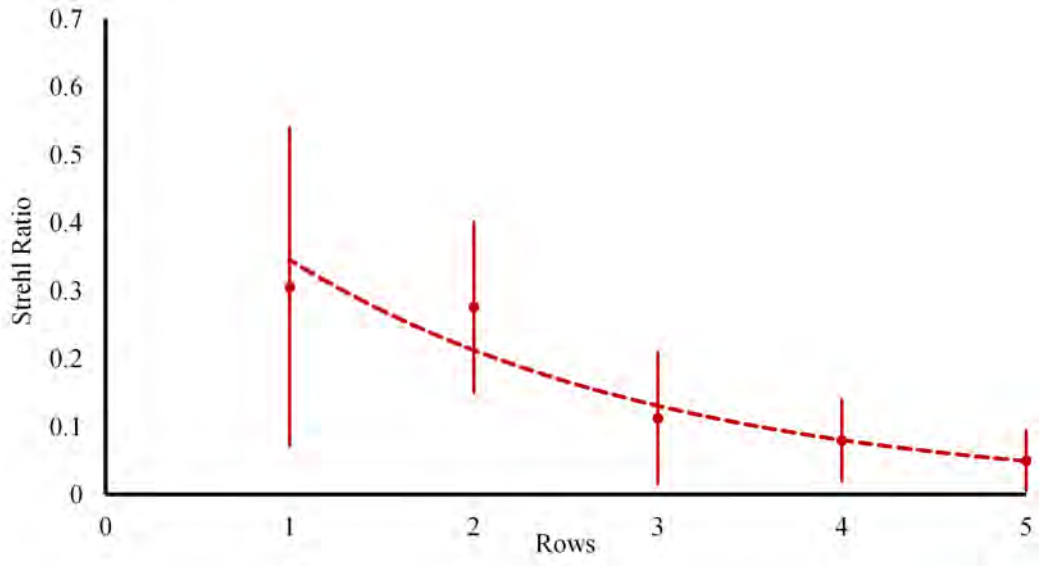

Figure 4.6: Plot of Strehl ratio, which is the measure of optical deformation, of a Gaussian beam as it traversed through various rows of the turbulent plate. As the turbulent strength increases the measured Strehl ratio decreased exponentially

by carrying out the violation of the CHSH inequality. The same analysis was carried as discussed theoretically in Chapter 2 and experimentally in Chapter 3. It was observed that in the absence of turbulence the violation obtained was 2.71 $\pm$ 0.03 however in the case of the weakest and strongest turbulence a violation of 2.61 $\pm$ 0.05 (SR = 0.306) and 2.41 $\pm$ 0.04 (SR = 0.05) was measured respectively. This is further illustrated in Figure 4.8. Although the violation varied for each of the SR measurements, the CHSH inequality was measured to be greater than the classical bound of 2 for all cases.

From these result it can be deduced that an increase in turbulence strength leads to decrease in the intensity of the beam (see Figure 4.5) which results in a decrease of the coupling efficiency of the single mode fibre within the detection scheme. This agrees with the theoretical expectation of the coupling efficiency of single mode fibre in the presence of turbulence, defined as [90]

$$\langle \eta \rangle = 2\pi \exp\left(-2\frac{3.83^2}{4}\frac{1}{(w/w_0)^2}\right) \times I^2_{\frac{1}{2}}\left(\frac{3.83^2}{8}\frac{1}{(w/w_0)}\right), \tag{4.4}$$

where $I^2_{\frac{1}{2}}$ is the intensity of the beams and w_0 and w is the beam waist and beam width respectively. Apart from measuring the violation of the CHSH inequality the visibility of both the rectilinear and the diagonal bases were measured for each of the turbulence strengths. This was determined by measuring the maximum and minimum coincidence which is summarised in Table 4.2 and plotted in Figure 4.9. It was observed that as the strength of the turbulence increased, the visibility in both bases (rectilinear and diagonal)

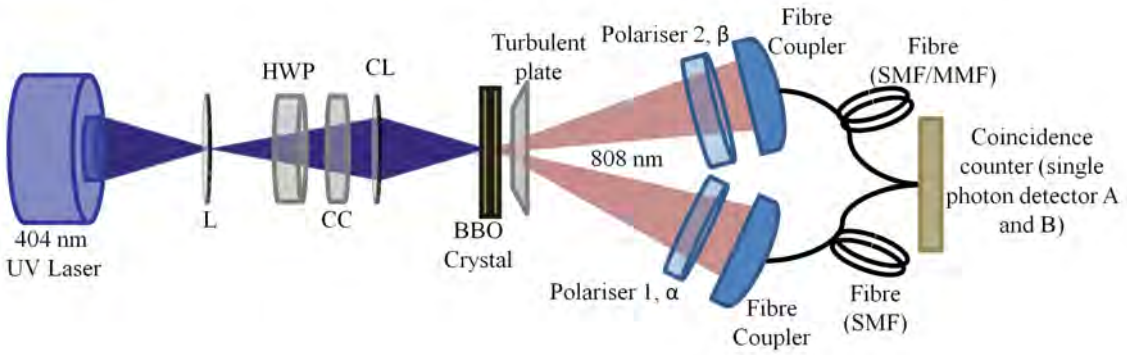

Figure 4.7: Optical system designed to test the non-classical properties of single photons within a turbulent medium. Schematic of an entangled photon source comprising of a pump laser (UV Laser), lasing at 404 nm, lens (L), a Half Wave Plate (HWP), a Crystal Compensator (CC), Cylindrical lens (CL), a type-I concatenated BBO crystal, turbulent plate, a polariser in each arm (polariser 1 and 2) followed by a fibre coupler connected to a coincidence counter comprising of single photon avalanche detectors A and B via single mode (SMF) and multimode fibre (MMF).

decreased. In the absence of turbulence the visibility was measured to be 89.5 % $\pm$ 4.46 % for both bases. Similar to the variation of the CHSH inequality, the variation in visibility was also due to the inefficient coupling of the single mode fibre as represented in Equation (4.4).

Identifying the Problem with the Inefficiency of the System

From the results obtained thus far using the turbulent plate, a decrease in the quality of entanglement for the various Strehl ratios was observed. This variation was not expected as it is well known that the change in polarisation state in negligible when passing through the atmosphere [74]. The discrepencies of results lies in the use of single mode fibre within the detection scheme.

Most polarisation based single photon sources are built using single mode fibre coupling the measurement and detection process. Under ideal conditions the system will function adequately however under non-ideal condition single mode fibre tends to decrease in efficiency due to the influences of spatial mode dipersion. Single mode fibre will efficiently couple modes that are TEM_{00}.

The presence of the turbulent plate caused the intensity of the beam to break-up (beam scattering and wandering) which resulted in a spatial mode dependence on the measured coincidence. Since the single mode fibre was unable to efficiently couple the scattered

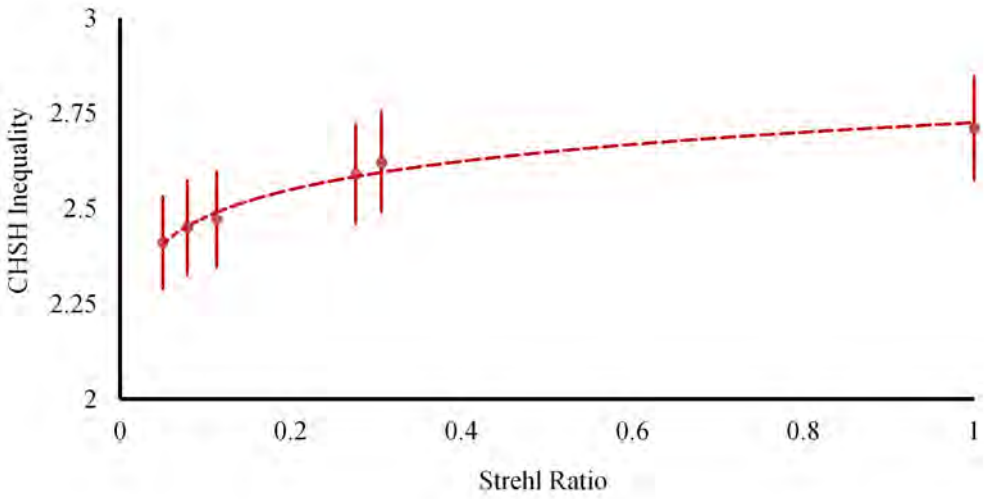

Figure 4.8: Plot representing the violation of the CHSH inequality for various turbulence strengths. As the turbulent strength increased, the violation of the CHSH inequality decreased. Although the violation varied for each of the SR measurement, the CHSH inequality was measured to be greater than the classical bound of 2 for all cases. An increase in turbulence strength leads to decrease in the intensity of the beam which results in a polynomial decrease of the coupling efficiency

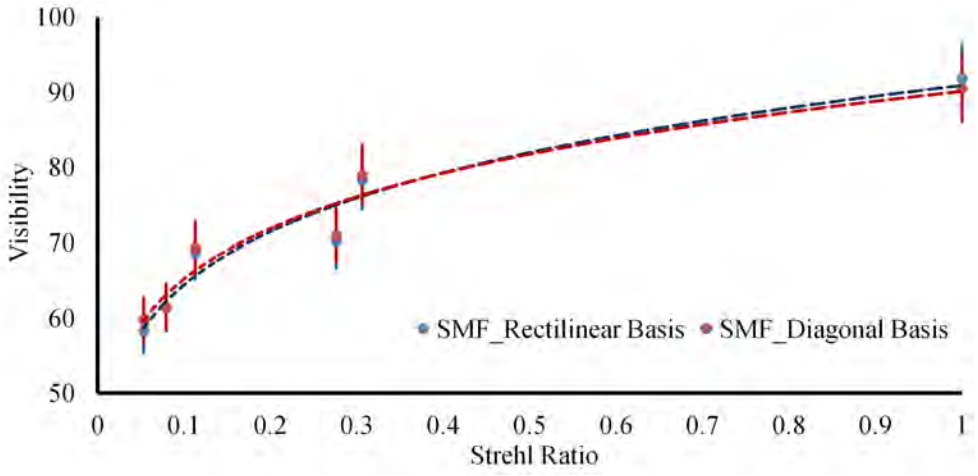

Figure 4.9: Visibility measurement for both the rectilinear (blue curve) and diagonal bases (red curve) passing through various turbulence strengths. It was observed that as the strength of the turbulence increased, the visibility in both bases (rectilinear and diagonal) decreased resutling in a polynomial decrease in coupling efficiency.

Table 4.2: Coincidence counts measured for each turbulent strength for the rectilinear and diagonal bases. This was obtained by setting polariser 1, α , to 0° for the rectilinear basis and 45° for the diagonal basis while varying the orientation of polariser 2, β, in increments of 20° from 0° to 360°. The coincidence was measured at each orientation. From the maximum coincidence, C_{max}, and the minimum coincidence, C_{min} ,the quality of entanglement was determined.

	Rectilinear basis ($\alpha = 0^\circ$)			Diagonal basis ($\alpha = 45^\circ$)		
Strehl ratio	C_{max}	C_{min}	Visiblity (%)	C_{max}	C_{min}	Visiblity (%)
1	2965	167	89.50±4.46	2591	143	89.54±4.48
0.306	2284	278	78.30±3.92	1881	251	76.45±3.82
0.276	2605	465	69.71±3.49	2064	338	71.86±3.59
0.113	1400	240	68.67±3.38	1490	270	69.32±3.47
0.080	1300	270	61.43±3.07	2640	630	61.47±3.07
0.050	950	250	58.33±2.91	1310	330	59.76±2.98

light, it was compensated for by using multimode fibre instead. Multimode fibre is not affected by the variation in intensity, which in this case is caused by the turbulent medium [91], since it accepts all modes not only TEM_{00}. One of the challenges that was faced when replacing the coupling fibres was the saturation of the detectors which was overcomed by replacing only one of the single mode fibres in the scheme presented in Figure 4.7.

4.2.2 Verification of Entanglement Using Multimode Fibre to Improve the Coupling Efficiency

The coupling inefficiency of the single mode fibre is apparent as it was observed that the visibility decreases as the turbulent strength increases as represented in Figure 4.9 as well as in the case of the violation of the CHSH inequality in Figure 4.8. Replacing one of the single mode fibres with a multimode fibre resulted in an increase in the coupling efficiency. Carrying out the same analysis as for the case of the single mode fibre, the visibilty did not change drastically as the turbulent strength was increased as observed in Figure 4.10. In the case of multimode fibre, the visibility at the various Strehl ratios was centered on 89.92% ± 2.65% .

There was also an improvement in the CHSH inequality measurements using a single and multi mode fibre combination. For the various Strehl ratios the CHSH inequality measured was centered on 2.695 ± 0.05 as observed in Figure 4.11. This is due to coupling of multimode fibre is independent on the intensity of the beam as well as mulitmode

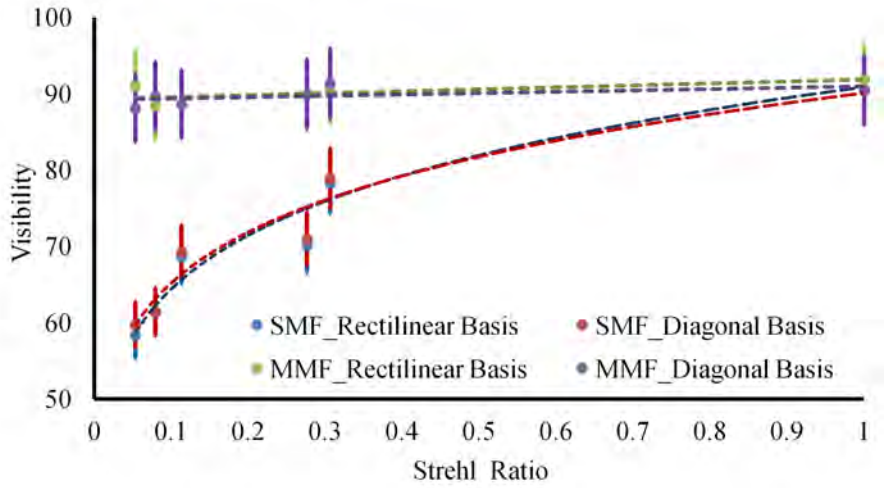

Figure 4.10: Quality of entanglement for the various Strehl ratios for the rectilinear and the diagonal bases using single mode (light blue curve for the rectilinear basis and the red curve for the diagonal basis) and a multimode fibre (light green line for the rectilinear basis and the purple line for the diagonal basis). Single mode fibre was unable to efficiently couple light into detector resulting in the degradation of the quality of entanglement. Multimode fibre did not suffer from mode selection hence the visibility measured was constant for the various Strehl ratios. This is due to multimode coupling being independent of the intensity of the beam.

fibre has a larger core radius than single mode fibre which means it accepts all modes, $TEM_{nm\ [91]}$.

The instrumentation of single photon sources is vital when conducting experiments under non-ideal conditions. Mode selection of the fibre due to scattered light influenced the overall coupling efficiency of the detected coincidence caused by spatial mode dispersion. It can be deduced that utilising the source presented in Figure 4.7, there is a significant likelihood that the entanglement will survive even for the strongest turbulence within a QKD link. These results suggest that care is required in the choice of detection schemes for free space quantum communication systems.

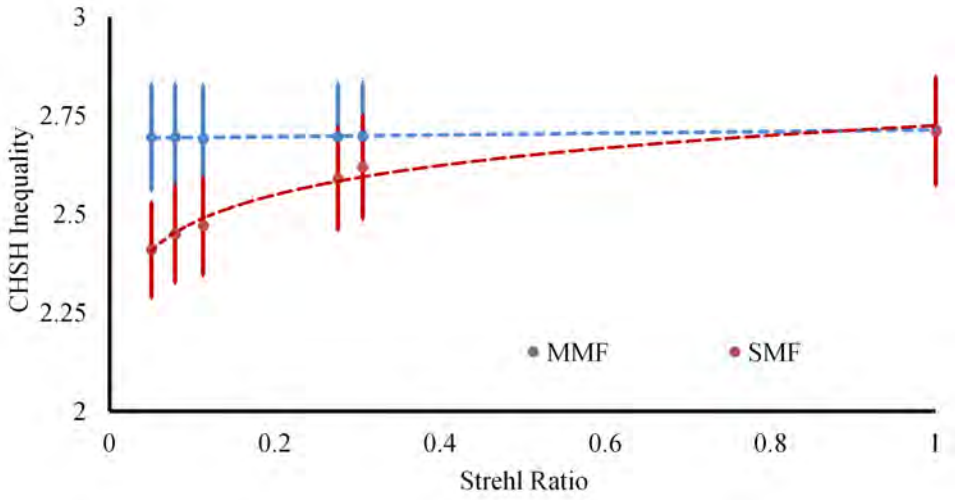

Figure 4.11: Verification or entanglement for the various Strehl ratios using single mode (red curve) and a multimode fibre (blue line). Single mode fibre suffers from mode selection due to the breakdown of the spatial mode caused by the turbulent plate. This leads to a polynomial decrease in the coupling efficiency of the fibre and hence polynomial decrease in the measure of the CHSH inequality. Multimode fibre was able to cope with spatial mode dispersion and hence efficiently couple the light into the detectors. This is due to multimode fibre being independent of the intensity of the beam.

5

Higher dimensional Entanglement: A Means to Reach an Infinite State Space

An alternative approach to encoding single photons for optical communication is through the use of spatial modes of light. These are single photons encoded with helical phase structures which carry a quantised amount of OAM [66]. There exist a family of beams which have these helical structures which include Laguerre-Gaussian (LG) [66], Bessel-Gaussian (BG) [92] and Bessel-Like Beams (BLB) [93]. Many studies have considered producing higher dimensional entanglement systems using LG beams. An alternative approach would be to make use of Bessel beams however not much work has been done on the topic of two-dimensional detection of such modes [94, 95, 96]. This Chapter focuses on the detection of Bessel beams by a simple scheme consisting only of a helical axicon and a lens. The concept of generating these beams is outlined and implemented optically. Experimentally these beams are generated with a digitally encoded phase-only holograms. The self-healing property of Bessel beams after an obstruction is discussed. Of emphasis however is the propagation of these beams through turbulence resulting in the changing radial and azimuthal spectrums observed for the first time. This is significant for future studies in optical communication since Bessel beams carry OAM over extended distances in a nominally non-diffracting manner which may be beneficial for signal delivery to distance receivers. This work was published in Optics Express [48].

5.1 Encoding of OAM States

There are numerous experimental methods to produce beams carrying OAM [66, 97, 98, 99, 100]. Beijersbergen *et al*. were the first to demonstrate the existence of LG beams by a method known as mode conversion [97]. This method makes use of two cylindrical lenses that are used to define a region in which the Gouy phase of a beam can be manip-

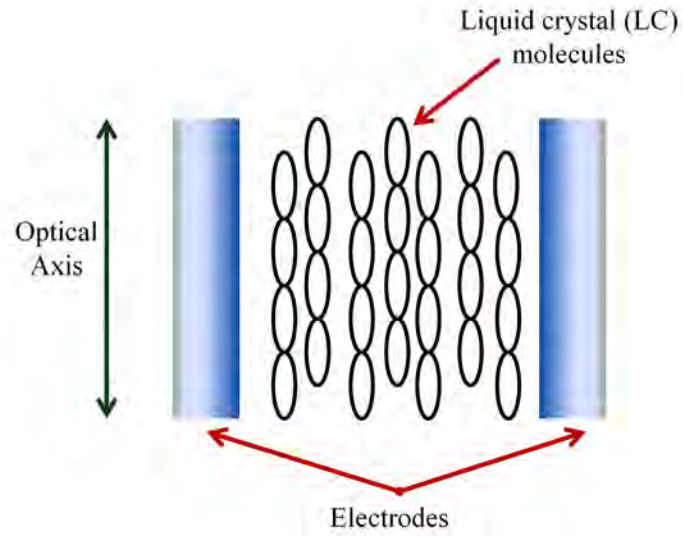

Figure 5.1: A SLM is a liquid crystal device comprising of birefringent molecules arranged in a lattice formation between two electrodes. They consist of 1920 $\times$ 1080 pixels each having a a dimension of 8 μm.

ulated. By enforcing a $\pi/2$ phase shift on a Hermite-Gaussian beam they were able to convert this beam to a LG beam. However there are easier approaches which include the use of diffractive optics, namely phase plates, demonstrated for the first time by Bazhenov *et al.* [101] where a hologram with a screw dislocation was etched onto a plate in order to generate LG beams of azimuthal index ± 1 depending on the left and right handedness of the forked pattern. Other methods include making use of digital holography which is the most cost effective method. This requires the use of a SLM, which is a liquid crystal device that is electronically addressed such that the phase of the incoming beam is modulated to produce the desired field. There exist other beams which also carry OAM such as higher-order Bessel beams which are enveloped by LG beams [102]. Also, Mathieu beams [103] and Ince-Gaussian beams [104] which are the explicit solution to the wave equation in elliptical cylindrical coordinates and which complete the family of beams that carry OAM.

Utilising a SLM for the Encoding

A SLM is a liquid crystal device that is electronically addressed by a circuit board in order to modulate the phase or amplitude of light. The liquid crystal is made up of birefringent molecules arranged in a lattice formation enclosed by two electrodes as seen in Figure 5.1. The main characteristic of these crystals is that they are birefringent. They are arranged such that they consist of 1920 $\times$ 1080 pixels each having a dimension of 8 μm. Note, a SLM may vary in pixel dimensions.

Figure 5.2: When an electric field is applied to the electrodes, the molecules tend to tilt in the direction of the electric field resulting in a phase shift from 0 and 2π. In the case for a zero phase shift there is no applied electric field (a). The liquid crystal molecules are aligned parallel to the electrodes; however, when a voltage is applied across the electrodes, the LC will align itself in the direction of the electric field (b).

When an electric field is applied to the electrodes, the molecules tend to tilt in the direction of the electric field. This brings about a change in the refractive index seen by the light which in turn causes a change in the phase. The phase is represented a by grey-level pattern that is programmed onto the liquid crystal. In order to realise the changes in phase with respect to an applied electric field, two cases are considered which illustrate a 0 and 2π phase shift. In the case for a zero phase shift there is no applied electric field as observed in Figure 5.2(a). The liquid crystal molecules are aligned parallel to the electrodes; however, when a voltage is applied across the electrodes, the molecules will align itself in the direction of the electric field as indicated in Figure 5.2(b).

The phase shift δ is given by:

$$\delta = \frac{2\pi}{\lambda}(n_e - n_o)D, \tag{5.1}$$

where D is the path length of the light as it travels through the birefringent medium, $n_e - n_o$ is the change in refractive index seen by the light and λ is the wavelength. Since the applied voltage is proportional to the refractive index seen by the light, it is clear that for a zero applied field the phase shift is zero and noticeably the phase shift is also wavelength dependent. If an electric field is applied to the electrodes, the liquid crystal molecules will tend to rotate in the direction of the electric field. This brings about a change in the refractive index as seen by the light and hence a change in the phase shift. Programming the SLM with a grey-scale phase pattern results in an appropriate phase shift dependent on the encoding and leads to the generation of states carrying OAM.

5.1.1 Implementation of OAM States in the Form of Laguerre-Gaussian Modes

A LG mode [105] in polar coordinates is given by:

$$E_p^\ell(r,\phi,z) = \left(\frac{\sqrt{2}r}{w(z)}\right)^{|\ell|} \exp\left[-\left(\frac{r}{w(z)}\right)^2\right] L_p^\ell\left(\frac{2r^2}{w^2(z)}\right) \exp\left(ik\frac{r^2}{2R(z)}\right) \tag{5.2}$$

$$\times \exp(i\ell\phi) \exp\left(-(2p+|\ell|+1)\,\zeta(z)\right),$$

where $w(z)$ is the beam width, L_p^ℓ is the generalised Laguerre polynomial, ℓ and p and are the azimuthal index and the radial order respectively, $R(z)$ is the radius of curvature, $\zeta(z)$ is the Gouy phase shift and ϕ is the azimuthul phase. The term that contains the azimuthal phase, $\exp(i\ell\phi)$, is identified with the amount of OAM carried by the beam. It has a $2\pi\ell$ quantised azimuthal phase and leads to an OAM of $\ell\hbar$ per photon [106]. This is a general form of a Laguerre field and can be simplified to a Gaussian beam by setting the values of the azimuthal index and the radial order to zero. By considering the generalised case whereby the azimuthal index, ℓ, is non zero while still keeping the radial order fixed at zero, different orders of LG beams carrying integer amounts of OAM can be generated. This can be realised by varying the order of the azimuthal index.

To further understand this concept, consider the wavefront of a beam carrying an azimuthal index of one. Instead of being planar, the wavefront is helical in shape and the phase of the wavefront will vary from 0 to 2π once. This is illustrated in Figure 5.3 which shows the dependence of the order of the azimuthal index on the helical wavefront. An increase in the azimuthal index leads to an increase in the helical structure or variation in phase from 0 to 2π.

The theoretical and experimental generation of these LG beams, using a grey-scale hologram programmed onto a phase-only SLM, is illustrated in Figure 5.4. The grey-scale digitial hologram is programmed such that the white region represents a zero phase hence at this point the phase of the beam will remain unchanged while the black region represents a phase of 2π. Generating LG beams of various orders entails programming the grey-scale hologram with a variation of white to black regions dependent on the azimuthal index required. By setting the azimuthal index to zero, the grey-scale hologram is programmed to contain a uniform phase as seen in Figure 5.4(a) which leads to the generation of a Gaussian beam represented theoreticallly in Figure 5.4(e) and experimentally in Figure5.4(i). Introducing a helical phase of 0 to 2π leads to a grey-scale hologram pro-

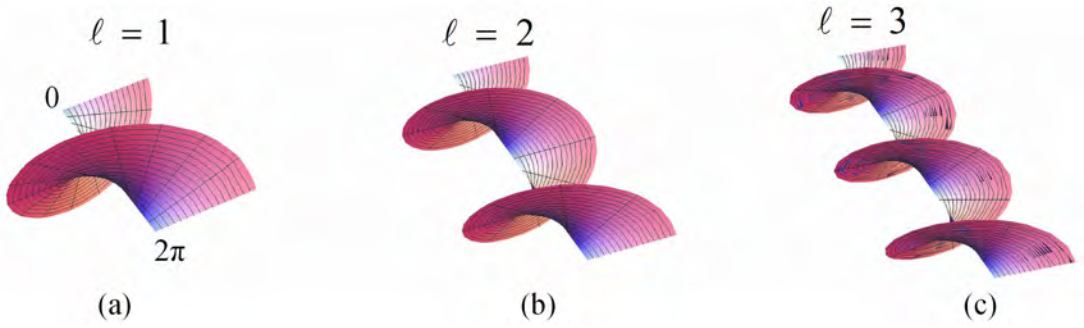

Figure 5.3: Helical wave-front of various order LG beam. The higher the order of the azimuthal index leads to an increase in the number of spirals of the beam and an increase in the region of zero intensity. A azimuthal index of order 1 leads to a phase shift from 0 to 2π once (a). A azimuthal index of two leads to a rotation from 0 to 2π twice (b). Similarly for a azimuthal index of three (c).

grammed with a variation in grey level going from white to black once as seen in Figure 5.4(b) and the generation of a LG beam with central null intensity illustrated theoretically in Figure 5.4(f) and experimentally in Figure 5.4(j). Similarly, this was carried out for higher order LG beams with azimuthal indices of order 2 (Figure 5.4(c), (g) and (k)) and 3 (Figure 5.4(d), (h) and (l)). Theoretically, these beams span an infinite state space which is of relevance to quantum communication since the encoding is not limited to only two orthogonal quantum states.

5.1.2 Implementation of OAM States in the Form of Bessel-Gaussian Modes

Since Durnin's seminal work in 1987 [107, 108], Bessel beams have been studied due to two interesting properties namely their non-diffracting behaviour and their ability to self-reconstruct upon encountering an obstruction [102, 109, 110]. These beams are defined in term of the radial wave vector (k_r) and azimuthal index (ℓ), which gives rise to the helical wave front structure. As a result Bessel beams have the ability to carry OAM, even at the single photon level [111, 112, 113].

Theoretically, a Bessel beam requires an infinite amount of energy however experimentally this beam is estimated to a finite region by Bessel Gaussian (BG) beams [114]. Over the years BG beams have been generated using annular ring-slits in the far field [107, 115], using a conical lens known as an axicon in the near field [116, 92], as well as through the use of digital holography [117, 118, 119, 120, 121].

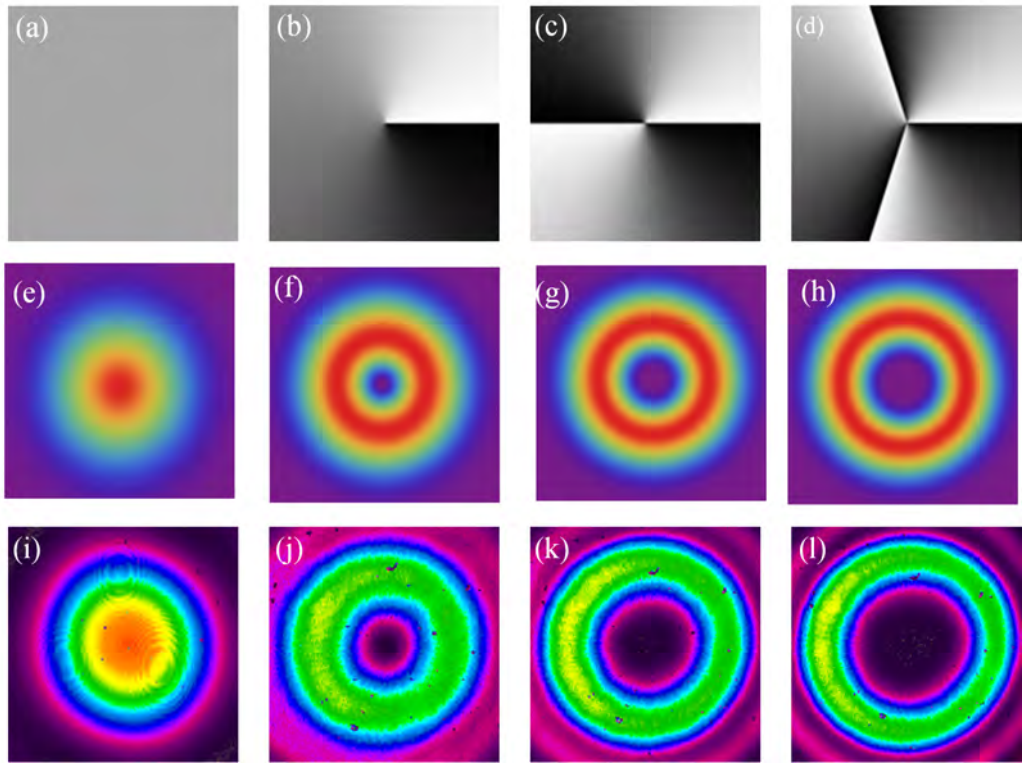

Figure 5.4: Azimuthal phase variations were encoded as digital holograms to convert an incoming Gaussian beam into higher-order LG beams. (a) – (d): digital holograms with an azimuthal variation corresponding to $\ell = 0$ to 3, (e) – (h) corresponding theoretical LG beams of azimuthal order from $\ell = 0$ to 3 and (i) – (l) is the corresponding experimentally generated LG beams of azimuthal order from $\ell = 0$ to 3.

5.1.3 Theoretical Background of Bessel-Gaussian Modes

The BG modes [114] in polar coordinates, are given by:

$$E_{\ell}^{BG}(r,\phi,z) = \sqrt{\frac{2}{\pi}} J_{\ell}\left(\frac{z_R k_r r}{z - iz}\right) \exp(i\ell\phi - ikz) \exp\left(\frac{ik_r z w_0^2 - 2k_r^2}{4(z_R - iz)}\right), \tag{5.3}$$

where ℓ is the azimuthal index, $J_{\ell}()$ is the Bessel function of order ℓ; k_r and k_z are the radial and longitudinal wave numbers respectively. The initial radius of the Gaussian profile is w_0 and the Rayleigh range is $z_R = \pi w_0^2/\lambda$. The propagation constant k and the parameters k_r and k_z are related by $k^2 = k_r^2 + k_z^2$. Although BG modes hold the property of being non-diffracting, when generated in the laboratory they are constrained to a finite propagation distance, given by:

$$z_{\max} = \frac{w_0}{k_r/k} = \frac{2\pi w_0}{\lambda k_r}. \tag{5.4}$$

Bessel beams also have the ability to reconstruct both in amplitude and phase after encountering an obstruction [122, 123]. In this case of reconstruction, there exist a minimum distance behind an obstacle of radius R_{obs} before reconstruction occurs. This distance is identified as the shadow region which is given by:

$$z_{\min} = \frac{2\pi R_{\text{obs}}}{\lambda k_r}. \tag{5.5}$$

The field of Bessel beams can be described as a function of two indices namely the discrete parameter, ℓ, and the continuous parameter k_r. Of which, ℓ determines the helicity of the wavefronts which is related to the amount of OAM carried by the field and k_r dictates the spacing of the intensity rings observed in Bessel beams as illustrated in Figure 5.5 where the order of the beam (helicity) is depicted by the central null intensity.

5.1.4 The Concept of State Generation

The original method for producing these beams introduced by Durnin and colleagues was to use a circular slit to produce an annular ring that was illuminated onto a lens [108]. Over the years however other methods were demonstrated both internal and external to the laser cavity which include the use of anistropic crystals [124], holography [117, 125] and using a conical optical element known as an axicon [92].

An axicon transforms any field into a non-diffracting field. When an axicon is illuminated by some arbitrary field, the light rays will propagate along the cone to form a diamond

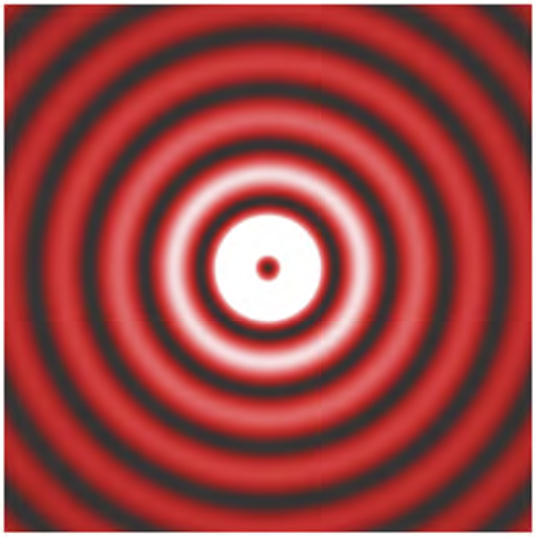

Figure 5.5: First order Bessel beams containing a central null intensity due to the helicity of the beam surrounded by annular rings whereby the spacing of the ring is dependent on radial wave vector, k_r.

shaped region in which the Bessel field exists. Anywhere within this region the Bessel field will be non-diffracting. This method of generating a Bessel field using an axicon can be digitally programmed onto an SLM [48].

An optical set-up was constructed to implement this, consisting of a lens and a digital hologram encoded to represent an axicon which was used to produce and verify the modal content of the field, for all values of ℓ and k_r. The system is shown schematically in Figure 5.6. Illuminating an axicon with a Gaussian beam results in the generation of BG beam at the output. Due to the interchangeability of light the reverse process must convert a BG beam back into a Gaussian beam. This means that essentially there is a possibility to detect particular BG modes, since Gaussian modes may readily be detected by single mode fibres.

Consider a ray-based analysis whereby an incoming Gaussian mode as seen in Figure 5.6 is converted by the first axicon to a BG mode of radial wavevector $k_r = k(n-1)\gamma$, where n is the refractive index of the axicon and γ is the axicon cone angle. The aforementioned transformation results in conical refraction at an angle $\theta = (n-1)\gamma = k_r/k$.

By passing the BG mode through an identical (reversed) axicon, the refracted rays are collimated, or equivalently, the Gaussian mode is generated again. In the case of a mismatch of cone angles, note the cone angle of the second axicon does not match the cone angle of the incoming BG beam, the outgoing rays will not be perfectly corrected hence a pure Gaussian mode will not be formed. This means that the detection is therefore k_r specific and is suggestive of a conventional lens telescope but with conical axicons rather than

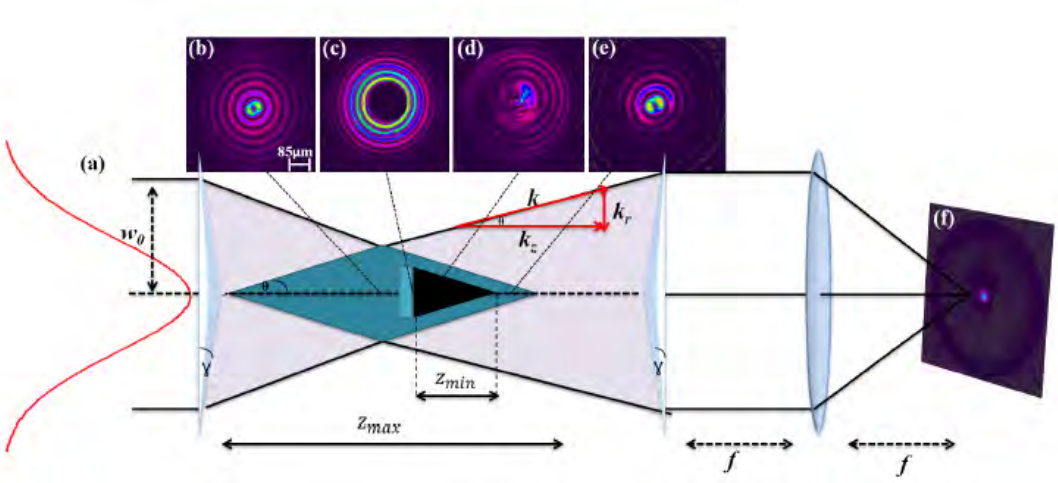

Figure 5.6: A diagram illustrating the generation and the detection of BG beams. (a) The BG beam is generated using a programmed hologram of an axicon, illuminating by a Gaussian beam, and exists in a finite region, $z_{\max}$. An obstacle placed in the center of the BG region obstructed the generated beam for a minimum distance, $z_{\min}$, after which the BG mode reconstructs. (b-e) experimental beam images of a Bessel beam of order $\ell = 1$ at four different positions. (f) The BG beam is detected at the far field of a programmed hologram of a second axicon, where the hologram is placed at $z = z_{\max}$ after the first axicon.

spherical lens. With the addition of a spiral plate with transmission function $\exp(i\ell\phi)$ the detection method becomes specific to the order of the BG mode.

Bessel-Gauss Mode Detection

The aforementioned ray-based analysis becomes tangible by utilising digital holograms for the detection by carrying out a modal decomposition. Modal decomposition is a process of breaking down a beam into its fundamental mode. This is achieved by performing an inner product of the generated beam with an appropriate transfer function. The transfer function, t_{SLM}, for the detection hologram may be written as:

$$t_{\text{SLM}} = \exp(i\tilde{k_r} - i\ell\phi), \tag{5.6}$$

where the first term represents an axicon to detect a BG with a radial wavevector of $\tilde{k_r}$ and the second term specifies the azimuthal index ℓ. Applying this tranfer function to the generated BG mode leads to a process of performing a mode detection. The experimental realisation of this process is illustrated in Figure 5.7 where Figure 5.7(a) is the digital hologram for the detection of a BG mode with $\ell = 3$ and the near and far-field BG mode that it will detect is represented in Figures 5.7(b) and 5.7(c) respectively.

The modal content of the BG mode is determined by carrying out an inner product measurement which is performed optically with the same scheme represented in Figure 5.6.

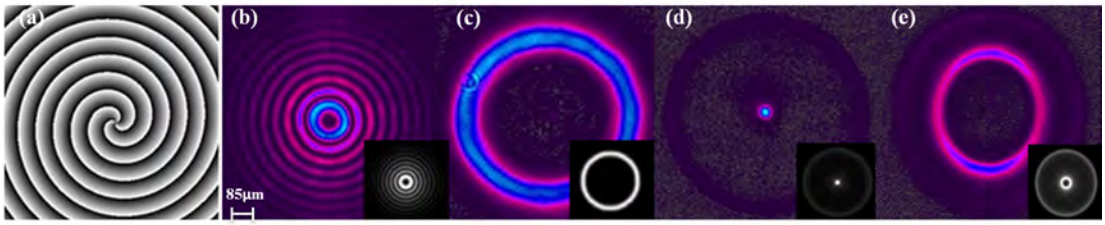

Figure 5.7: Experimental images of (a) a digital hologram for the detector of a BG mode with $\ell = 3$ and (b) a BG mode profile of $\ell = 3$ and (c) its Fourier transform (annular ring). The signal at the detector is shown for the scenarios of (d) matching k_r and ℓ and (e) matching in ℓ but not matching in k_r. The black and white insets show the theoretical results.

By considering the signal at the origin of the focal plane of the lens [126], the field at the output plane can be calculated numerically from

$$g_{\text{out}} = \mathscr{F}\{t_\ell^{BG}\} \otimes \mathscr{F}\{t_{\text{SLM}}\}, \tag{5.7}$$

where $\mathscr{F}$ is the Fourier transform, $\otimes$ denotes the convolution process and $E_\ell^{BG}$is the incoming BG beam defined in Equation (5.3). The angular spectrum of a BG mode and the Fourier transform of the transmission function both have the shape of an annular ring. On the condition that the radii of these annular rings which represent the k_r values of the modes are equal, the convolution of these rings will produce a bright spot with a Gaussian profile (signal) in the center of the output plane, as shown in Figure 5.7(d). This central peak is enclosed by a ring of twice the radius. If there is a mismatch in the radii (k_r values) the central spot will itself become a small ring with a low intensity in the center, which will cause a negligible signal on the detector, as shown in Figure 5.7(e).

This can be quantified by considering the dependence of the width of the annular ring, $\mathscr{F}\{t_\ell^{BG}\}$, upon the radius of the Gaussian envelope of the BG mode. Making an assumption that the ring for the axicon transmission function is exceedingly thin then the width of the ring due to $\mathscr{F}\{t_{\text{SLM}}\}$ is determined by the size of the SLM which is much smaller than the equivalent width for the BG mode. The convolution of the two rings produces a function comprising of two rings with radii that are correspondingly equal to the sum and difference of the radii of the original rings. Thus if the original radii were equal the convolution produces a central spot (signal). Conversely, if these original radii differ the intensity at the center of the output is given by $\exp\left[-\left(\frac{\triangle R}{w_0}\right)^2\right]$, where $\triangle R$ is the difference between the original radii.

For $\triangle R > 1.5 w_0$ the intensity at the center is essentially zero and the corresponding functions are considered to be orthogonal. Likewise, if the ℓ value of the BG mode is different from that of the transmission function of the SLM, they won't be canceled during the con-

volution process. A mismatch in values will result in the central peak in the convolution to have a phase singularity in the center and thus a central intensity null, which will produce a negligible signal on the detector. This means that the BG mode detection method is sensitive to both radial (k_r) and azimuthal indices (ℓ).

5.1.5 Experimental Realisation of Mode Detection

The experimental realisation of the BG mode decomposition comprises of two parts; firstly the generation of a BG beam with known parameters (modal profile) and thereafter the detection of this beam by modal analysis. This was accomplished by constructing the following optical system shown in Figure 5.8, where the created BG beam on SLM_1 is assumed to be the "unknown" beam.

A HeNe laser was expanded with a 3× telescope and directed onto a SLM, denoted as SLM_1, with a beam width of $w_0 = 1\,mm$. The SLM (Holoeye, PLUTO-VIS, 1920×1080 pixels, with a pixel pitch of 8 μm) was calibrated for a 2π phase shift at a wavelength of 633 nm. SLM_1 was programmed with the conical phase of an axicon, plus a helical phase with an azimuthal index ranging from -10 to 10.

The resulting image was filtered through the 4-f imaging system, and propagated a distance of $z_{\max} = 340\,mm$ (for $k_r = 31250\,rad/m$) onto the detection SLM, denoted as SLM_2, where the transmission function was scanned through the spectrum of ℓ and k_r values and the resulting signal detected by a CCD camera placed after a Fourier transforming lens (L_5).

A full modal decomposition was carried out in k_r and ℓ at the plane $z = z_{\max}$ with the results shown in Figure 5.9(a) and 5.9(b). The uncertainty in detection of the order ℓ is clearly negligible while that for the radial wavevector is approximately 5% (one standard deviation). This scheme illustrates that using this method a wide range of Bessel modes can be detected quickly and accurately.

The versatility of this approach was tested by applying it to two perturbation studies: the self-healing of Bessel beams after an obstacle and the propagation of Bessel beams through turbulence. The aformentioned detection method was used to experimentally observe the change in modal spectrum during these processes.

Bessel Reconstruction

A circular opague disk, with a radius of $R_{\text{obs}} = 300\,\mu m$, was used as the obstruction. The disk was initially placed at 34 $z_{\max}$ for a BG of k_r = 0.25 rad/pixel. The detection was done at z = 34 $z_{\max}$ while the disk was moved away from the detection plane until exceeding the

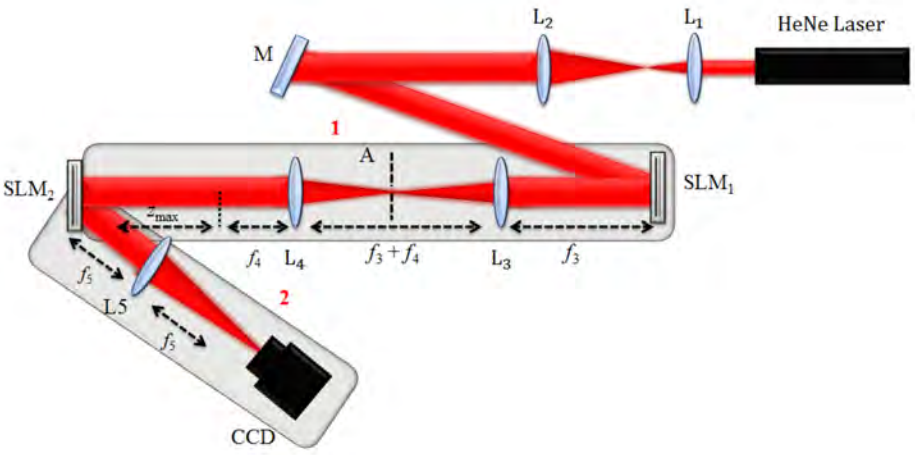

Figure 5.8: A schematic of the experimental setup for accomplishing the decomposition of a Bessel field. The Lenses L_1, L_2, L_3, L_4 and L_5 have focal lengths f_1 = 100 mm, f_2 = 300 mm, f_3 = 500 mm, f_4 =500 mm and f_5=150 mm, respectively. A is the filtering aperture. SLM_1 and SLM_2 denote the two SLMs and M represents a mirror. The field from SLM_1 was relay imaged with a 1:1 telescope and then allowed to propagate a distance of z_{max} prior to modulation by SLM_2. The resulting signal was measured in the far field of SLM_2 using a CCD camera.

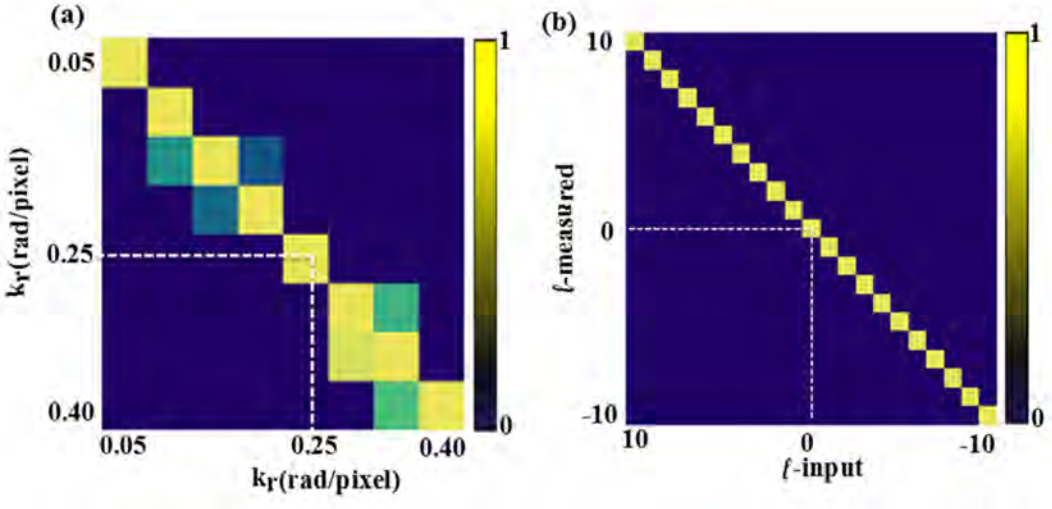

Figure 5.9: A full modal decomposition was done in k_r and ℓ at the plane $z = z_{\max}$. The results depicted is that for a Bessel beam, radial k_r, decomposition for ℓ= 1 (a) and the Bessel beam, azimuthal indices ℓ, decomposition for k_r = 0.25 rad/pixel (b) .

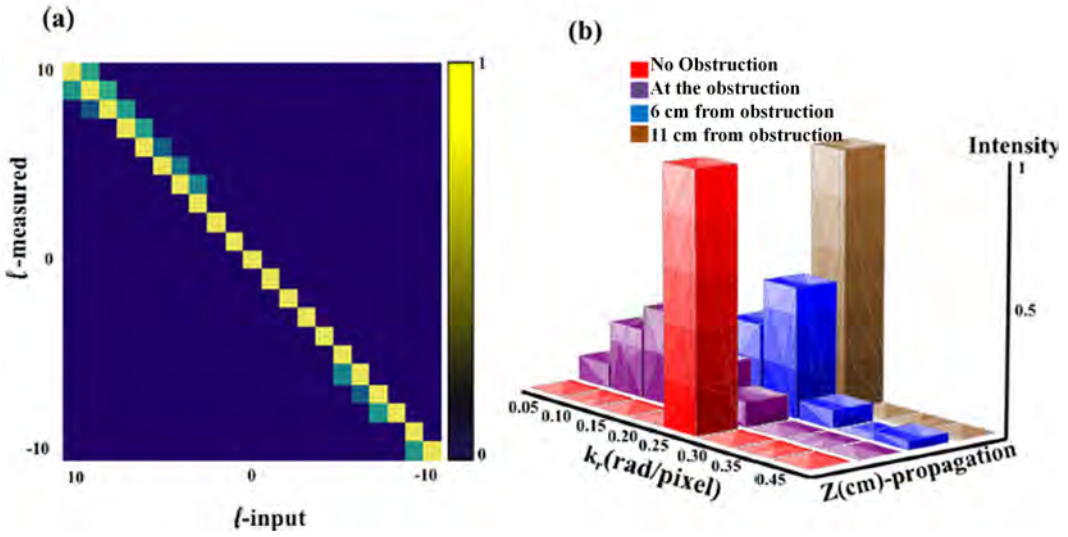

Figure 5.10: A minimal azimuthal distortion of the mode due to the obstruction was observed but significant broadening of the radial modes. Azimuthal decomposition (ℓ detection) of the fully obstructed beam (a) and k_r decomposition without an obstruction and then at three planes with the obstruction (b).

self-healing distance of z_{min} = 9.5 cm. The radial and azimuthal spectrum was measured before the obstruction and then at various distances after the obstruction until the self-healing process was completed. As observed in Figure 5.10 minimal azimuthal distortion of the mode due to the obstruction, but significant broadening of the radial modes. This broadening reduces as the beam self-heals, returning to the initial spectrum after the self-healing distance. While the self-healing of Bessel beams has been studied extensively before [123], this is the first time that the process has been observed using modal analysis.

Bessel Propagation Through Turbulence

This tool is of interest when applied to the study of Bessel beams propagating through turbulence, a topic that has received much theoretical attention of late. The atmospheric turbulence was simulated using a diffractive plate which was extensively discussed in Chapter 4. The plate was encoded for Kolmogorov turbulence, which for the purpose of this study was characterised in terms of the Strehl ratio [127]. The turbulence plate was placed at $\frac{1}{2}z_{\text{max}}$ and the detector at $z = z_{\text{max}}$. Two turbulence strengths were used corresponding to Strehl ratios of SR = 0.2 and SR = 0.03, with the impact on the Bessel modes shown in Figure 5.11.

Without the plate the results are identical to those shown earlier: narrow k_r and ℓ spectrums with little cross-talk, as seen in Figures 5.12(a) and 5.12(b). At medium turbulence levels (SR = 0.2), the k_r spectrum broadens and so does the OAM spectrum [Figures.

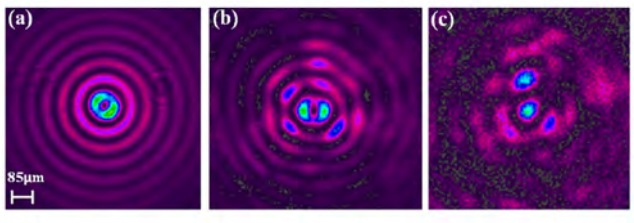

Figure 5.11: Impact that turbulence strengths has on the Bessel mode corresponding to Strehl ratios of SR = 0.2 and SR = 0.03. Images of a BG mode profile for $\ell = 1$ (a) without turbulence, after passing a turbulence of (b) SR=0.2 and (c) SR=0.03.

5.12(a) and 5.12(c)], becoming wider [Figures 5.12(a) and 5.12(d)] as the turbulence becomes very strong (SR = 0.03). These results are consistent with that predicted by theory [128, 129], and serves to illustrate the versatility of the tool. This work thus shows the ability to distinguish both the radial and azimuthal indices of such beams, a core requirement for optical communication protocols if the bit rate per photon is to be increased by exploiting all the degrees of freedom of spatial modes.

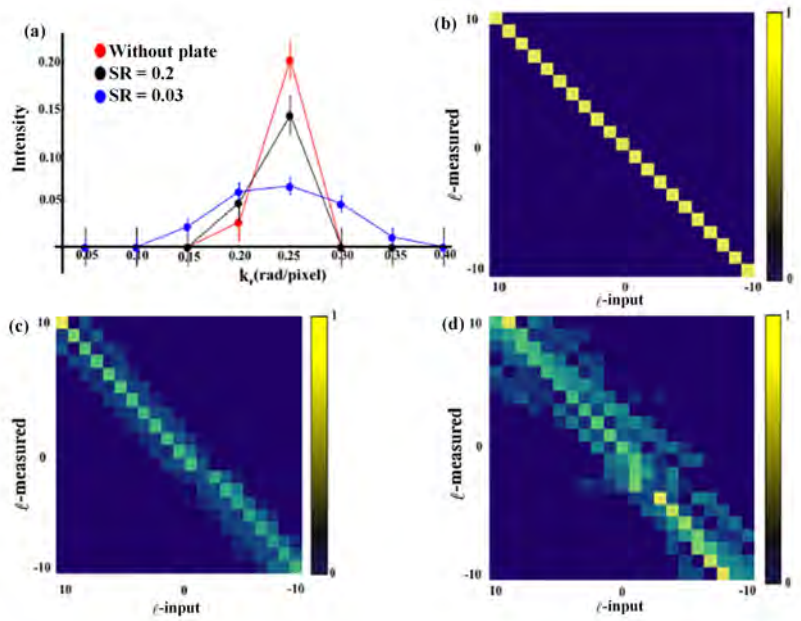

Figure 5.12: (a) Decomposition of k_r = 0.25 rad/pixel for different strehl ratios where the red line is the decompisition in the absence of the plate, the black line is the decomposition for weak turbulence (SR=0.2) and the blue line is the decomposition for strong turbulence (SR=0.03) (b) decomposition spectrum without turbulence. (c) and (d) decomposition spectrum for SR = 0.2 and SR = 0.03, respectively.

6

Construction of a Polarisation Encoded Entanglement Source Using High Powered Lasers

A single photon source provides substantial value to the field of optical quantum information. One of the challenges in quantum communication is to build a robust and widespread communication network. Such a network requires a bright source of high quality entangled photon pairs [130]. For this to be realised, sources of entangled photon pairs need to meet the following three criteria:

Light Source

An appropriate pump laser is one of the most important factors to consider when constructing an entanglement sources. The parameters of the pump laser affects a number of components within the system and more specifically it dictates the downconversion process. The type of non-linear crystal utilised for the downconversion process relies on the wavelength of the pump source. Apart from the logistics of constructing the source, the power output of the pump laser determines the optimum efficiency of the source. The brightness of the source is dependent upon the power output of the pump laser and is related to the rate of photon pair generation. Furthermore, a brigther source leads to a higher quality of entanglement and a larger violation of the Bell inequality.

Beam Quality

A Gaussian beam is propagation invariant which means it retains its spatial distribution as it propagates in free space, however it varies in beam width as a function of the propagation distance as illustrated in Figure 6.1 and is defined as [131]

$$w(z) = w_0 \sqrt{1 + \left(\frac{z}{z_R}\right)^2}, \tag{6.1}$$

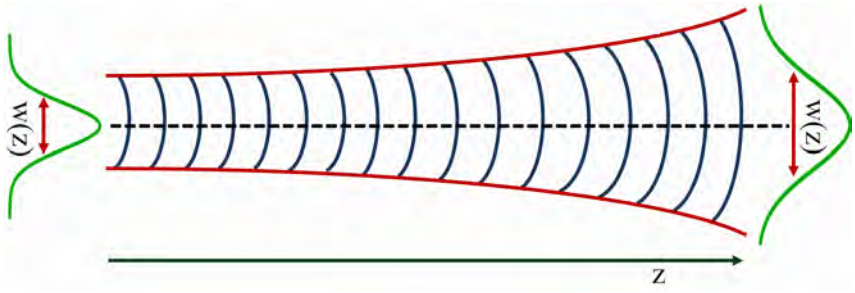

Figure 6.1: Propagation of a Gaussian beam in free space along the optical axis, z., where w(z) is the width of the beam which is a function of distance, z. As the propagation distance increases, the width of the beam increases.

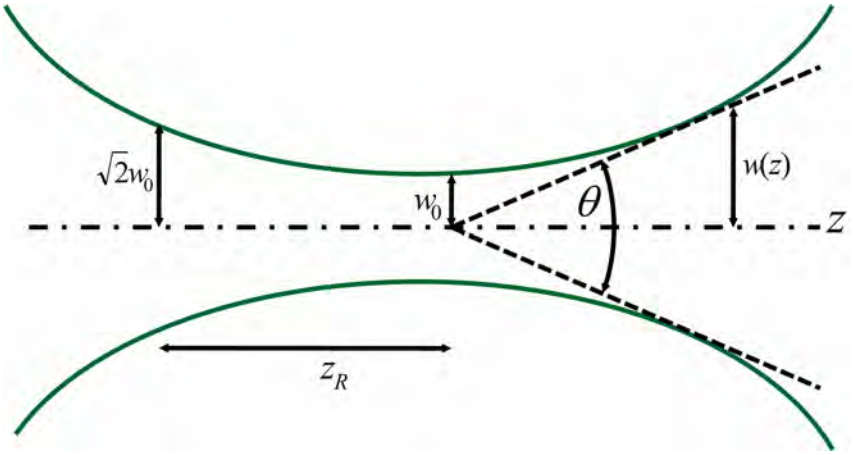

Figure 6.2: Geometrical interpretation of the beam width, $w(z)$, with respect to propagation distance, z, where w_0 is the beam waist, z_R is the Rayleigh range and θ the beam divergence.

where z is the propagation distance, w_0 is the beam waist and z_R is the Rayleigh range. The Rayleigh range is the distance along the direction of propagation from the beam waist to the point at which the cross sectional area of the beam is doubled as seen in Figure 6.2 and is defined as [131]

$$z_R = \frac{\pi w_0^2}{\lambda}, \tag{6.2}$$

where λ is the wavelength. As observed, the Rayleigh range is directly dependent upon the beam waist and inversely proportional to the wavelength. As the propagation distance increases the beam width increases linearly (Equation (6.1)) which is further seen by the dashed line in Figure 6.2. Clearly, w_0 is the point at which the beam width is at its minimum, that is, when $z = 0$.

It is not only the beam width that changes with an increase in propagation distance, there is also a change in wavefront of the Gaussian beam which can be expressed in terms of the radius of curvature given as [131]

$$R(z) = z\sqrt{1+\left(\frac{z_R}{z}\right)^2}. \tag{6.3}$$

Similar to the width of the beam, the radius of curvature is also dependent on the Rayleigh range and the propagation distance. The quality of the beam is determined by beam quality factor, M^2, which is measured by equating the M^2 with the product of the beam waist and the beam divergence defined as [131]

$$w_0\theta = \frac{M^2\lambda}{\pi}, \tag{6.4}$$

where θ is the beam divergence. Experimentally the M^2 value is determined by measuring the width of the beam as it propagates along the optical axis, upon passing through a thin lens, of which it is expected that the field with a Gaussian distribution has a beam quality factor 1. One of the conditions for downconversion is a good quality beam hence the lasers incorporated within an entanglement source should have a beam quality factor close to one.

Non-linear optics is based on the study of the effects of a dielectric medium in the presence of a strong optical field. In this case it is the interactions of a laser beam within a non-linear crystal. If a laser beam is passed through a linear medium it remains in an unaltered state however in the case of a non-linear crystal the laser beam undergoes a frequency conversion. Numerous types of non-linear crystals can be utilised within an entanglement source whereby the choice of crystal is dependent upon the application of the source. With respect to QKD an entanglement source can be built for telecommunications wavelength or for free space transmission. This source discussed within this chapter was built with the intention of free space QKD.

6.1 Optical System Design

In order to improve the design of an entanglement source, all the processes leading to the construction of the system need to be addressed individually. A schematic of these processes is illustrated in Figure 6.3 and will be discussed in detail within this chapter. The work presented in this chapter is currently in the process of being prepared for publication.

6.1.1 Pump Source

Continuous Wavelength (CW) lasers are feasible choices for entanglement sources due to their compactness and versatility. They suffer however from decoherence resulting in a compromise between source brightness and fidelity. This can be overcome by using

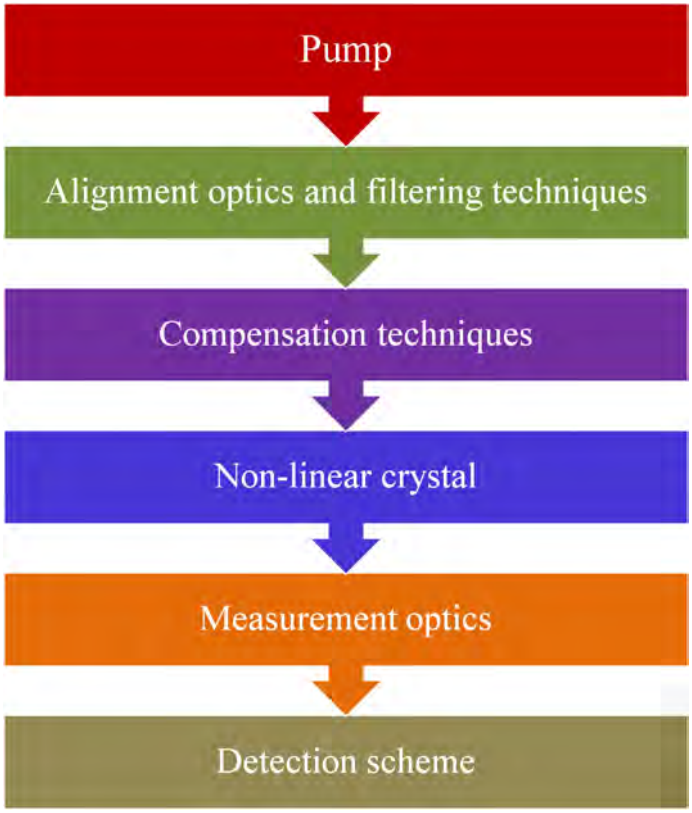

Figure 6.3: Schematic outlining the processes involved in constructing a polarisation based entanglement source in systematic order starting from the pump source ending with the detection scheme. The most important process is the generation of the polarisation entangled photons created by a non-linear crystal.

an appropriate spatial-phase compensation techniques which will be discussed further in Section 6.1.3. The important parameters when choosing an appropriate pump for an entanglement source is listed below:

- Power output
- Divergence
- Beam width

The power output contributes to the brightness of the source and hence infers the detection of photon pairs. Here, a 400 mW power output is used to pump a Beta Barium Borate (BBO) non-linear crystal. This was obtained by making use of three diode lasers, of which two were lasing at 135 mW and the third at 120 mW, combined using a curved mirror. The reason for using three lasers instead of one high powered laser, was that all of the aforementioned lasers, were reasonably priced hence they were an economical choice for the system. This particular system was built with the intention of maniturising the system to a portable entanglement source. The use of these three lasers allowed for the design of the source to be as compact as possible. The chosen power output is also under that of the damage threshold for the non-linear crystal used for the downconversion process. Apart from the power the parameters of the lasers were determined. The width of the combined beam was measured to be 3 mm and the divergence was 0.0859 mrad. For downconversion the spot size is quite large however with the necessary optics this was reduced before entering the BBO crystal.

6.1.2 Alignment Optics and Filtering Techniques

One of the crucial processes within the developement of an entanglement source is the alignment. Misalignment of the source can result in the degradation of entanglement. Here, planar mirrors were used to align the near and far-field of the three lasers prior to beam combination. The laser beam combination process was implemented by making use of a concave curved mirror as illusrated in Figure 6.4. This technique resulted in beam combination without major loss of power as would be the case if a beam splitter or fibre combiner was ulitised instead. Utilising a beam-splitter would mean accepting at best 10 % trade-off in power. A curved concave mirror has a reflecting surface that bulges inward which collects light incident to the surface by refocusing the incoming parallel rays towards a focus. This is due to light being reflected at different angles since the normal to the surface is different at various positions on the mirror.

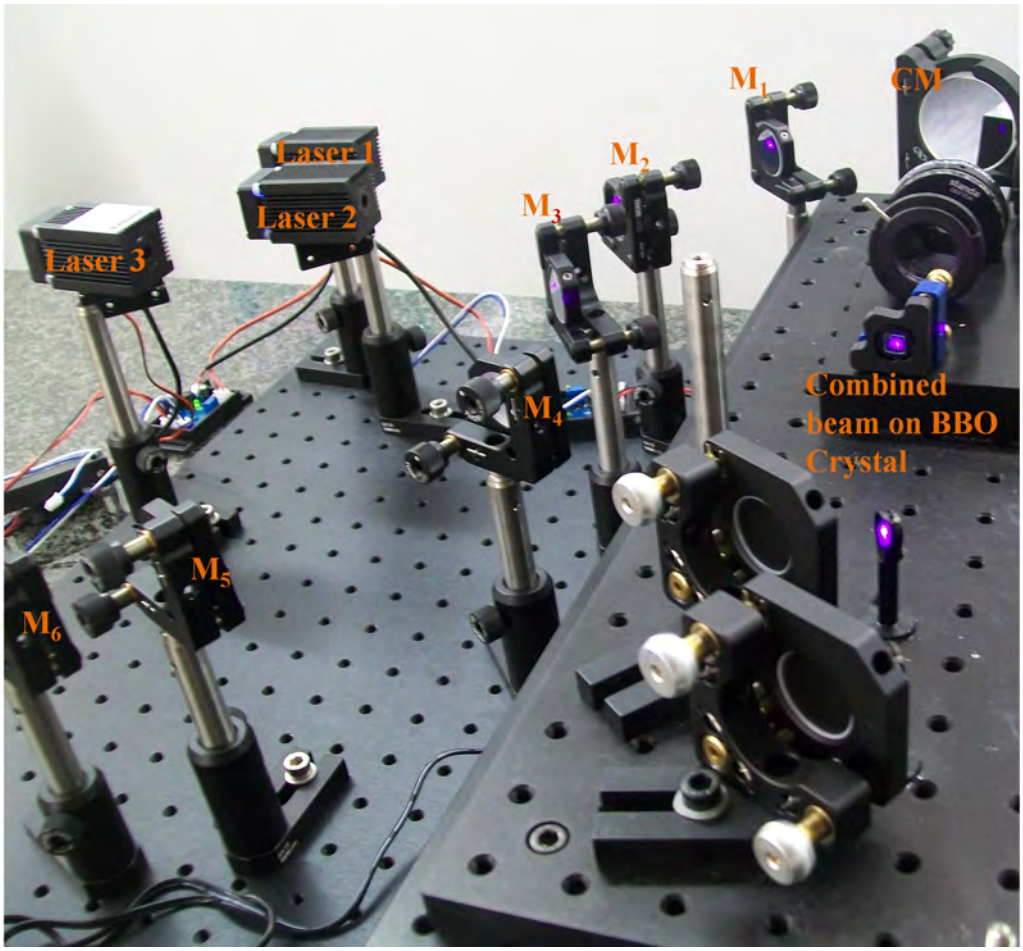

Figure 6.4: Experimental setup of laser combination system using a curved mirror. Three lasers were combined during this process, each having a power output of 150 mW. Mirrors (M_1-M_6) were used to direct the beam towards the curved mirror (CM). The combined beams is viewed on the BBO Crystal. This is the size of the beam before filtering.

It is important to pump the non-linear crystal with a Gaussian beam that has a good beam quality. Usually the beam shape of laser diodes is elliptical. For optimal performance of the system a correction of the ellipticity of the beam is required. This is achieved by the carrying out the necessary filtering techniques. In this case, the Gaussian beam was passed through a cylindrical lens which was used to convert the beam to focus to a rotational symmetric waist on the non-linear crystal.

To generate the appropriate state as represented in Equation (2.8), the incoming polarisation of the pump beam has to be diagonally polarised. This allows for an equal probability of either the horizontal or vertical state being generated within the non-linear crystal. This was easily achieved by placing a HWP infront of the non-linear crystal.

6.1.3 Compensation Techniques

As mentioned in Secion 6.1.1 the use of CW lasers leads to decoherence of the source.

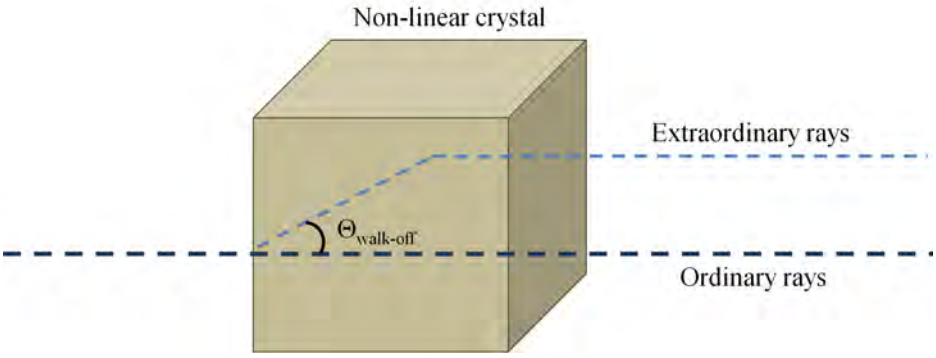

Figure 6.5: Diagram illustrating the walk-off experienced by the extraordinary waves due to the birefringence of the non-linear crystal where $\theta_{walk-off}$ the is the walk-off angle. The walk-off of the light rays leads to the loss of entanglement which can be compensated for using an additional crystal that is half the thickness of the downconversion crystal.

Decoherence is also caused by the angle dependent phase shift of the non-linear crystal as well as by the use of large irises. Large aperture also leads to the degradation in the quality of entanglement. These effects can be compensated for using spatial and spectral compenstaion method first demonstrated by Kwait et al [132, 62]. Due to birefringence of the non-linear crystal, the refractive index of the extraordinary wave will experience a Poynting vector walk-off . The walk-off produces a shift between the ordinary and extraordinary rays as shown in Figure 6.5.

If the beam width of the input beam is separated at the walk-off angle in the crystal it will cause a low conversion efficiency. This walk-off angle is given by [132]

$$\theta_{\text{walk-off}} = \left(\theta_p - a\tan\left[\frac{n_o^2}{n_e^2} \tan\theta_p \right] \right) sgn\left(n_o - n_e\right), \tag{6.5}$$

where θ_p is the angle from the optical axis, n_o is the crystals ordinary index and n_e is the crystals extraordinary index. The amount of the walk-off depends on the location where the photon-pairs are created within the crystal. This position is completely random due to the coherent nature of the downconversion. This effect leads to a loss of entanglement which can be mitigated by using an additional crystal that is half the thickness of the downconversion crystal and oriented in the same way as the original downconversion crystal [132]. Here a BBO crystal, 245 μm in thickness and cut at 33.9^0 , was used to compensate for spatial decoherence. The spectral-temporal decoherence was countered by precompensating with a birefringent quartz crystal that was placed before the down-conversion crystal. Apart from this, a pair of narrow bandpass filter centred at 810 nm with a bandwith of 10 nm was used to clean the spectrum and increase the entanglement

visibility [62].

6.1.4 Non-Linear Crystal

To obtain entanglement the phase matching condition needs to be satisfied irrespective if a type-I or II crystal is utilised for the downconversion. This is automatically adhered to by cutting the crystal specific for a specific wavelength. If however, the wavelength of the pump beam is only close to the wavelength for which it is cut, the phase matching condition needs to be re-established by tilting the crystal. The tilt of the crystal is determined by first ascertaining the extraordinary and ordinary refractive indices of the crystal computed by the Sellmeier equations represented as [133]

$$n_e = 2.3753 + \frac{0.01224}{(\lambda^2 - 0.01667)} - 0.01516\lambda^2 \tag{6.6}$$

$$n_o = 2.7359 + \frac{0.01878}{(\lambda^2 - 0.01822)} - 0.01354\lambda^2, \tag{6.7}$$

where n_e and n_o are the extraordinary and ordinary refractive index respectively and λ is the wavelength in μm. The tilt of the crystal is thereafter determined by:

$$\theta_{\text{tilt}} = \sin^{-1}(n^0(\text{pump wavelength}) \sin \theta_{\text{diff}}), \tag{6.8}$$

where θ_{diff} is the difference in orientation of the pump laser and the cut of the crystal determined by $\theta_{\text{diff}} = \theta_{\text{pump wavelength}} - \theta_{\text{crystal wavelength}}$.

There are a number of non-linear crystals that can be utilised for the downconversion process. The choice of crystal is dependent on the properties of the crystal and the wavelength of the pump beam. A good criteria for choosing an appropriate non-linear crystal is listed below:

- Phase matching type and angle cut
- Damage threshold
- Acceptance angle
- Spectral acceptance
- Crystal size and walk off angle
- Temperature acceptance and moisture

Table 6.1: Properties of a type-I concactenated BBO Crystal used for the implementation of a single photon source generating polarisation encoded photons.

Pump angle	29.3°
Dimensions	$7 \times 7 \times 0.7\,\mathrm{mm}^3$
Absorbtion coefficient	$< 0.1/\mathrm{cm}^2$ @ 1064 nm
Transparency range	$189 - 3500\,\mathrm{nm}$
Damage threshold	$1\mathrm{GW}/\mathrm{cm}^2(10\,\mathrm{ns})$ @ 532 nm

For the purpose of this experiment a type-I concatenated BBO crystal that was cut for a pump laser lasing at 405 nm was utilised for the downconversion. This meant that there was no need for any tilt of the crystal. The advantage of using a type-I crystal is the comparitively high brightness of the source, the increase in stability and the ease of alignment. The properties of the crystal used for this study is summarised in Table 6.1.

The length of the crystal is of important as it relates directly to the conversion efficiency of the crystal. Selecting the optimum height of the crystal becomes significant as this dimension should be slightly larger than the diameter of the laser beam entering the crystal. The crystal thickness is also important as it influences the photon generation. A thinner non-linear crytal can generate a higher number of entangled photons [134]. Here the BBO crystal used for the downconversion has a thickness of 0.7 mm. The pump angle of the crystal is dependent on the wavelength as well as other factors such as the refractive indices of the crystal. Taking these parameters into consideration the pump angle for the downconversion crystal was cut for 29.3°.

6.1.5 Measurement Optics and Detection Scheme

Since a polarisation encoded system is being developed, the measurement scheme required the use of polarisers. A polariser is an optical filter that passes light of a specific polarisation and blocks waves of other polarisations. It can convert a beam of light of undefined or mixed polarisation into a beam with well-defined polarisation. The detection scheme consisted of fibre couplers, a pair of avalanche single photon detectors and a means to determine the coincidence (coincidence counter). The fibre couplers were used to shift from free space to fibre.

Avalanche single photon detectors are solid-state photo detector which can trigger an avalanche current caused by the arrival of photons. This device is able to detect low intensity signals specifically down to the single photon regime. The intensity of the signal is obtained by counting the number of photons in the output pulses within an integration time. An ideal detector should hold the following properties [135]:

Table 6.2: List of specification for the avalanche single photon detectors used to measure the single count rates in the the channels.

Spectral Range	450-1050 nm
Peak detection efficiency at 800 nm	30 % (40 %)
Dark count rates per channel	1500(typically 500) cps
Dead time	approximately 1μs
Output pulse width	40 ns

- A higher detector efficiency than the needed spectral range. The detector efficiency is defined as the probability that a single photon incident on the device is detected,
- A low dark count rate. Note the dark count rate is the rate at which the detector generates signals without an arriving photon.
- A constant time between the arrival of the photon and the generation of the corresponding signal.
- A short dead time which is the time between detections during which no events are recorded.

The specifications of the detector used for the implementation of the source are listed in Table 6.2.

6.2 Alignment of an Entangled Source

Before continuing with the alignment process, recall that the system being built is a free space system however since the detectors are embedded within the coincidence count, fibre couplers using single mode fibres are used to transfers single photons to the detectors. This means that the system is a free space and fibre based system. The alignment process can be broken into two parts, namely, the aligment of the BBO crystal and HWP and thereafter the alignment of the detectors

Aligning the BBO Crystal and HWP

1. Prior to aligning the BBO crystal, the beam was aligned such that it was collimated and traveling along one of the holes on the bread board. This made the alignment process simpler.
2. When adding the BBO crystal to the system a good vertical height was chosen. The height was adjusted such that the pump beam hit the central region of the crystal.

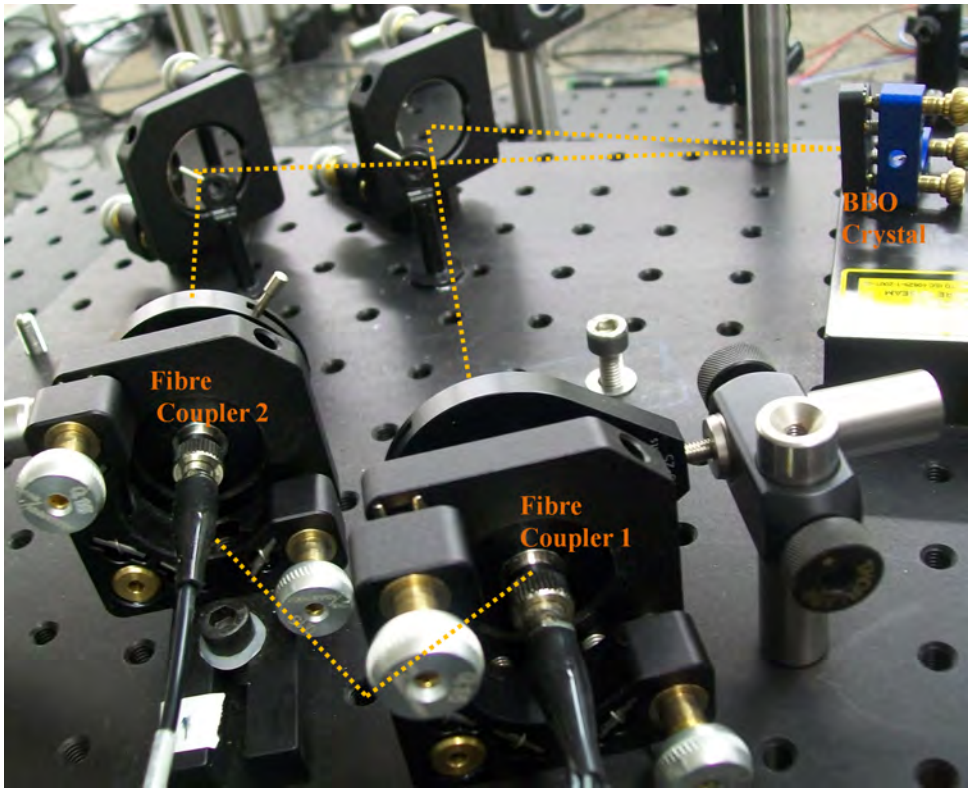

Figure 6.6: Image of BBO and fibre coupler alignment. The fibre couplers were placed 12 holes which is 300 mm away from the BBO crytal to allow for sufficient sepearation of the generated photon pair. The fibre coupler were placed about 25 mm outwards from the position where the pump beam should propagate.

To ensure that this was done correctly the pump beam (blue spot) was observed on the other side of the crystal.

3. The HWP was then be placed in the path of the beam before the BBO crystal and set at 22.5 degrees. It was positioned such that there was room to read and adjust the orientation of the plate.

Aligning the Detectors

For Detector A:

1. To avoid overlap of the single photon pairs generated, the detectors, in this case the fibre couplers, were placed as a rule of thumb on the breadboard about 12 holes, approximately 300 mm, away from the BBO crystal. Furthermore the fibre couplers were placed about 1 holes outwards (25 mm) as observed in Figure 6.6.

2. The height of the fibre coupler was adjusted by placing a preset iris in front of the fibre coupler. The height of the fibre coupler was adjusted close enough to the height of the iris.

3. To align the fibre coupler with respect to the BBO crystal, the fibre coupler was connected to a HeNe laser and the tilt of the fibre coupler was adjusted until the HeNe laser reached the centre of the BBO crystal.

4. A 10 nm bandpass filter centred at 810 nm was placed directly in front of the fibre coupler lens and aligned so that the face was roughly perpendicular to the down-converted beam.

5. Thereafter the fibre exiting the fibre coupler was connected to the detectors sitting within the coincidence counter. The counts rates was detected by setting the integration time to 1s and observing the single count in channel 1 rise above that of the dark counts.

6. The horizontal/vertical tilt adjustment knobs of the fibre coupler was adjusted until a maximum single count rate was reached. The point of maximum single count rate was validated by adjusting the horizontal/vertical tilt in increments and observing the fluctuations in the single counts. Using this method the fibre coupler was adjusted to a position of maximum single counts.

For detector B, steps 1-6, were repeated as carried out for the alignment of detector A however instead of maximising the single count rate of detector B, the coincidence counts was maximised. The aforementioned steps were repeated a few times for both detectors to ensure that the system was correctly aligned. Collating the aforementioned techniques the system is represented in Figure 6.7. The single counts rates reached 1.515×10^6 cps in channel 0 and 1.425×10^6 in channel 1.

6.3 Characterisation of the Bright source

The characterisation of the bright source was carried out similar to the analysis performed in Chapter 3. The quality of entanglement was determined for both bases, the rectilinear and diagonal bases. The coincidence was measured at each orientation over an integration time of 1s. The dark count of the detectors were measured to be 900 and 1600 cps in detector A and B respectively. The resolution time was set at 26 ns. A plot of the data for the two bases is shown in Figure 6.8.

The resulting visibility was measured to be 99.0 % ± 0.14 % and 99.2 % ± 0.13 % for the rectilinear and diagonal basis respectively which was calculated using Equation (2.12). The coincidence counts of both bases (rectilinear and diagonal) have a cosine squared dependence and are correlated. From Figure 6.8 it can also be seen that the mean number

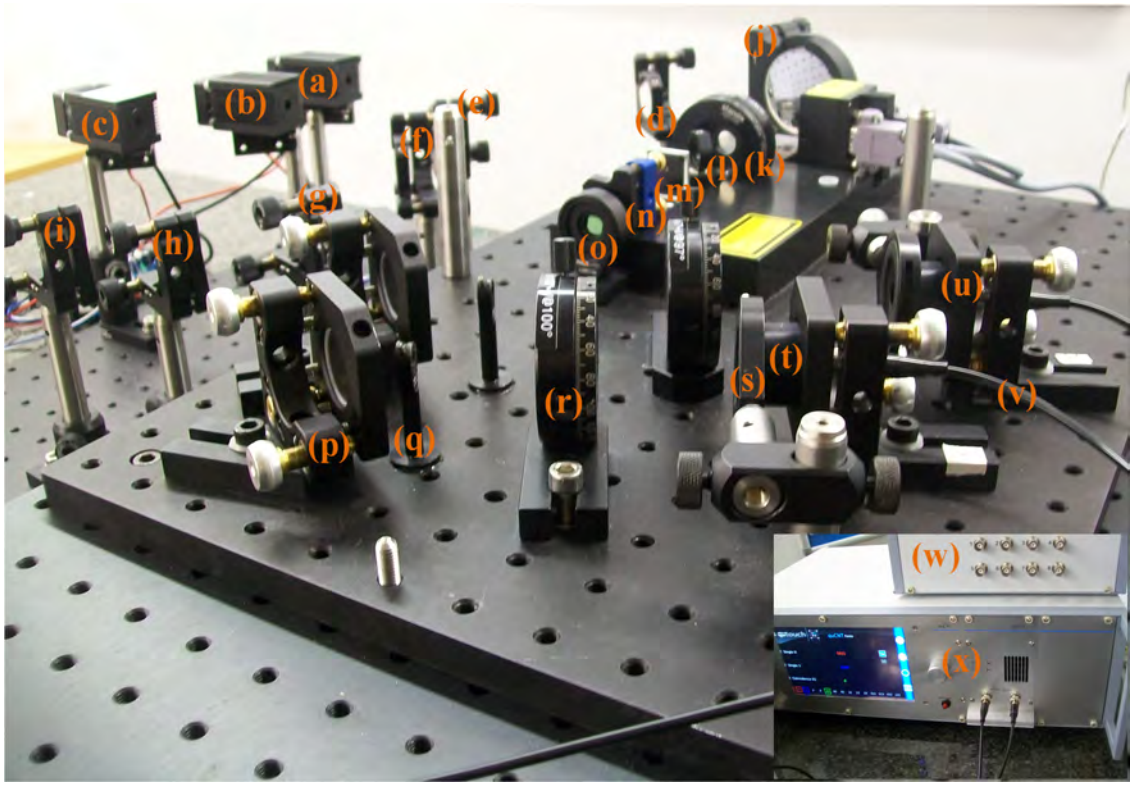

Figure 6.7: Optical system constructed to generate and characterise polarisation encoded single photon pairs using high powered lasers: (a)-(c) UV pump lasers lasing at 405 nm with a power output of 150 mW, (d)-(i) planar mirrors used to align the near and far-field, (j) concave curved mirror, (k) Half Wave Plate (HWP). (l) quartz crystal compensator, (m) cylindrical lens, (n) concatenated type-I BBO crystal, (o) crystal compensator, (p) mirrors, (q) variable apertures (r) polarisers, (s) variable apertures, (t) long pass filters, (u) fibre couplers, (v) single mode fibre, (w) time to digital convertor, (x) coincidence counter embedded with single photon avalanche detectors.

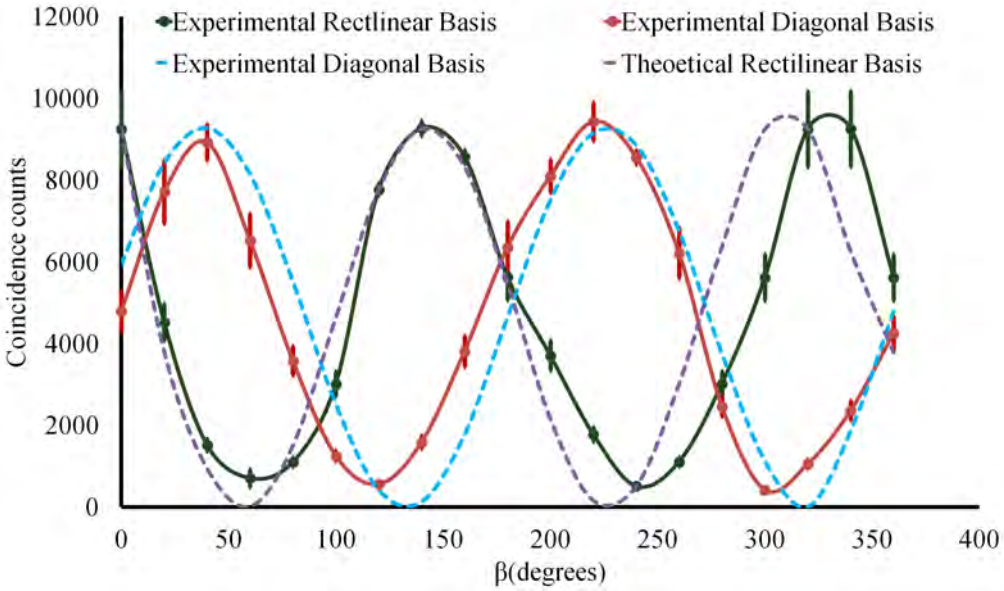

Figure 6.8: Plot representing the correlation of the rectilinear and diagonal bases. The rectilinear basis was measured by setting polariser 1 to 0° while varying the orienation of polariser 2. The orientaion was varied from 0° to 360° and coincidence was measured at each variation. Similarly this was carried out for the diagonal basis except in this case polariser 1 was set at 45°.

of coincidences per second was about 4500 with a noise of about 100 coincidences per second. The coincidences was minimum when the measurement basis were at horizontal and vertical respectively while it was maximum when they were at the same basis.

Presetting the orientation of the polarisers in each arm of the source as carried out in Chapter 3, the system was tested for the violation of the CHSH inequality. The data obtained during the various experimental runs are presented in Table 6.3 from which the violation was determined to be 2.79 ± 0.01. For the theoretical violation of the CHSH inequality, it is expected that the S-value tends to $2\sqrt{2}$, we obtained a value 0.8 % less than the expected value. This data was obtained for an integration of 3s as opposed to the usual integration time of 5s. At lower integration time, the coincidence counts tends to fluctuate, which results in a higher accidental count which lowers the S-value obtained. With the high powered scheme presented, the fluctuation in coincidence was minimised even at a low integration time.

Although the violation of the CHSH inequality verified entanglement, as a last step in the characterising of a polarisation based entangled source the fidelity of the system was measured. This was achieved by setting the HWP and QWP to the appropriate orientation as listed in Table 6.4 and measuring the coincidence at each permutation. From the data presented in Table 6.4 the desity matrix shown below was reconstructed by making use of the maximum likelihood method [73] represented in Equation (2.27)

Table 6.3: Data obtained during the 16 permutation used to determine the violation of CHSH inequality. This was achieved by varying the orientation of the polarisers according to the predetermined angles and measuring coincidence. From the coincidence the expectation value for each orientation set was determined. This was used to measure the violation.

Expectation value when α is 0 and β is 22.5 degrees								
α	β	$\alpha_\perp$	$\beta_\perp$	$C(\alpha,\beta)$	$C(\alpha_\perp,\beta)$	$C(\alpha,\beta_\perp)$	$C(\alpha_\perp,\beta_\perp)$	$E(\alpha,\beta)$
0	22.5	90	112.5	8358	1409	1629	8196	0.689873
Expectation value when α' is 45 and β is 22.5 degrees								
α'	β	$\alpha'_\perp$	$\beta_\perp$	$C(\alpha',\beta)$	$C(\alpha'_\perp,\beta)$	$C(\alpha',\beta_\perp)$	$C(\alpha'_\perp,\beta_\perp)$	$E(\alpha',\beta)$
45	22.5	135	112.5	8402	1455	1674	8447	0.686755
Expectation value when α is 0 and β' is 67.5 degrees								
α	β'	$\alpha_\perp$	$\beta'_\perp$	$C(\alpha,\beta')$	$C(\alpha_\perp,\beta')$	$C(\alpha,\beta'_\perp)$	$C(\alpha_\perp,\beta'_\perp)$	$E(\alpha,\beta')$
0	67.5	90	157.5	1685	7542	7734	1125	-0.68926
Expectation value when α' is 45 and β' is 67.5 degrees								
α'	β'	$\alpha'_\perp$	$\beta'_\perp$	$C(\alpha',\beta')$	$C(\alpha'_\perp,\beta')$	$C(\alpha',\beta'_\perp)$	$C(\alpha'_\perp,\beta'_\perp)$	$E(\alpha',\beta')$
45	67.5	135	157.5	9059	1584	1007	7193	0.724991

$$\rho = \begin{bmatrix} 0.4889 & -0.0025+0.0230\,i & -0.0710-0.0788\,i & 0.6007+0.0491\,i \\ -0.0025-0.0230\,i & 0.0176 & 0.0567-0.0820\,i & -0.0842-0.0378\,i \\ -0.0710+0.0788\,i & 0.0567+0.0820\,i & 0.0125 & -0.0786+0.0471\,i \\ 0.6007-0.0491\,i & -0.0842+0.0378\,i & -0.0786-0.0471\,i & 0.4801 \end{bmatrix}.$$

A graphical representation of the real and imaginary part of the density matrix is illustrated in Figure 6.9. The fidelity of the system was determined to be 0.997 ± 0.0001, evaluated using Equation (2.26,) by taking the trace of the density matrix. Noticeably the fidelity is almost 1 which means that the states are indistinguishable and that the quantum states are well preserved.

Table 6.4: Experimental data for the 16 polarisation projections used to determine the fidelity of the system. This was achieved by setting the HWP and QWP in each arm of the inferometer to the appropriate orientations. From coincidence counts measured coincidence counts the density matrix was reconstructed.

N	State 1	State 2	HWP 1 (°)	QWP 1 (°)	HWP 2 (°)	QWP 2 (°)	C
1	$\|H\rangle$	$\|H\rangle$	45	0	45	0	23256
2	$\|H\rangle$	$\|V\rangle$	45	0	0	0	208
3	$\|V\rangle$	$\|V\rangle$	0	0	0	0	23417
4	$\|V\rangle$	$\|H\rangle$	0	0	45	0	426
5	$\|R\rangle$	$\|H\rangle$	22.5	0	45	0	10749
6	$\|R\rangle$	$\|V\rangle$	22.5	0	0	0	33059
7	$\|P\rangle$	$\|V\rangle$	22.5	45	0	0	10396
8	$\|P\rangle$	$\|H\rangle$	22.5	45	45	0	14400
9	$\|P\rangle$	$\|R\rangle$	22.5	45	22.5	0	13161
10	$\|P\rangle$	$\|P\rangle$	22.5	45	22.5	45	34859
11	$\|R\rangle$	$\|P\rangle$	22.5	0	22.5	45	19298
12	$\|H\rangle$	$\|P\rangle$	45	0	22.5	45	6005
13	$\|V\rangle$	$\|P\rangle$	0	0	22.5	45	10015
14	$\|V\rangle$	$\|L\rangle$	0	0	22.5	90	9001
15	$\|H\rangle$	$\|L\rangle$	45	0	22.5	90	7001
16	$\|R\rangle$	$\|L\rangle$	22.5	0	22.5	90	19211

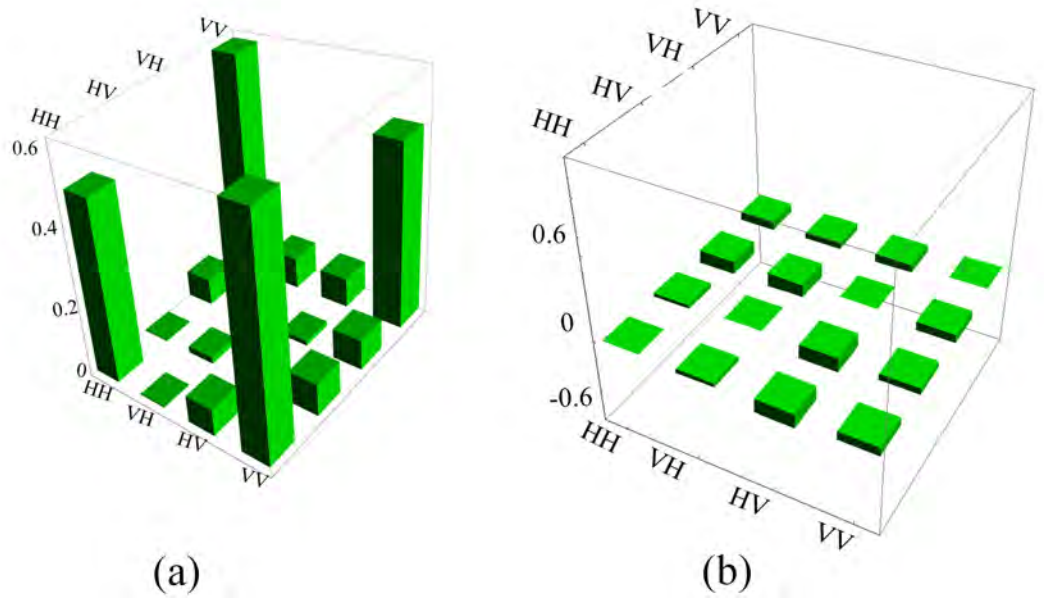

Figure 6.9: Graphical representation of the real (a) and imaginary (b) part of the reconstructed density matrix obtained from carrying out a full tomography of the system. It can be noted that the fidelity is almost 1 which means that the states generated are indistinguishable.

Table 6.5: Comparison of a low and high powered polarisation encoded entangled single photon source. The low powered source utilises a pump source of 20 mW while the bright source reached a power of 400 mW.

	Low powered source (20 mW)	High powered source (400mW)
Quality of entanglement (%)	91.3 ± 0.80	99.0 ± 0.14
Violation of the CHSH inequality	2.71 ± 0.03	2.79 ± 0.001
Fidelity	0.947 ± 0.0001	0.997 ± 0.0001

6.4 Comparison of Low and High powered Source

Within this study, two different entanglement sources were demonstrated, a low powered source with a power output of 20 mW as discussed in Chapter 3 and the source discussed within this chapter which was constructed using three economical lasers, reaching a power output of 400 mW. Both these sources were constructed using similar alignment, filtering and compensation techniques. The principal variation in these sources lies in the pump power. The quality of entanglement, violation of the CHSH inequality and the fidelity of the generated states were investigated for both systems. These results are presented in Table 6.5.

Taking into consideration the methods of verifying entanglement presented in this thesis, it is evident that the high powered laser source developed is the optimum of the two sources. The most promising enhancement between these two sources is the improved

violation of the CHSH inequality. The theoretical limit for the violation of the CHSH inequality is $2\sqrt{2}$. For the low powered source a violation of 2.71 ± 0.03 was measured which was 3.56 % less than the theoretical limit. In the case of the bright source the violation was measured to be 2.79 ± 0.001 which was 0.8 % less than the theoretical limit. Furthermore this was obtained at a lower integration time of 3s. From this it can be deduced that the bright source would be a potentially good choice of a source of single photons particularly for the encoding within a free space QKD link.

The quality of entanglement was also an improvement from 91.3 % for a low powered source to 99.0 % for the bright source. One of the factors that leads to an increase in the quality of entanglement, is the brightness of the source. This was further observed by the fidelity of the system. At the begining of this Chapter it was mentioned that one of the challenges in quantum communication is the development of a robust communication network which requires a bright source of high quality entanglement [130]. The aformentioned high powered source constructed fits the necessary criterion of a brighter source and would be beneficial for the further devopment of free space QKD.

7 Summary

Free space QKD, has of recent, been a topical process for achieving secure communication especially in urban areas prone to atmospheric turbulence. During the implementation of a free space quantum communication system, the survival of single photons especially in atmospheric conditions, is one of the major drawbacks of achieving a successful link. This study deals with understanding, constructing and developing an entanglement source.The objective was to understand the advancements and constraints of an entanglement source, essentially for the purpose of quantum communication.

Optical quantum communication is reliant upon a single photon source for the encoding. This criterion maybe satisfied by makign use of an entangled photon source. Preliminary experiments of this study involved generating polarisation based entangled photon pairs using a low powered source. This source was characterised by measuring the visibility of the correlation curves in the rectilinear and diagonal bases which was measured to be 91.3 % $\pm$ 0.8 % and 90.8 % $\pm$ 0.8 % respectively. We also proved that our system was entangled by violating the CHSH inequality by obtaining a vioation of 2.71 $\pm$ 0.03. Carrying out the state tomography, we obtained a fidelity of 0.947 $\pm$ 0.0001, which revealed that the quantum state remained preserved during propagation. Since one of the challenges of free space QKD based on entanglement, is the implementation of a bright source with high quality entanglement, we developed a high powered polarisation encoded single photon source with a power input of 400 mW using three economical lasers. We showed that using a brighter source it is possible to reach a CHSH violation of 2.79 $\pm$ 0.001 which is 0.8 % less than the theoretical limits. We have also observed a high quality of entanglement in both bases (rectilinear and diagonal bases) as collated in Table 6.5. Furthermore we reached a fidelity of 0.997 $\pm$ 0.0001 using this system which signifies that the generated states are indistingiushable. It it is evident that the bright source yeilds better results in terms of the violation of the CHSH inequality as well as the quality of

entanglement.

It is believed that the state of polarisation of photons are immune to atmospheric turbulence perturbations as the medium is isotropic. We mimicked in the laboratory the near and far field turbulence effects on the polarisation of entangled photons. We made use of a diffractive optical element to simulate turbulence distortions and measured the entanglement as a function of the turbulence strength. We showed that the standard detection method of single mode fibre coupling to single photon counters results in a spatial mode dependence on the coincidence, even if the entanglement is not measured with spatial modes. We found that the overall coupling inefficiency of the detected coincidence caused by spatial mode dependence can be corrected using a detection scheme coupled with multimode fibre. Our results suggest that care is required in the choice of a detection system for free space quantum communication systems.

An alternative approach to encoding single photons would be to make use of states carrying OAM. The advantage of a high dimensional entanglement source, is the ability to span an inifnite state space as well as achieve a higher encoding efficiency. A recent method of encoding is through the use of Bessel beams. We presented a versatile technique to experimentally realise the detection of Bessel beams using digital axicons programmed on a SLM. We have shown the ability to distinguish both the radial and azimuthal indices of such beams, a core requirement for optical communication protocols if the bit rate per photon is to be increased by exploiting all the degrees of freedom of spatial modes. In addition we have considered two applications of the tool and observed the modal changes to an incoming Bessel beam due to both amplitude and phase perturbations resulting from a turbulence plate. As the holograms are only phase dependent they are suitable for detection at the single photon level too. The ability to modally resolve such fields will find uses in both quantum and classical studies.

Encoding and a single photon source are important factors required for the development of free space QKD applications. This study touched on both these aspects which provides insight into some of the necessary tools required in advancing the field of free space QKD. Entanglement is significantly important for free space QKD as it provides a means to uphold the security of the system and garauntee the generation of single photons. The current global trend of quantum communication is to achieve, not only, long distance QKD however to take it a step further and implement satellite QKD. For this to reach its full potential the contruction of a high powered source, as constructed within this study, could prove useful as it offers the advantage of greater coincidence detection.

Apart from single photon propagation, understanding the processes and the influences of the environment is important for the successful implementation of QKD. This means

being able to understand not only the effects of lower order modes on the system however the effects of higher order modes are significant as the environment is not static and cannot be controlled. This suggests that compensation techniques are imperative to overcome the effects that the environment poses on the system. The turbulent studies discussed in this thesis provides a means to understanding the detection scheme of an entangled single photon source which provides insight into the development of QKD systems when dealing with strong and weak turbulence.

Most research in free space QKD are implemented using porisation for the encoding as oppose to phase for the reason of the influences of turbulences. Encoding using states carrying OAM is a significant enhancement to a QKD system as it spans an infinite state space however the breakdown of the phase under the influence of turbulence is a major drawback. Within this study it was shown that photons that are appropriately encoded to carry OAM provides a platform to introduce extra variables that could be controlled during a QKD process. This could be utilised to implement higher-dimensional QKD protocols based on mutually unbiased bases [136] which illustarates the value of understanding and generating states carrying OAM. Much work is still required in the field however, to ensure the stability of the system under non-ideal turbulent conditions. These investigation presented in this thesis were carried out with the intention of implementing a free space QKD link by making use of q-plates which incorporates both polarisation and phase encoding [137]. This will also be a beneficial for looking at MDI QKD which will be discussed briefly in the subsequent chapter.

8 Future Work

Quantum cryptography (QKD) is a physical process of securing information whereby the access of information is governed by the laws of nature. This process of exchanging information between two legitimate parties, is done so in the presence of an eavesdropper. QKD encodes the key information into a quantum data carrier that is then transported from one point to another. This shifts the security basis away from mathematical complexities towards fundamental physical boundaries set by the laws of quantum mechanics. This therefore means that the retrieval of the key information by illicit parties requires the defiance of the laws of quantum mechanics such as the Heisenberg's uncertainty principle[7]. Due to the laws of quantum mechanics, an eavesdropper cannot split the quantum signal to carry out measurements securely. QKD also obeys the quantum no-cloning theory [138]. This theory shows that it is not possible to duplicate a quantum data carrier. A basic QKD scheme is represented in Figure 8.1 which specifically utilises single photons as quantum data carriers encoded by bits of 1's and 0's.

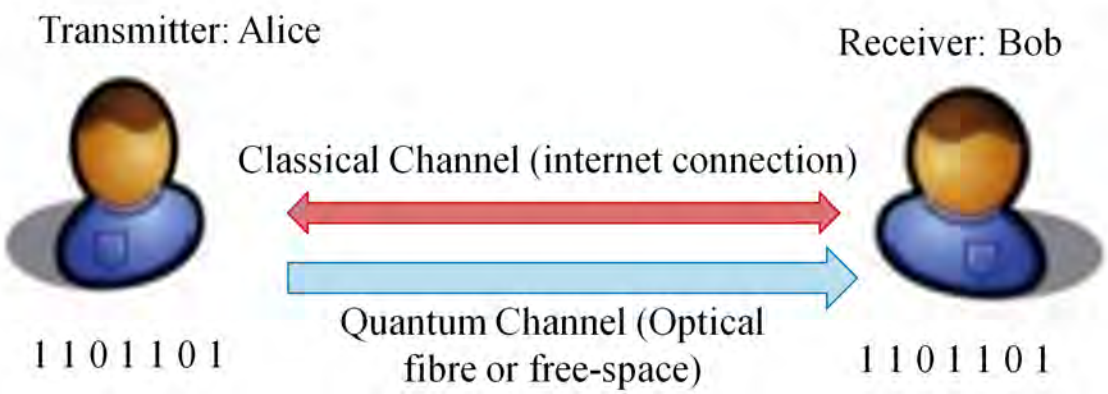

Figure 8.1: QKD scheme representing a transmitter (Alice) and Receiver (Bob) sharing a string of bits accross and a quantum channel and obtain a secure key through post-processing from a classical channel.

Two channels are required for the key distribution process, the quantum channel which is used for the propagation of the single photons and the classical channel required for the post-processing to determine a secure key. The quantum channel is of importance and is chosen dependent upon the method of encoding. Within this scheme, two types of quantum channels are applicable, either a fibre or a free space channel. The choice of encoding of single photons can be either through phase or polarisation and hence dictates the quantum channel used within the scheme. For a phase based encoding scheme it is preferable to use a fibre based channel and for a polarisation based scheme, a free space channel is most applicable.

8.1 Implementation of Quantum Key Distribution

QKD is realised by the implementation of the appropriate protocol. There are mainly two types of QKD schemes. One is the prepare-and-measure scheme, such as BB84 [139] and B92 [140] and the other are the entanglement based QKD, such as E91 [141] and BBM92 [142]. A concise discussion of the BB84, B92 and E91 protocols is presented below, for an understanding of the processes involved in obtaining a secure key.

BB84 Protocol

The BB84 protocol was the first QKD protocol proposed by Bennet and Brassard [139]. This is a four state protocol which makes use of the two non-orthogonal polarisation bases namely the rectilinear and the diagonal basis. Implementation of the BB84 protocol lies in the encoding of single photons with either the vertical, horizontal or the $\pm$ 45^{o} state of polarisation. The process entails transmitting a train of encoded single photons to the receiver. The receiver randomly choses to measure each of the photons in the rectilinear or diagonal bases. This procedure is carried out on the quantum channel. On the classical channel the post-processing takes place whereby the receiver announces to the transmitter as to which bases was used for the measurements and from this a sifted key is produced. At this point, those single photons with a mismatch in measurement bases will be discarded. The remainder of the single photons are kept for the continuation of the post-processing procedure.

B92 Protocol

This is a two-state protocol, similar to the BB84 protocol, except in this case instead of the measurement bases being announced on the classical channel during the post processing,

the detector that clicked is publicised. The authorised parties (Alice and Bob) would be able to distinguish the sifted key by the click of the detector since each detector is pre-assigned a bit value. This process is less efficient than the BB84 protocol however under certain assumptions there is greater secrecy during the post-processing of the single photons [140].

E91 Protocol

The E91 protocol is mathematically identical to the BB84 protocol except in makes use of entanglement. A pair of entangled photons is emitted from a single photon source such that one photon is directed towards the receiver (Alice) while the other is sent to the transmitter (Bob). Both authorised parties will carry out a measurement independent of each other by randomly choosing between the rectilinear or the diagonal bases. Since these photons are entangled if the receiver is the first to carry out a measurement, the transmitter will automatically measure the opposite state. By one of the authorised parties, inverting their string of bits received, a key can be produced [141].

The aforementioned protocols belong to the class of Discrete Variable (DV) protocols [143]. There exist also a class of Continuous Variable (CV) protocols which comprises of Coherent One Way (COW) protocol [144] and Differential Phase Shift (DPS) protocol [145]. Since the focus of this study is to consider entanglement as resource for QKD, these protocols will not be discussed futher. For a detailed review of these protocols refer to the work of Gisin *et al* [143].

8.2 Free space Measurement Device Independent Quantum Key Distribution

During the course of this study a potential point to point free space link was identified as seen in Figure 8.2 for the purpose of constructing a QKD system however the process is involved and falls beyond the scope of this study. This is an intercampus link with a line of sight of 6.62 km running from the University of KwaZulu-Natal, Physics department on the Westville Campus (Alice) to the MTB Building on the Howard College Campus (Bob). It is the intention to establish this link by implementing a Measurement Device Independent (MDI) QKD system.

The notion behind MDI QKD is to create a network of un-trusted nodes. Thus far within a QKD system, it is believed that the devices are trusted however practical system demonstrates the ability to perform side channel attacks. Unlike current entanglement based

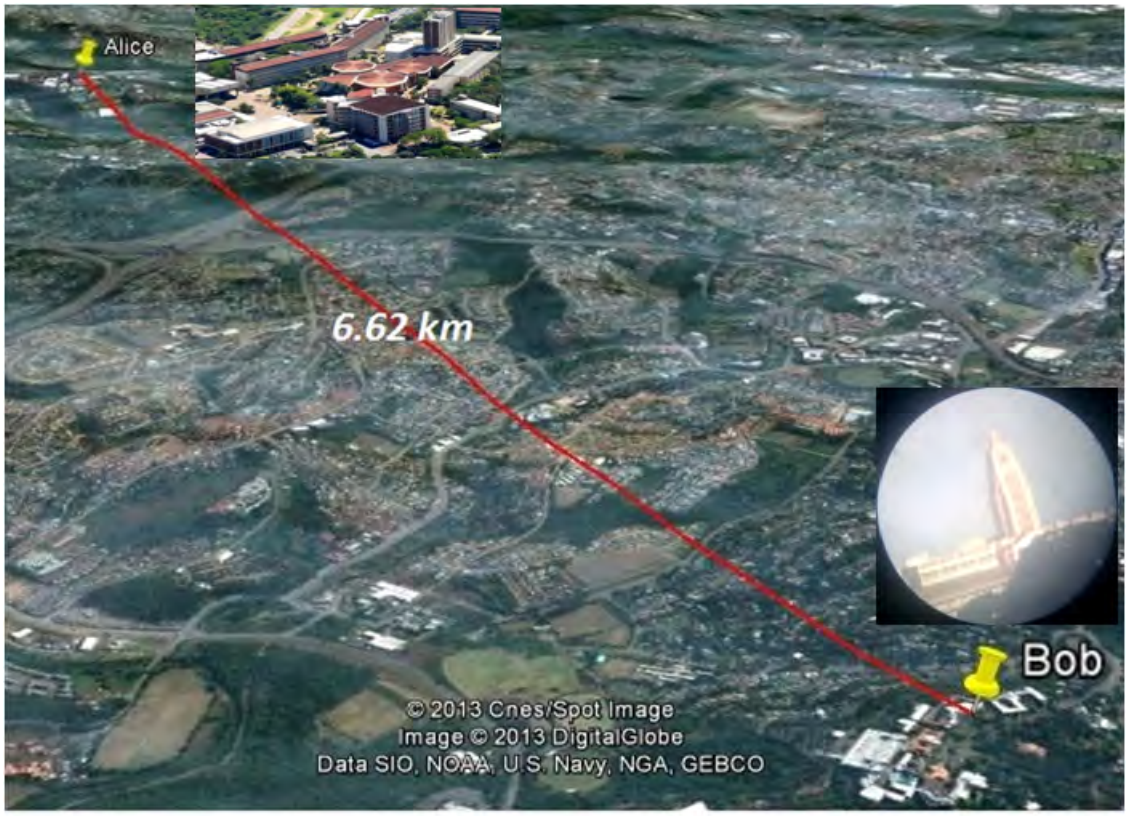

Figure 8.2: Potential point to point free space link was identified for the purpose of constructing a QKD system. This is an intercampus link with a line of sight of 6.62 km running from the University of KwaZulu-Natal, Physics department on the Westville Campus (Alice) to the MTB Building on the Howard College Campus (Bob).

QKD schemes where the entangled source lies with Alice, within the MDI-QKD scheme the entangled source lies with the adversary, Eve as illustrated in Figure 8.3.

Within this scheme Eve is allowed to perform a Bell state measurement and announce the measurement result. The measurement setting is only used to post-select entanglement between Alice and Bob hence it can be treated as a true black box. This makes MDI-QKD essentially resistant to all attacks in the detection system. This is a major accomplishment as MDI-QKD allows authorised individuals to perform secure quantum communications with un-trusted nodes.

MDI-QKD is highly practical and can be realised with standard optical components. The source does not need to be a perfect single-photon source and the measurement setting can be performed by a simple Bell state measurement using linear optics.

To date there has been a number theoretical studies reported on MDI-QKD [146, 147, 148, 149, 150, 151] as well as experimental attempts carried out by several groups [152, 153, 154, 155]. Nevertheless, for MDI-QKD to become a realistic application, there are a few practical issues that still needs to be addressed which include a loophole-free violation of a Bell inequality [156].

Recently, a secure transmission distance of MDI QKD over 200 km in fibre was demonstrated by Pan *et al* [157] whereby a secure key rate higher than previously reported [153, 155] by three orders of magnitude was demonstrated. These results pave the way towards a quantum network with MDI security and other quantum communication tasks, such as the development of quantum repeater.

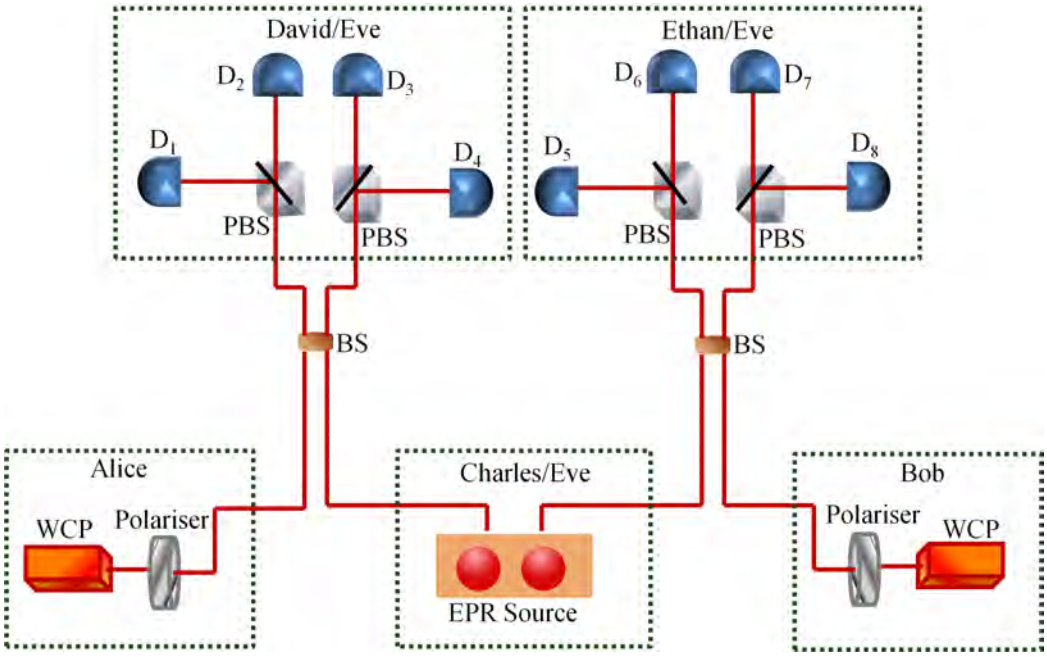

Figure 8.3: Measurement Device Independent QKD scheme whereby the the entangled source lies with the adversary, Eve. This scheme allows Eve to perform a Bell state measurement and announce the measurement results. The measurement setting is only used to post-select entanglement between Alice and Bob which means it can be treated as a true black box.

Bibliography

[1] Bohm D. Causality and Chance in Modern Physics. London: Taylor and Francis.; 2005.

[2] Dirac P A M. The Principles of Quantum Mechanis. Clarendon Oxford; 1987.

[3] Grynberg G, Fabre C, Aspect A. Introduction to Quantum Optics. Cambridge University Press; 2010.

[4] A D Aczel. Entanglement the Greatest Mystery in Physics. John Wiley & Sons Ltd; 2001.

[5] Lehmann J W. Atomic and Molecular Structure: the development of our concepts. John Wiley and Sons.; 1972.

[6] Grenier W. Quantum Mechanics: An Introduction. Springer; 2001.

[7] Griffiths D. Quantum Mechanics,. New Jersey: Pearson; 2005.

[8] Wheeler J A, Zurek W H. Quantum Theory and Measurement. Princeton University Press; 1983.

[9] Podolsky B, Einstein A, Rosen N. Can Quantum-Mechanical Description of Physical reality be Considered Complete? Physics Review A. 1935;47:777–780.

[10] Bell J S. On the Einstein-Podolski-Rosen Paradox. Long Island City, New York. 1964;1:403–408.

[11] Bohm D. Causality and Chance in Modern Physics. University of Pennsylvania Press; 1957.

[12] Clauser J, Horne M, Shimony A , Holt R. Proposed experiment to test local hidden-variable theories. Physical Review Letters. 1969;23(15):880–884.

[13] Aspect A, Grangier P, Roger G. Experimental Realization of Einstein-Podolsky-Rosen-Bohm Gedankenexperiment: A New Violation of Bellś Inequalities. Physics Review Letters. 1982;49(2):91–94.

[14] Freedman J S, Clauser J F. Experimental Test of Local Hidden-Variable Theories. Physical Review Letters. 1976;37:465.

[15] Fry E S, Thompson R C. Experimental Test of Local Hidden-Variable Theories. Physical Review Letters. 1976;37:465.

[16] Grangier P, Roger G, Aspect A. Experimental tests of Realistic local Theories via Bell's theorem. Physical Review Letters. 1981;47(7):460–463.

[17] Ghosh R, Mandel L. Observation of Nonclassical Effects in the Interferenceof Two Photons. Physical Review Letters. 1987;59:1903.

[18] Hong C K, Ou Z Y, Mandel L. Measurement of subpicosecond time intervals between two photons by interference. Physical Review Letters. 1987;59(18):2044–2046.

[19] Ou Z Y, Mandel L. Violation of Bellś Inequality and Classical Probability in a Two-Photon Correlation Experiment. Physical Review Letters. 1988;61:2921.

[20] Shih Y H, Alley C O. New Type of Einstein-Podolsky-Rosen-Bohm Experiment using pairs of light quanta produced by optical parametric down conversion. Physical Review Letters. 1988;61:2921.

[21] Kiess T E, Shih Y H, Sergienko A V, Alley C O. Einstein-Podolsky-Rosen-Bohm experiment using pairs of light quanta produced by type-II parametric down-conversion. Physical Review Letters. 1993;71(24):3893–3897.

[22] Kwait P G, Sergienko A V, Zeilinger A , et al. New High-Intensity Source of Polarization-Entangled Photon Pairs. Physical Review Letters. 1995;75(24):4337–4341.

[23] Kwait P G, Waks E, White A G, Appelbaum I. Ultrabright source of polarization-entangled photons. Physical Review A (Atomic, Molecular, and Optical Physics). 1999;60(2):R773–R776.

[24] Armstrong J A, Bloembergen N, Ducuing J, Pershan P S. Interactions between Light Waves in a Nonlinear Dielectric. Physical Review. 1962;127:1918.

[25] Fraken P A, Ward J F. Optical Harmonics and Nonlinear Phenomena. Review of Modern Physics. 1963;35:23.

[26] Fejer M M, Magel G A, Jundt D H, Byer R L. Quasi-phase-matched second harmonic generation: tuning and tolerances. IEEE Journal of Quantum Electronics. 1992;28:2631.

[27] Tabzilli S, Tittel H, Gisin N. Highly efficient photon-pair source using periodically poled lithium niobate waveguide. Electronics Letters,. Electronics Letters. 2001;37:38.

[28] Sanaka K, Kawahara K, Kuga T. High-Efficiency Source of Photon Pairs for Engineering Quantum Entanglement. Physical Review Letters. 2001;86(24):5620–5623.

[29] Kuklewicz C E, Fiorentino M, Messin G, Wong F N C, Shapiro H H. High-flux source of polarization-entangled photons from a periodically poled KTiOPO4 parametric down-converter. Physical Review A (Atomic, Molecular, and Optical Physics). 2004;69(1):013807.

[30] Fiorentino M, Messin G, Shapiro J H, et al. Generation of ultrabright tunable polarization entanglement without spatial, spectral, or temporal constraints. Physical Review A (Atomic, Molecular, and Optical Physics). 2004;69(4):041801.

[31] Pelton M, Marsden P, Laurell F, et al. Bright, single-spatial-mode source of frequency nondegenerate, polarization-entangled photon pairs using periodically poled KTP. Optics Express. 2004;12:3573.

[32] U'Ren A B, Silberhorn C, Banaszek K, Walmsley I A. Efficient Conditional Preparation of High-Fidelity Single Photon States for Fiber-Optic Quantum Networks. Physics Review Letters. 2004;93(9):093601.

[33] Fedrizzi A, Herbst T, Poppe A, Jennewein T, Zeilinger A. A wavelengthtunable fiber-coupled source of narrowband entangled photons. Optics Express. 2007;15:15377.

[34] Li X, Voss P L, Sharping J E, Kumar P. Optical-Fiber Source of Polarization-Entangled Photons in the 1550 nm Telecom Band. Physical Review Letters. 2005;94(5):053061.

[35] Fan J, Eisaman M D, Migdall A. Bright phase-stable broadband fiberbased source of polarization-entangled photon pairs . Physics Review A (Atomic, Molecular and Optical Physics),. 2007;76:043836.

[36] Eisaman M D, Fan J, Migdall A, Polyakov S V. Invited Review Article: Single-photon sources and detectors. Review of Scientific Instruments. 2011;82:0711101.

[37] Chuang I L, et al. Implementation of a three-quantum-bit search algorithm. Applied Physics Letters. 2000;75(5):646–648.

[38] Chuang I L, et al. Chuang. Experimental realization of shorś quantum factoring algorithm using nuclear magnetic resonance. Nature. 2001;414(6866):883–887.

[39] Blatt R, et al. Implmentation of the deutschjozsa algorithm on an ion-trap quantum computer. Nature. 2003;421(6918):48–50.

[40] Singh S, Khare P K, Mor P. Analysing Performance of Data Encryption Techniques. VSRD International Journal of Computer Science and Information Technology. 2011;1(6):339–349.

[41] Naseri M. Secure quantum dialogue using entanglement swapping. International Journal of Physical Sciences. 2012;7(27):5049–5053.

[42] Lo H K, Curty M, Tamaki K. Secure quantum key distribution. Nature Photonics. 2014;8:595–604.

[43] Beals T R. Quantum communication and Information processing. University of California, Berkeley; 2008.

[44] Simon C, et al . Quantum Memories. The European Physical Journal D - Atomic, Molecular, Optical and Plasma Physics. 2010;58(1):1–22.

[45] Ursin R, Jennewein T, Zeillinger A. Entanglement-based quantum communication over 144 km. Nature Photonics. 2007;3:481–486.

[46] Kolmogorov A N. Dissipation of energy in the locally isotropic turbulence. Comptes rendus (Doklady) del'Académie des Sciences de l'URSS. 1941;32:16–18.

[47] Kolmogorov A N. The local structure of turbulence in incompressible viscous fluid for very large Reynold's numbers. Comptes rendus (Doklady) de l'Académie des Sciences de l'URSS. 1941;30:301–305.

[48] Trichili A, Mhlanga T, Ismail Y, Roux F S, McLaren M, Zghal M, Forbes A. Detection of Bessel beams with digital axicons. Optics Express. 2014;22(14):17553–17560.

[49] Nielsen M A, Chuang I L. Quantum Information Processing and Communication. United Kingdom: Cambridge University Press; 2002.

[50] Edamatsu K, et al. Entangled state preparation for optical quantum communication. Progress in Informatics. 2011;8:19–26.

[51] Kwon O, Park K K, Ra Y S, Kim Y S, Kim Y H. Time-bin entangled photon pairs from spontaneous parametric down-conversion pumped by a cw multi-mode diode laser. Optics Express. 2013;21(21):25492–25500.

[52] Mair A, Vaziri A, Weihs G, Zeilinger A. Entanglement of the orbital angular momentum states of photons. Nature. 2001;412:313–316.

[53] Paris M G A. Entanglement and visibility at the output of a Mach-Zehnder interferometer. Physics Review A. 1999;59(2):1615–1621.

[54] Lawall J, Solomon G S, Muller A , Fang W. Creating polarization-entangled photon pairs from a semiconductor quantum dot using the optical stark effect. Physics Review Letters. 2009;103:217–300.

[55] Kocher C A, Commins E D. Polarisation Correlation of Photon emitted in an atomic cascade. Physics Review A. 1967;18(15):575–577.

[56] Fan J, Migdall A , Chen J, Levine Z H. Frequency-bin entangled comb of photon pairs from a silicon on-insulator micro-resonator. Optics Express. 2011;19:1470–1783.

[57] Liscidini M, Sipe J E, Helt L G, Yang Z. Spontaneous four-wave mixing in microring resonators. Optics Letters. 2010;35:3006–3008.

[58] Bogaerts W, Baets R G, Emplit P, Massar S, Clemmen S, Huy K P. Continuous wave photon pair generation in silicon-on-insulator waveguides and ring resonators. Optics Express. 2009;17:16558Ű16570.

[59] Weinberg D L, Burnham D C. Observation of simultaneity in parametric production of optical photon pairs. Physical Review Letters. 1970;25:84–87.

[60] Klyshko D N. Scattering of Light in a Medium with Nonlinear Polarizability. Journal of Experimental and Theoretical Physics. 1969;28(3):522–526.

[61] Steinlechner F, Ursin R, Pruneri V, et al. A high-brightness source of polarization-entangled photons optimized for applications in free space. Optics Express. 2012;20(9):9640–9649.

[62] Rangarajan R, Goggin M, Kwait P. Optimizing type-I polarisation-entangled photons. Optics Express. 2009;17(21):18920–18933.

[63] Franson D, Potock K A. Single-photon interference over large distances. Physics Review A. 1988;37:2511–2515.

[64] Rarity J G, Tapster P R. Experimental violation of Bells inequality based on phase and momentum. Physics Review Letters. 1990;64(21):2495–2498.

[65] Mair A, Vaziri A,Weihs G, Zeilinger A. Entanglement of the orbital angular momentum states of photons. Nature. 2001;412:313–316.

[66] Allen L, Beijerbergens M W, Spreeuw R J C, Woerdman J P. Orbital angular momentum of light and the transfromation of Laguerre-Guassian laser modes. Physical Review A. 1992;45(11):8185–8189.

[67] McClaren M, et al. Entangled Bessel-Gaussian beams. Optics Express. 2012;20(21):23589 – 23597.

[68] Padgett M J, Giovannini D, Lavery M, Romero J, Barnett S M , et al . Photon orbital angular momentum: generation, measurement and application to QKD. Proceedings of SPIE. 2012;Electro-Optical Remote Sensing, Photonic Technologies, and Applications VI:85421P.

[69] Ibrahim A H, Roux F S, McLaren M, Konrad T, Forbes A. The decay of the orbital angular momentum entanglement in turbulence. In: Frontiers in Optics; 2013. .

[70] Dehlinger D, Mitchell M W. Entangled photons, nonlocality and Bell inequalities in the undergraduate laboratory. American Journal of Physics. 2002;70:903.

[71] Monken C H, Souto Ribeiro P H, Pat'dua S. Optimizing the photon pair collection efficiency: A step toward a loophole-free Bells inequalities experiment. Physics Review A. 1998;57(4):R2267–R2269.

[72] Cosme O, Pádua S, Bovino F A, Mazzei A, Sciarrino F, Martini F De. Hong-Ou-Mandel interferometer with one and two photon pairs. Physical Review A. 2008;77:053822.

[73] William J M, James D F V, Kwiat P G, White A G. Measurement of qubits. Physical Review A. 2001;64:052312:1Ű15.

[74] Anufriev A V, Zimin I A, Volpov A L, Matveev I N. Change in the polarization of light in a turbulent atmosphere. Soviet Journal of Quantum Electronics,. 1983;13:1627–1628.

[75] Love G D, Gourlay J. Intensity-only modulation for atmospheric scintillation correction by liquid-crystal spatial light modulators. Optics Letters. 1996;21:1496–1498.

[76] Love G D. Wavefront correction and production of Zernike modes with a liquid crystal spatial light modulator. Applied Optics. 1997;36:1517–1524.

[77] Bold G T, Barnes T H, Gourlay J, Sharples R R, Haskell T G. Practical issues for the use of spatial light modulators in adaptive optics. Optics Communications. 1998;148:323–330.

[78] Dayton D C, Browne S L, Sandven S P, Gondlewski J D, Kudryashov A V. Theory and laboratory demonstrations on the use of a nematic liquid crystal phase modulator for controlled turbulence generation and adaptive optics. Applied Optics. 1998;37:5579–5589.

[79] Burger L, Litvin I A, Forbes A. Simulating atmospheric turbulence using a phase-only spatial light modulator. South African Journal of Physics. 2008;104:129–134.

[80] Wooters W K. Entanglement of Formation of an Arbitrary State of Two Qubits. Physics Review L. 1998;80:2245.

[81] Ibrahim A H, Roux F S, McLaren M, Konrad T, Forbes A. Orbital-angular-momentum entanglement in turbulence. Physics Review A. 2013;88:012312.

[82] Brunner T, Roux FS. Robust entangled qutrit states in atmospheric turbulence. New Journal of Physics. 2013;15:1–15.

[83] Zhao S, Yang H, Li Y, Cao F, Sheng Y, Cheng W, Gong L. The influence of atmospheric turbulence on holographic ghost imaging using orbital angular momentum entanglement: Simulation and experimental studies. Optics Communications. 2013;294:223–228.

[84] Frisch U. Turbulence: The Legacy of A. N. Kolmogorov. Cambridge, UK: Cambridge University Press; 1995.

[85] Andrews L C, Phillips R L. In Laser Beam Propagation Through Random Media. SPIE Optical Engineering Press, Bellingham; 1998.

[86] Andrew L C. In Field Guide to Atmospheric Optics. SPIE Optical Engineering Press, Bellingham; 2004.

[87] Fried D L. Statistics of a Geometric Representation of Wavefront Distortion. Optical Society of America Journal. 1965;55(11):1427–1435.

[88] Ebstein S M. Pseudo-random phase plates. Proceedinds of SPIE. 2002;4493:150–155.

[89] Strehl K. Zeitschrift für Instrumkde. 1901;22:213.

[90] Zhao X, Jiang H, Zheng H. Fibre coupling efficiency through turbulence medium for long and short exposures. IEEE Optoelectronics and Microelectronics. 2012;p. 334–336.

[91] Niu J, Xu J. Coupling efficiency of laser beams to multimode fibre. Optics Communications. 2007;274:315–319.

[92] Artl J, Dholakai K. Generation of high-order bessel beams by use of an axicon. Optics communications. 2000;177:277–301.

[93] Ismail Y, Beyli V, Khilo N, Forbes A. Shape invariant higher-order bessel-like beams carrying orbital angular momentum. Journal of Optics. 2012;14(8):085703:1–12.

[94] Mazilu M, Mourka A, Vettenburg T, Wright E M, Dholakia K. Simultaneous determination of the constituent azimuthal and radial mode indices for light fields possessing orbital angular momentum. Applied Physics Letters. 2012;100:231115.

[95] Mourka A, Mazilu M, Wright E M, Dholakia K. Modal characterization using principal componentanalysis: application to Bessel, higher-order Gaussian beams and their superpositions. Scientific Report. 2013;3:1422.

[96] Dudley A, Forbes A, Padgett M, et al. Efficient sorting of Bessel beams. Optics Express. 2013;21(1):165–171.

[97] Beijersbergen M W, Coerwinkel R P C, Kristensen M, Woerdman J P. Helical wavefront next term laser beams produced with a spiral phaseplate. Optics Communications. 1994;112:321–327.

[98] Clifford M A, Arlt J, Courtial J, Dholakia K. High-order Laguerre-Gaussian laser modes for studies of cold atom. Optics Communications. 1998;154:300–306.

[99] Heckenberg N R, McDuff R, Smith C P, White A G. Generation of optical phase singularities by computer-generated holograms. Optics Letters. 1992;17:221 Ű 223.

[100] Turnbull G A, Robertson D A, Smith G M, Allen L, Padgett M J. The generation of free-space Laguerre-Gaussian modes at millimetre-wave frequencies by use of a spiral phaseplate. Optics Communications. 1996;127:183–188.

[101] Bazhenov V Y, Vasnetsov M V, Soskin M S. Laser modes with screw dislocations in their wave-fronts. Journal of Experimental and Theoretical Physics Letters. 1990;52:429–431.

[102] McGloin D, Dholakai K. Bessel beams:diffraction in new light. Contemporary Physics. 2005;46(1):15–28.

[103] Gutierrez-Vega J C , Iturbe-Castillo M D, Chavez-Cerda S. Alterative formulation for invariant optical fields: Mathieu beams. Optics Letters. 2000;25:1493–1495.

[104] Bandres M A, Gutierrez-Vega J C. Ince Gaussian beams. Optics Letters. 2004;29:144–146.

[105] Galvez J E. Gaussian beams in optics courses. American Journal of Physics. 2006;74(4):355–361.

[106] Kennedy S A, Szabo M J, Teslow H, Porterfield J Z, Abrahams R I. Creation of Laguerre-Gaussian laser modes using diffractive optics. Physics Review A. 2002;66:043801.

[107] Durnin J, Miceli J J, Elberly J H. Diffraction-Free Beams. Physical Review Letters. 1987;58(15):1499–1501.

[108] Durnin J. Exact solutions for nondiffracting beams. I. The scalar theory. Journal of the Optical Society of America A. 1987;4(4):651–654.

[109] Mazilu M, Stevenson D J, Gunn-Moore F, Dholakai K. Light beats the spread: non-diffracting beams,Ť. Laser Photon Review. 2010;4(4):529–547.

[110] Dudley A, Lavery M, Padgett M, Forbe A. Unraveling Bessel Beams. Optics Photonics News. 2013;24(6):22–29.

[111] McLaren M, Agnew M, Leach J, Roux F S, Padgett M J, Boyd R W, Forbes A. Entangled Bessel-Gaussian beams. Optics Express. 2012;20(21):23589Ű23597.

[112] McLaren M, Mhlanga T, Padgett M J, Roux F S, Forbes A. Self-healing of quantum entanglement after an obstruction. Nature Communication. 2014;5:3284.

[113] Ramrez H C, Vega J C G, UŠRen A B, et al. Observation of non-diffracting behavior at the single-photon level. Optics Express. 2012;20(28):29761–29768.

[114] Gori F, Guattari G. Bessel-Gauss beams. Optics Communications. 1987;64(6):491–495.

[115] Mahmoud M A, Shalaby M Y, Khalil D. Propagation of Bessel beams generated using finite-width Durnin ring. Applied Optics. 2013;52(2):256–263.

[116] Herman R M, Wiggins T A. Production and uses of diffractionless beams. Journal of Optical Society of America A. 1991;8(6):932–942.

[117] Vasara A, Turunen J, Friberg A T. Realization of general nondiffracting beams with computer-generated holograms. Journal of the Optical Society of America A. 1989;6(11):1748–1754.

[118] Paterson C, Smith R. Higher-order Bessel waves produced by axicon-type computer-generated holograms. Optics Communications. 1996;124:121–130.

[119] Bowman R, Muller N, Padgett M J, et al. Efficient generation of Bessel beam arrays by means of an SLM. Europe Physics Journal on Special Topics. 2011;199:159–166.

[120] Rong Z Y, Han Y J, Wang S Z, Guo C. Generation of arbitrary vector beams with cascaded liquid crystal spatial light modulators. Optics Express. 2014;22(2):1636Ű1644.

[121] Bock M , Das S K, Grumwald R. Programmable ultrashort-pulsed flying images. Optics Express. 2009;17:7465–7478.

[122] Litvin I, McLaren M, Forbes A. A conical wave approach to calculating Bessel-Gauss beam reconstruction after complex obstacles. Optics Communications. 2009;282:1078–1082.

[123] Bouchal Z, Wanger J, Chulp M. Self-reconstruction of a distorted nondiffracting beam. Optics Communications. 1998;151:207–211.

[124] Khilo N A, Petrova E S, Ryzhevich A A. Transformation of the order Bessel beams in unaxial crystals. Quantum Electronics. 2001;31(1):85–89.

[125] Davidson N, Friesem A A, Hasman E. Holographic axilens: high resolution and long focal depth. Optics Letters. 1991;16:523–525.

[126] Litvin I A, Dudley A, Roux F S, Forbes A. Azimuthal decomposition with digital holograms. Optics Express. 2012;20(10):10996 –11004.

[127] Janssen A, Haver S, Dirksen P, Braat J. Zernike representation and strehl ratio of optical systems with numerical aperture. Journal of Modern Optics. 2008;55(7):1127–1157.

[128] Ou J, Wang S, Liao J, et al. Spreading of spiral spectrum of Bessel-Gaussian beam in non-Kolmogorov turbulence. Optics Communications. 2014;318:95–99.

[129] Nelson W, Palastro J P, Davis C C, Sprangl P. Propagation of Bessel and Airy beams through atmospheric turbulence. Journal of the Optical Society of America A. 2014;31(3):603–609.

[130] Jin A L E. Entangled state preparation for optical quantum communication. National University of Singapore; 2008.

[131] Saleh B E A, Tiech M C. Fundamentals of photonics. Goodman J W , editor. Wiley-Interscience; 1991.

[132] Altepeter J B , Jeffrey E R, Kwait P G. Phase-compensated ultr-bright source of entangled photons. Optics Express. 2005;13(22):8951–8959.

[133] Sellmeier W. Annalen der Physik und Chemie. 1871;143:271.

[134] Lee P S K, Exter van M P, Woerdman J P. Increased polarization-entangled photon flux via thinner crystals. Physics Review A. 2004;70:043818.

[135] Fan J, Bienfang J, Polyakov S, Migdall A. Single-Photon Generation and Detection. Lucatorto T, Parr A C, Baldwin K, editor. Academic Press; 2013.

[136] Mafu M, Dudley A, Petruccione F, et al. Higher-dimensional orbital-angular-momentum-based quantum key distribution with mutually unbiased bases. Physics Review A. 2013;88:032305–032313.

[137] Vallone G, DÁmbrosio V, Marrucci L, Villoresi P, et al. Free-Space Quantum Key Distribution by Rotation-Invariant Twisted Photons. Physical Review Letters. 2014;113:060503.

[138] Buzek V, Hillery M. Quantum copying: Beyond the no-cloning theorem. Physical Review A. 1996;54(3):1844–1852.

[139] Bennett C H, Brassard G. Quantum cryptography: public key distribution and coin tossing. In: In International Conference on Computers, Sytems and Signal Processing,; 1984. .

[140] Bennett C H. Quantum cryptography using any two nonorthogonal states. Physical Review Letters,. 1992;68:3121–3124.

[141] Ekert A K. Quantum cryptography based on Bellś theorem. Physical Review Letter. 1991;67:661–663.

[142] Bennet C H, Brassard G, Mermain N D. Quantum cryptography without BellŠs theorem. Physical Review Letters. 1992;68(5):557–559.

[143] Gisin N, Ribordy G, Titel W, Zbinden H. Quantum Cryptography. Review of Modern Physics. 2002;74(1):145–195.

[144] Stucki D, Fasel L, Gisin N, Thoma Y, Zbinden H. Coherent one way quanutm key distribution. In Society of Photo-Optical Instrumentation Engineers (SPIE) Conference Series. 2007;6583:18.

[145] Kyo I, Waks E, Yamamoto Y. Differential phase shift quantum key distribution. Physical Review Letters. 2002;89(3):037902.

[146] Tamaki K, Lo H K, Fung C H F, Qi B. Phase encoding schemes for measurement-device-independent quantum key distribution with basis-dependent flaw. Physics Review A. 2012;85:042307.

[147] Ma X, Fung C H F, Razavi M. Statistical fluctuation analysis for measurement-device-independent quantum key distribution. Physical Review A. 2012;86:052305.

[148] Ma Z, Razavi M. Alternative schemes for measurement-device-independent quantum key distribution. Physics Review A. 2012;86:062319.

[149] Song T T, Wen Q Y, Guo F Z, Tan X Q. Finite-key analysis for measurement-device-independent quantum key distribution. Physical Review A. 2012;86:022332.

[150] Wang X B. Three-intensity decoy-state method for device-independent quantum key distribution with basis-dependent errors. Physical Review A. 2013;87:012320.

[151] Chan P, Slater J A, Rubenok A, Lucio-Martinez I, Tittel W. Modeling a measurement-device-independent quantum key distribution system. Optics Express. 2014;22(11):12716–12736.

[152] Rubenok A, Slater J A, Lucio-Martinez I, Tittel W. Real-World Two-Photon Interference and Proof-of-Principle Quantum Key Distribution Immune to Detector Attacks. Physics Review Letters. 2013;111:130501.

[153] Liu Y, et al . Experimental Measurement-Device-Independent Quantum Key Distribution. Physics Review Letters. 2013;111:130502.

[154] Silva T F, et al. Proof-of-principle demonstration of measurement-device-independent quantum key distribution using polarization qubits. Physics Review A. 2013;88:052303.

[155] Tang Z, Liao Z, Xu F, QI B, Qian L, Lo H K. Experimental Demonstration of Polarization Encoding Measurement-Device-Independent Quantum Key Distribution. Physics Review A. 2014;112:190503.

[156] Larsson J, Giustina M, Kofler J, Wittmann B, Ursin R, Ramelow S. Bell-inequality violation with entangled photons, free of the coincidence-time loophole. Physics Review A. 2014;90:032107.

[157] Liu Y, Chen T-Y, Wang L-J, Liang H, et al. Measurement-device-independent quantum key distribution over 200 km. Physical Review Letters. 2014;113(19):190501.